

## **University of Southampton Research Repository**

Copyright © and Moral Rights for this thesis and, where applicable, any accompanying data are retained by the author and/or other copyright owners. A copy can be downloaded for personal non-commercial research or study, without prior permission or charge. This thesis and the accompanying data cannot be reproduced or quoted extensively from without first obtaining permission in writing from the copyright holder/s. The content of the thesis and accompanying research data (where applicable) must not be changed in any way or sold commercially in any format or medium without the formal permission of the copyright holder/s.

When referring to this thesis and any accompanying data, full bibliographic details must be given, e.g.

Thesis: Author (Year of Submission) "Full thesis title", University of Southampton, name of the University Faculty or School or Department, PhD Thesis, pagination.

Data: Author (Year) Title. URI [dataset]

## **University of Southampton**

Faculty of Engineering and Physical Science School of Electronics and Computer Science

# Optical modulation in vanadium dioxide-based nanophotonic devices

by

Zihang Zheng

A thesis submitted in fulfilment for the degree of Doctor of Philosophy

Mar / 2025

## **University of Southampton**

Faculty of Engineering and Physical Science School of Electronics and Computer Science

#### **Abstract**

Doctor of Philosophy

Optical modulation in vanadium dioxide-based nanophotonic devices

by Zihang Zheng

The material of vanadium dioxide (VO<sub>2</sub>) possesses a metal-insulator transition at approximately 68 °C, and drastic changes in its optical and electrical properties accompany this phase transition. In recent years, benefiting from rapid advances in nanofabrication and characterisation technologies, VO<sub>2</sub>-based nanophotonic devices have attracted a lot of research attention. In terms of phase and power modulation of near-infrared lights, VO<sub>2</sub>-enabled devices present a wide range of applications such as optical imaging sensors for portable platforms and energy-control solar units. Currently there are two main challenges in applications of phase-change materials: the precise prediction of changes in their physical characteristics to improve the reliability of device designs, and how to apply the characteristic data extracted from both experiments and analytical methods to versatile designs. This thesis reports my research on these two specific challenges about the optical modulation based on VO<sub>2</sub> phase transition through introducing two pieces of separate but highly correlated work.

In my first work, I propose vertical growth models for analysing the VO<sub>2</sub> phase transition, which assumes that during the thermally driven phase transition of VO<sub>2</sub>, the transformation of components in the mixture from the insulating phase to the metallic phase exhibits directional preference. The vertical growth models are established analytically, which assumes different regulations in changes of physical parameters from effective medium models by introducing more interfaces in the nanostructure. By comparing the temperature-dependent reflection change derived from theoretical models, the vertical growth model shows better matching to the experimental benchmark than commonly used effective medium models. It provides a potential tool to predict the behaviour of switchable devices enabled by phase transition materials.

In my second work, I design a tunable metalens that works at 1550 nm. By utilising the temperature dependence of VO<sub>2</sub>, the binary focus tuning is implemented on the metalens in numerical simulation. It has also been found to possess continuously tuneable characteristics. In addition to providing a metalens design, I propose an algorithm for rapidly selecting elements and determining the metalens structure based on lens parameters, and on the basis, generalize a workflow of tunable metalens design.

## **Table of contents**

List of Publications	7
Journals	7
Conference papers	7
List of Figures	8
List of Abbreviations	10
Declaration of Authorship	11
Acknowledgements	12
1. Introduction	13
2. Backgrounds and literature review	17
2.1. Vanadium dioxide (VO <sub>2</sub> ) and its applications	17
2.1.1. Insulator-metal phase transition of VO <sub>2</sub>	17
2.1.2. VO <sub>2</sub> photonics	20
2.2. Effective medium models (EMM)	25
2.3. Overview of fundamental optical systems	31
2.3.1. The focusing and zooming implemented by geometric optics	31
2.3.2. From refractive optics to diffractive optics	34
2.4. Metasurfaces and metalenses.	37
2.4.1. The applications of metasurfaces based on VO <sub>2</sub> phase transition	37
2.4.2. Introduction to metalenses and their categorisation	40
2.4.3. The general design method of metalenses	46
3. Methodology	50
3.1. Fabrication techniques of VO <sub>2</sub> films	50
3.2. Transfer matrix methods for analytical calculations	54
3.3. Characterisation enabled by spectroscopic ellipsometry	56
3.4. Parametric sweep on multiple dimensional variables	58
4. Results and discussion	61
4.1. Vertical growth models	61
4.1.1. Vertical growth models	61
4.1.2. Multi-layered VO <sub>2</sub> -based films	63
4.1.3. Temperature-dependent reflection measured at certain wavelengths	66
4.1.4. Reflection analytically derived from theoretical models	68
4.1.5. Benchmarking using Degree of Non-monotonic Dependence (DoND)	71
4.1.6. Quantified comparison against the experiment	74
4.2. VO <sub>2</sub> -enabled tunable metalens	78
4.2.1. Parameters of elements in the metalens array	78

4.2.2. Metalens design and setup of simulation environment	
4.2.3. Binary focus tuning implemented by numerical simulation	86
4.2.4. Quantified analysis of the tunable metalens	89
4.2.5. Continuous focus tuning and extended applications	91
4.3. Fabrication work	95
4.3.1. Exploration on ICP etching rate of Si	95
4.3.2. Fabrication of embedded VO <sub>2</sub> fillings	96
4.3.3. The phase transition of ultra-thin VO <sub>2</sub> films	102
5. Summary and future work	106
5.1. Summary of my PhD project	106
5.2. Future work	108
Appendix	110
A. Simulation settings of COMSOL	110
B. Quantified comparison between different models	112
C. Parameters of representative elements in the metalens array	113
D. Element optimisation by using different forms of VO <sub>2</sub> coating	115
E. Mie-resonance tunable metasurfaces based on VO <sub>2</sub>	118
List of References	121

## **List of Publications**

#### **Journals**

[1] Title: Vertical growth model for VO<sub>2</sub> phase transition: the opposite of effective medium

models

Authors: Zihang Zheng, Kai Sun, Yuxin Du, Otto L. Muskens, Cornelis H. (Kees) de Groot &

Xu Fang

Status: Unpublished

[2] Title: Low temperature annealing for vanadium dioxide in photonic integrated circuits

Authors: Yuxin Du, Kai Sun, Zihang Zheng, Otto L. Muskens, Cornelis H. (Kees) de Groot &

Xu Fang

Status: Unpublished

#### Conference papers

[1] Title: Vertical Growth Models Outperform Effective Medium Models in Analysing VO2

**Phase Transition** 

Authors: Zihang Zheng, Kai Sun, Yuxin Du, Otto L. Muskens, Cornelis H. (Kees) de Groot &

Xu Fang

Status: Published at 2022 Conference on Lasers and Electro-Optics (CLEO)

[2] Title: Vertical growth models for analysing vanadium dioxide phase transition in thin films

Authors: Zihang Zheng, Kai Sun, Yuxin Du, Otto L. Muskens, Cornelis H. (Kees) de Groot &

Xu Fang

Status: Published on IOP Photon 2022

[3] Title: Vanadium dioxide-enabled tunable metasurfaces

Authors: Zihang Zheng, Kai Sun, Yuxin Du, Cornelis H. (Kees) de Groot & Xu Fang

Status: Published on the 84th JSAP Autumn Meeting 2023

# **List of Figures**

Fig. 1 Schematic diagram of insulator-metal transition of VO <sub>2</sub>				
Fig. 2 Measurement of optical properties of VO <sub>2</sub> thin films through phase transition				
Fig. 3 Thermal hysteresis of VO <sub>2</sub> nanocrystals exhibited by transmission changes. 23				
Fig. 4 Characterisation of a tuneable absorber based on VO <sub>2</sub> phase transition 24				
Fig. 5 The effective medium approximation for continuous multiple composites 25				
Fig. 6 Extraction of temperature-dependent parameters based on literatures 30				
Fig. 7 Several examples of single-piece lenses.				
Fig. 8 A selection of famous camera lenses design.				
Fig. 9 Schematic comparison between refractive optics and diffractive optics 35				
Fig. 10 Two application examples of diffractive optics.				
Fig. 11 Tunable Mie resonance-based tunable dielectric metasurfaces				
Fig. 12 Terahertz-band coding enabled by VO <sub>2</sub> -based switchable metasurfaces 40				
Fig. 13 Propagation phase metalens based on nanofin pair units				
Fig. 14 Schematic and properties of Mie-resonance metalens. 43				
Fig. 15 Switchable Pancharatnam-Berry metalens working at the terahertz regime				
45				
Fig. 16 Coherently controlled beam-steering implemented on a phase-gradien				
metasurface				
Fig. 17 Unit nanostructure and the phase library produced through parametric				
sweep on it. 48				
Fig. 18 Schematic diagram of an ion sputtering system 50				
Fig. 19 Schematic representation of ALD using self-limiting surface chemistry and				
an AB binary reaction sequence. 51				
Fig. 20 Ellipsometry fitting results of $n$ and $k$ of $VO_2$				
Fig. 21 Schematic of the basic unit of the metalens.				
Fig. 22 Different analytical interpretations of VO <sub>2</sub> phase transition				
Fig. 23 SEM image and optical reflection measured on one of the two VO <sub>2</sub> thin films				
Fig. 24 Broadband reflection spectra of three types of vertical growth models and				
Looyenga's model				
Fig. 25 Example of a relationship curve to convert temperature $T$ and volume				
fraction factor f to each other (1550 nm)				
Fig. 26 Effective permittivity and reflection calculated based on the Looyenga (the				
solid black lines) and the Bruggeman EMMs (the dashed green lines). The				
wavelength is 1550 nm				
Fig. 27 Reflection derived from the VGM at the wavelength of 1550 nm				
Fig. 28 Definition of <i>DoND</i> (Degree of Non-monotonic Dependence)				
Fig. 29 Maps of reflection $R$ , together with curves of figures of merit extracted from				
the maps				
Fig. 30 The three figures of merit, (a) $R_{\min}$ , (b) $\Delta R$ and (c) $DoND$ for the second sample				
7*				

Fig. 31 Reflection phase with respect to different side length a and b obtain	ained by
parametric sweep via Lumerical simulation	80
Fig. 32 Target (solid lines) and simulated (dot) phase profile along the $x$ dire	ection. 84
Fig. 33 Layout of the designed metalens pattern viewed from above	85
Fig. 34 Distribution of electric field intensity to show binary tuning of the n	netalens.
	86
Fig. 35 Extraction and calculation of focus parameters at insulating state	88
Fig. 36 Graphs of normalised phase against filling factor $f$ of units along $x$ -a	xis 90
Fig. 37 Electric field distribution in xz-plane that shows the position and	shape of
focusing point	93
Fig. 38 Continuous tuning of the VO <sub>2</sub> metalens	94
Fig. 39 Etch rate measured from different SOI-based samples with different	t etching
recipes.	96
Fig. 40 Fabrication process of the embedded $ m VO_2$ filling	98
Fig. 41 Layout of mask design for E-beam lithography	99
Fig. 42 Photo and SEM images of the VO <sub>2</sub> filling structure buried in the Si su	ubstrate.
	100
Fig. 43 AFM images of the VO <sub>2</sub> filling structure buried in the Si substrate	101
Fig. 44 Reflection of VO <sub>2</sub> films of different thicknesses.	102
Fig. 45 Reflection spectra across broadband measured on VO <sub>2</sub> samples of	different
thicknesses	104
Fig. 46 High-index dielectric Quasi-BIC metasurfaces	109

#### List of Abbreviations

ALD - Atomic layer deposition

BAML - Broadband achromatic metalens

B-antinode – Magnetic field antinode

BIC - Bound states in the continuum

BMM – Bruggeman model

CVD – Chemical vapour deposition

DLSR - Digital single-lens reflex cameras

ED - Extra-low dispersion (glass)

EMA – Effective medium approximations

EMM – Effective medium models

EMTs/EMT – Effective medium theories

E-antinode – Electrical field antinode

FDTD - Finite-difference time-domain

FP - Fabry-Perot (cavity)

FTIR - Fourier transform infrared microscope

GSST - Germanium-antimony-antimony-tellurium (GeSbSeTe)

GST - Germanium-antimony-tellurium (GeSbTe)

HOM - High order multipole

IBE - Ion beam etching

ICP - Inductively coupled plasma (etching)

LCP - Left-handed circularly polarised

MSE – Mean square error

NA – Numerical aperture

PB - Pancharatnam-Berry (phase)

PECVD - Plasma-enhanced chemical vapour deposition

PMMA – Polymethyl methacrylate

PVD – Physical vapour deposition

qBIC – Quasi bound states in the continuum

RCP - Right-handed circularly polarised

RIE – Reactive ion etching

SOI – Silicon on insulator

VGM – Vertical growth model

# **Declaration of Authorship**

Print name: Zihang Zheng
Title of thesis: Optical modulation in vanadium dioxide-based nanophotonic devices
I, Zihang Zheng, declare that this thesis and the work presented in it are my own and have been generated by me as the result of my own original research.
I confirm that:
This work was done wholly or mainly while in candidature for a research degree at this University;
Where any part of this thesis has previously been submitted for a degree or any other qualification at this University or any other institution, this has been clearly stated;
Where I have consulted the published work of others, this is always clearly attributed;
Where I have quoted from the work of others, the source is always given. With the exception of such quotations, this thesis is entirely my own work;
I have acknowledged all main sources of help;
Where the thesis is based on work done by myself jointly with others, I have made clear exactly what was done by others and what I have contributed myself;
Parts of this work have been published as journal papers or conference papers as listed in the list of publications.
Signature:
Date:

## Acknowledgements

I would like to express my gratitude to my supervisors, Dr Xu Fang, Prof Kees De Groot and Dr Kai Sun at the very beginning. They have provided me with significant theoretical support during the past years, especially in the early stages of my PhD project when I was struggling in determining the research direction.

I also would like to give my thanks to my collaborators, who provided excellent examples of how to solve specific problems and shared their valuable opinions through discussion. Dr Fei He, Dr Shengqi Yin, Dr James Frame, Dr Hailong Pi, Jianzhi Huang, Yuxin Du, Siyu Chen. Though some of them are working on a very different topic from my work, they still lent me a helping hand wherever possible with simulation and fabrication work.

I also would like to show my appreciation to colleagues who work together in the Sustainable Electronic Technologies research group and even in the entire ECS school. Here I would like to specifically list Tongjun Zhang, Dongkai Guo, Jiale Zeng, Jiapei Zhang, Wenjie Wang, Chuang Sun, Wangke Yu, Yue Fan for their assistance in fabrication training and cross-disciplinary mentoring.

I also would like to thank to my friends who provided me with both material and mental care in daily life, so that we could overcome the difficulties brought by the COVID restrictions together. Thanks to Anyu Shang, Mingjie Huang, Ruixiao Zhang, Dingzhao Wang, Yihong Wu, Weilin Jin, Cong Xie, Zhihao Tao, Qiaoyu Luo, Zhangyan Gao, and everyone who stood by my side during the past few years.

Last but not the least, I would like to give special thanks to my parents who provided solid support from my home country. Without them, I might lose the motivation in every sense of the word to continue striving and completing my PhD project. The last sentence of this acknowledgements belongs to Weihua Zheng and Aiping Wang, my dear parents.

#### 1. Introduction

The formation of the idea of my entire PhD work is strongly related to the concept of metamaterials that I encountered during my master's project and the initial understanding of its research field. Since the beginning of 21st century, the field of metamaterials has been gaining more attention as they can present functions or physical properties that conventional devices are unable to implement through artificially designed composite structures [1]. One of the core features of metamaterials is the specific subwavelength structure, such as the gratings composed of nanowires or nanopillars, ring resonators, two-dimensional photonic crystals [2], and silicon waveguides. A variety of subwavelength structures are designed to produce frequency-dependent response to electromagnetic waves, thereby achieving myriad unique features including perfect absorption, focusing and de-focusing, negative refractive index, and localized surface plasmon resonance. As a result, metamaterials also provide the functional basis for various applications that have developed rapidly in the last decade, such as the metalenses, nanoarrays of lidar, solar reflectors, subwavelength optical antennas, optomechanical cavities, and strain sensors. Among the various fields where metamaterials are motivating the development of applications, optical modulation has received great attention due to its huge market value and breadth of application scenarios. At present, the main challenges in the application of metamaterials in optical device design are in two aspects. The first and most critical challenge is to improve the tunability of devices by using materials with adjustable properties, which determines the flexibility of optical modulation. The second challenge is brought by the increase in design complexity of devices. For example, some of the metalenses proposed recently integrate multiple features such as focus tuning, variable aperture, and reconfigurable array. Compared with the early forms of metalenses, how to bring out the design efficiently and accurately has contributed to more discussion. My entire PhD work is revolved around these two main challenges, and I have been committed to proposing a possible solution from my own perspective. Next, I will explain how the backgrounds introduced above motivate me to engage in my research on the materials and device design.

Many functional materials consist of multiple different constituent materials or phases, and effective medium models (EMMs) have evolved into a classical tool for analysing their electromagnetic properties [3, 4]. An exquisite textbook example of such materials is vanadium dioxide (VO<sub>2</sub>) [5, 6]. It has attracted a lot of research interest, not only for its intriguing strongly correlated electronic behaviours [7, 8] but also for its broad range of potential applications, which include temperature regulation [9], photodetection [10], photo-thermal actuation [11] and neuromorphic computing [12]. VO<sub>2</sub> possesses a solid-state, first-order phase transition at approximately 68 °C, with the exact temperature affected by factors such as the method and the

conditions of fabrication. At temperatures sufficiently below (e.g., 25 °C) or above (e.g., 100 °C) the phase transition temperature, VO<sub>2</sub> has a pure monoclinic insulating phase or a pure rutile metallic phase, respectively. At intermediate temperatures, the two phases co-exist and their volume fractions are temperature-dependent [13]. Because of the large electromagnetic property contrast between these two phases, these intermediate VO<sub>2</sub> states show intriguing temperature dependencies in their electromagnetic properties, which are usually both non-linear and hysteretic [14]. Among multiple EMMs available for analysing these intermediate states [15-19], the Bruggeman model [20-23] is frequently used, while the Looyenga model (also referred to as the Landau-Lifshitz-Looyenga model [24]) benefits from a straightforward formula [25].

The Bruggeman model and the Looyenga model were first proposed more than half a centenary ago (in 1935 and 1965, respectively, to be more specific) when the current nanotechnology advancements could not be foreseen. Specific to VO<sub>2</sub>, many of its emerging functionalities (e.g., electromagnetic wavefront shaping [5] and neuromorphic computing [12]) require the VO<sub>2</sub> to have at least one dimension at the nanoscale. This raises the doubt of whether the classical EMMs remain valid for these nano-devices.

This problem can trace its origin to a fundamental assumption taken by all the EMMs: they all assume that the constituent materials/phases are well mixed in space, making the whole mixture react to electromagnetic waves like a homogenous medium (hence the name of effective medium) [3, 4]. This assumption can easily become invalid in a VO<sub>2</sub> film that has a thickness at the nanoscale. As a general rule in thermodynamics, heterogeneous nucleation, which occurs at interfaces or sites of defects, is favoured over homogeneous nucleation, which occurs away from interfaces, due to its lower energy barrier. For thin films that have a large surface area to volume ratio, this preference for heterogeneous nucleation becomes dominant. This behaviour is indeed observed recently on epitaxial VO<sub>2</sub> films by using TEM (transmission electron microscopy), which clearly excludes the existence of a uniformly mixed, effectively homogenous medium at any moment during the phase transition [26]. This experimental observation directly contradicts the fundamental assumption of EMMs. I consequently raise this question: is there any alternative to EMMs for VO<sub>2</sub> nanophotonics research? My PhD work is aiming to answer this question.

Next is the second challenge, which is how to apply tunable materials with complex regulations in the changes in their physical properties to design innovative optical devices. Here I still put my focus on VO<sub>2</sub>, which processes the feature of low-temperature phase transition. This feature makes it advantageous in possible development of industrial applications, as it will significantly

reduce the cost of peripherals used to achieve its tunability. The phase transition of VO<sub>2</sub> has several fundamental characteristics: (i) The insulator-metal phase transition occurs at a relatively low temperature (depending on the fabrication conditions, usually around 68 °C), and has obvious thermal hysteresis characteristics [13, 27]. (ii) The phase transition is reversible, and the speed is very fast, reaching the femtosecond level [28]. (iii) When the phase of VO<sub>2</sub> changes, its refractive index and permittivity change continuously. Some studies have proven that other optical or electrical properties of VO<sub>2</sub> also exhibit changes during the phase transition, which will not be discussed in this chapter.

Based on the phase transition characteristics of VO<sub>2</sub>, VO<sub>2</sub> is widely used in the design of various light modulation devices in the nanophotonic field [29]. Among them, dynamic colour filters [30, 31], light modulation of waves from visible to near-infrared bands [32, 33], intensity modulation of multi-wavelength light using the contrast of refractive index in its two phases (pure insulating and metallic phases) [34, 35], and switching functions based on full reflection or absorption characteristics [36-38] have received widespread attention. My PhD work which will be detailed in this thesis emphasizes the phase modulation function, the most typical application case of which is metalens.

Metalens is a category of optical devices made of artificial nanostructures rather than traditional curved glass or plastic lenses [39, 40] that will be introduced in detail in further chapters. These subwavelength nanostructures are designed to control the phase, amplitude, and polarisation of light of specific wavelengths, allowing for the manipulation of light in ways that are traditionally achieved with conventional lenses, which is the theoretical basis of metalens [41, 42]. The concept of metalenses has gained significant attention in the field of optics and photonics due to their potential for overcoming some limitations of conventional lenses, such as size, weight, and the need for multiple elements.

Among the optimisation directions of metalens, the focus tuning attracts my attention. The main methods known for designing tuneable metalens include these. (i) To use electro-optic materials, such as liquid crystals or electroactive polymers, to change the refractive index of specific regions of the metalens or directly apply an external electric field to modulate the material's properties, allowing for dynamic control over the focal length [43, 44]. (ii) To use materials with a high thermo-optic coefficient that changes refractive index in response to temperature variations, then incorporate a heating element, such as a microheater, to locally heat specific regions of the metalens, altering its optical characteristics [45]. (iii) To employ piezoelectric or shape-memory materials to induce controlled mechanical deformation in the metalens structure. With external forces or electrical signals applied, the shape of the lens is changed, thereby

adjusting its focal length [46, 47]. (iv) To integrate acoustic waves to modulate the refractive index of the metalens [48, 49].

Then one another question to answer by my thesis appears here: by leveraging the fundamental properties of metalenses and the insights gained from my previous work on VO<sub>2</sub> phase transition, how to design a VO<sub>2</sub>-based tuneable metalens then its focal length can be switched by using the high contrast between the refractive indices of VO<sub>2</sub> at its insulating and metallic phases? My PhD work aims to explore how VO<sub>2</sub>-based metalens will perform and whether there is an effective method to design this kind of metalenses (or other optical devices) with tunability.

## 2. Backgrounds and literature review

#### 2.1. Vanadium dioxide (VO<sub>2</sub>) and its applications

#### 2.1.1. Insulator-metal phase transition of VO<sub>2</sub>

Vanadium (element symbol V) is a metal element of the VB group. Vanadium can form a variety of oxides and present various valences in them. Vanadium metal is a malleable, hard and nonmagnetic material which has a high melting point and very stable chemical properties [50]. But for vanadium oxides (such as vanadium dioxide, and vanadium pentoxide), the physical and chemical properties are significantly different. Vanadium oxides are commonly regarded as good phase transition materials. For example, the phase transition temperature of vanadium dioxide is about 68 °C, and that of vanadium pentoxide is 257 °C, the required conditions of which are not harsh [51]. Taking vanadium dioxide as an example, the abrupt changes in optical properties during the phase transition (such as the transmission and reflection of infrared lights) and the change in conductive properties promise excellent thin film sensors. Specific to the vanadium dioxide (VO<sub>2</sub>) that this work mainly involves, it presents a very significant two-state difference in electrical and optical properties. For example, at room temperature, VO2 is not qualified as a conductive material (density of states at insulating state approaches 0 above the valence band) [28]. However, when it enters the metallic state through external stimuli such as thermal excitation, both electrical and optical properties change to a large extent. The electrical resistance of VO<sub>2</sub> experiences a sharp fall during the phase transition towards the metallic state from the magnitude of 10<sup>5</sup> to 10<sup>2</sup>, while light absorption at a specific waveband may increase [52]. For example, the absorbance of lights at 1.1~1.3 THz measured on VO<sub>2</sub>-based films approaches 0 at room temperature but increases to 1 when heating it up to around 350 K, which exhibits the significant contrast between its frequency response features depending on temperature [52].

The phase transition of VO<sub>2</sub> is described by the changes in its physical properties. With the maturity of fabrication technology and measurement methods [53, 54], the measurement of the physical properties of VO<sub>2</sub> such as the thickness of a specific VO<sub>2</sub> film sample and the transmission through it when illuminating the sample with lights of certain wavelengths become possible, which provides the basis for research on its phase transition. For example, by depositing VO<sub>2</sub> on the insulator substrate and integrating it with complex optical devices, physical parameters including the transmission, reflection, and absorption of certain kinds of light (such as light in the visible and near-infrared region) can be measured. Mainly with the ellipsometry, significant coefficients such as dielectric constants and complex refractive indices

can be obtained. The original data directly measured on the ellipsometer is the change in polarization as light reflects or transmits from the materials to be measured, then the amplitude ratio of polarization  $\Psi$  and phase difference  $\Delta$  are extracted [55]. To obtain complex refractive indices, which are the most important parameters for further analysis from optical perspectives, Lossy Lorentz oscillator model [56] and Drude model [57] are used to process the data (Lorentz model is used for insulating state and Drude model is used for metallic state). Below, I will introduce the phase transition in detail.

The phase transition of VO<sub>2</sub>, also known as the insulator-metal transition (IMT), refers to the physical transition from an insulator or semiconductor to a metallic conductor. Physically the phase transition can be summarized as a structural change in VO<sub>2</sub> crystals. The VO<sub>2</sub> crystals transform from monoclinic phase (vanadium atoms dimerize along crystallographic c-axis and lead to a distorted lattice as shown in Fig. 1) to tetragonal rutile phase (vanadium dimers break, which makes the lattice symmetric), which also brings changes in its density from 4.571 g/cm<sup>3</sup> to 4.653 g/cm<sup>3</sup> [58, 59]. Combining Fig. 1 with the concept of energy bands (refer to ranges of energy levels that electrons can occupy in a solid materials), many of the behavioural predications made in this thesis about VO<sub>2</sub> phase transition have the basic physical foundations. The relative positions of energy bands shown in Fig. 1(c) illustrate the essential difference between metals, insulators, and semiconductors, which also provides the method to change the phase of a certain material [60]. For example, the microstructural differences in Si can be achieved by changing its production process. Amorphous Si and crystalline Si have significant differences in both optical and electrical properties. Crystalline silicon can be divided into different types based on the geometric structure of its lattice (e.g. monocrystalline Si and polycrystalline Si. It is also possible to dope atoms like phosphorus and boron to make n-type or p-type mono-S) [61, 62]. In contrast to most dielectric materials, the phase transition of VO<sub>2</sub> is easily excitable and reversible, which provides large flexibility in the design of tuneable devices. In this chapter and the whole thesis, the transition from the insulator phase to the metal phase, and its inverse process, are both referred to as phase transition to highlight its characteristics [27].

Fig. 1 shows the change in lattice and energy band during the VO<sub>2</sub> phase transition with the aid of schematic diagrams [27]. Variations in external conditions, such as pressure and temperature, can significantly alter the lattice constant and structure, consequently shifting the positions of the energy bands. The positions of the energy bands directly determine how difficult the electrons move between different energy levels, which means the change in them shows up as huge differences in electrical properties. This internal reaction generates an energy overlap between the full band and empty band of the insulator or semiconductor, which eliminates the

forbidden band and transits to a conductor [63]. Conversely, when the overlapping energy bands are separated, a forbidden band appears, and the conductor becomes an insulator or semiconductor, which has different physical features [18, 27]. The main domain of changing windows can be determined by different fabrication processes and conditions of growth (e.g. the ratio of vanadium and oxygen in  $V_xO_y$  varies in the  $VO_2$  films produced at different pressure and temperature), which will be discussed in this thesis. It is particularly noteworthy that the variation in  $VO_2$  crystals occurs as a transition from a monoclinic distorted rutile structure to a tetragonal rutile structure, rather than undergoing a transition between amorphous and crystalline states. The lattice change shown in Fig. 1 can be excited by different methods. Among the various methods known to change the physical characteristics of  $VO_2$ , temperature control is considered an effective method to control the  $VO_2$  phase transition [64, 65].

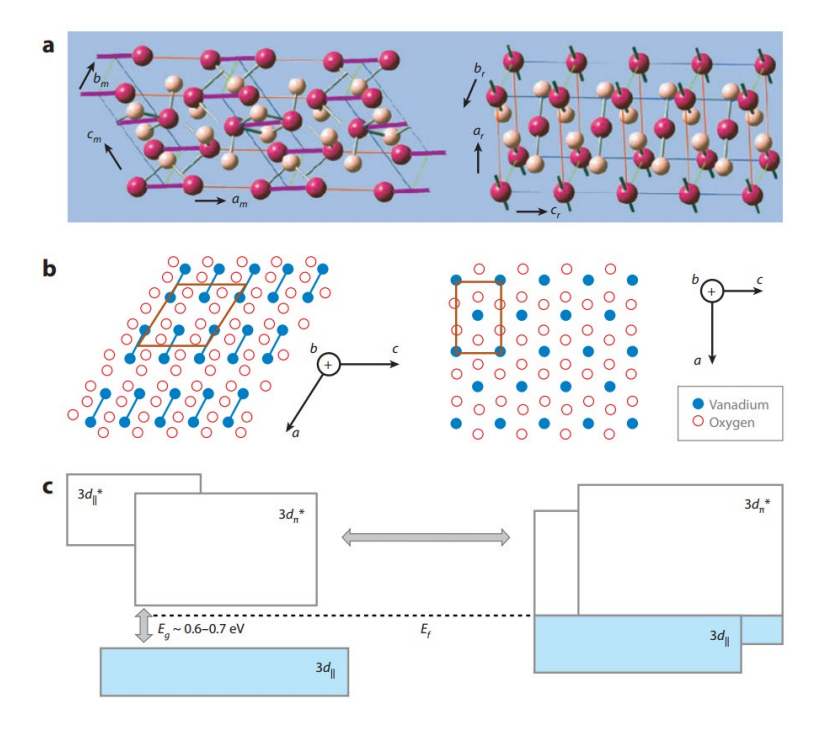


Fig. 1 Schematic diagram of insulator-metal transition of  $VO_2$ . (a) and (b) illustrate the structural crystal change from monoclinic insulator to tetragonal metal in the three-dimensional view and the cross-sectional view respectively. (c) shows the change in energy band during the insulator-to-metal transition. The elimination of energy gap can be observed by comparing the positions of energy bands before and after the transition. The figures (a)~ (c) are copied from [27].

#### 2.1.2. VO<sub>2</sub> photonics

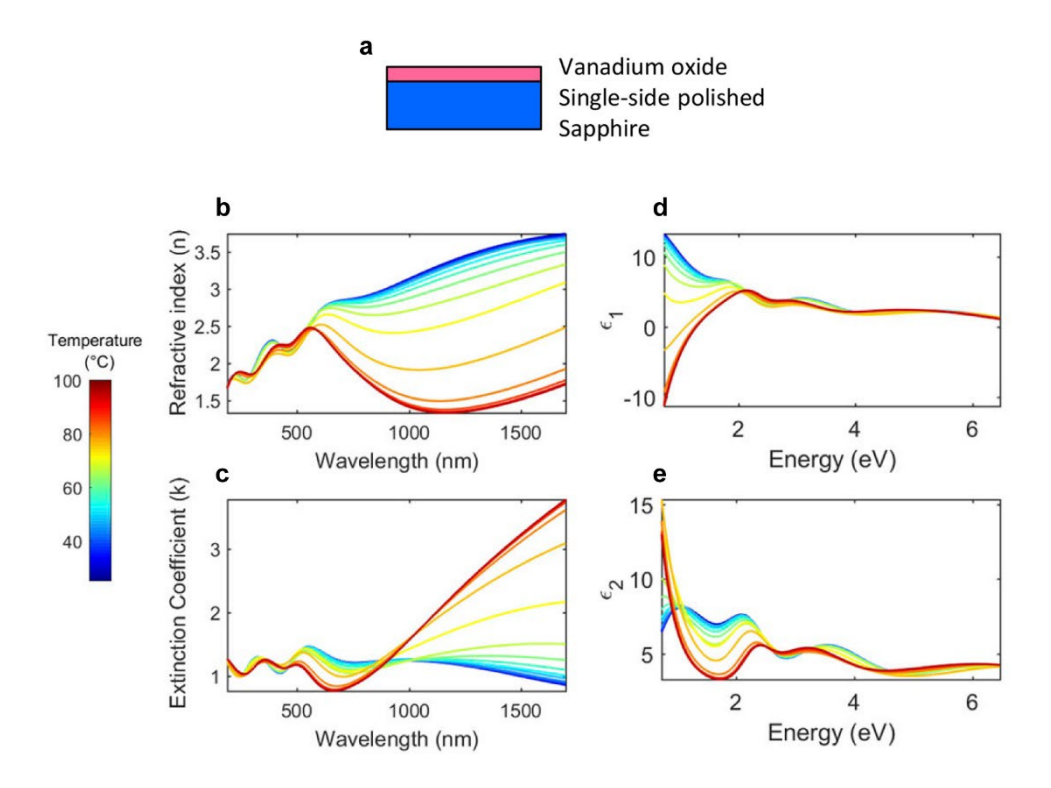


Fig. 2 Measurement of optical properties of VO<sub>2</sub> thin films through phase transition. (a) shows the layered structure of VO<sub>2</sub> films deposited on a single-side polished sapphire substrate. The thickness of film varies from 35.4 nm to 36.2 nm. Different optical parameters are measured and plotted in (b) refractive index n, (c) extinction coefficient k, (d) real part of permittivity  $\varepsilon_1$ , (e) imaginary part of permittivity  $\varepsilon_2$ . The figures (a)~ (e) are copied from [66].

The field of nanophotonics studies how light interacts with structures on the nanometre scale, where unique phenomena like plasmonic and subwavelength confinement arise [67]. It enables the manipulation of light in ways not applicable with larger-scale systems such as subwavelength modulation and metalens imaging. Applications include high-efficiency LEDs, advanced optical communications, nanoscale sensors, and enhanced solar energy harvesting are developed with the progress of nanophotonics [68]. Leveraging fabrication techniques that enable higher resolution of device designs and the modelling tools, nanophotonics is pivotal for innovations in optoelectronics, imaging, and energy technologies [69]. Many materials have been widely used in the design of nanophotonics such as Si (the most frequently used material due to its high refractive index and compatibility), GaN (used in LEDs and lasers for its efficient light emission properties), graphene (a typical 2D material enabling ultrafast and tunable optical devices) and other dielectric materials (TiO<sub>2</sub>, Si<sub>3</sub>N<sub>4</sub>, etc.).

VO<sub>2</sub> has attracted attention in the field of nanophotonics, mainly due to the fact that the optical properties of its thin films are relatively easy to predict [70, 71]. By using different deposition processes, post-processing conditions (for VO<sub>2</sub>, it is annealing while crystallization is necessary for Si), combinations of substrate materials and doping with other materials, a variety of tunable structures have been designed to study the optical properties of VO<sub>2</sub>, thereby providing a theoretical basis for the subsequent development of more complex devices [54]. Spectroscopic ellipsometry is widely used to measure optical parameters such as refractive index and dielectric constants in the visible, near-infrared and mid-infrared bands [55, 72, 73]. On this basis, some structures with special frequency response characteristics were designed, including infrared absorbers and reconfigurable multi-wavelength blockers. In this section, I list a few representative nanophotonic devices to explain how VO<sub>2</sub> and its phase transition properties are applied.

The first focus of research on VO<sub>2</sub> nanophotonics is the temperature-dependent change in refractive index. Fig. 2 shows a work that analyses a series of optical properties of VO<sub>2</sub> thin films by using spectroscopic ellipsometry [66]. A simple VO<sub>2</sub>-based structure is proposed to measure the physical parameters. In this model, a thin VO<sub>2</sub> film with a thickness between 35.4 nm and 36.2 nm is deposited on a single-side polished sapphire substrate by ion beam sputtering. This VO<sub>2</sub>-Al<sub>2</sub>O<sub>3</sub> double-layer structure exhibits significant temperature-sensitive changes in optical properties including the refractive index, extinction coefficient and complex permittivity. In Fig. 2(b) and (c), the blue curves represent the frequency response of refractive index n and k at room temperature while the red curves correspond to that of high temperature. Several intermediate states are measured to show how the refractive index changes during the heating process. The optical response over the wavelength from 193 nm to 1690 nm is measured, which includes the ultraviolet, visible and near-infrared bands. It can be seen that the VO<sub>2</sub> phase transition contributes to a large contrast among the refractive index n and k at different temperatures in the visible to near-infrared band, while the temperature dependence is not as significant in the ultraviolet band [74, 75].

Combining with the results provided by [64, 70, 71, 76], which also lists research on the frequency response of VO<sub>2</sub>-based devices at different wavelength bands. An important observation can be drawn that during the last two decades, frequency of the light interacts with the device and work temperature are two most important variables in the design and characterisation of VO<sub>2</sub> films. In judiciously designed nanodevices, VO<sub>2</sub> can induce large sensitivity to both temperature and frequency changes [27]. Therefore, when discussing the physical properties of VO<sub>2</sub>, these two parameters can be used as variables to establish a 2D element library.

Besides the tunable refractive index, another essential feature of VO<sub>2</sub> during its phase transition is the hysteresis phenomenon, which can be summarized as the trajectories of a certain physical indicator changing with temperature during heating and cooling process don't overlap. Fig. 3 below demonstrates a design that utilises the thermal hysteresis properties of VO<sub>2</sub> phase transition to achieve specific phase control, thereby providing a functional basis for fabricating imprinted reconfigurable photonic devices [77]. Fig. 3(a) shows an embedded structure. With the support of continuous ion beam implantation technology, VO<sub>2</sub> nanocrystals with an average diameter of about 90 nm are buried in a fused SiO<sub>2</sub> substrate that is about 0.5 mm thick. The ratio of oxygen in the  $VO_x$  (for pure  $VO_2$ , the value of x is theoretical equal to 2. When x is not equal to 2, there might be impurities like  $V_2O_5$  in the mixture) is finally determined by rapid annealing at 1000 °C for 10 minutes. After these process procedures, these VO<sub>2</sub> nanocrystals can have the typical phase transition characteristics. The heating of this structure is implemented by optical illumination. A continuous-wave 532 nm pump laser is used to locally induce the phase transition, and the illumination time is precisely controlled by a mechanical shutter. A 1550 nm laser source is used to probe the phase and intensity during the phase transition, which provides the data to plot the hysteresis curves.

From Fig. 3(b) and Fig. 3(c), VO<sub>2</sub> nanocrystals exhibit a very wide hysteresis window (the temperature difference between the heating and cooling trajectories when the measured physical quantity reaches the same corresponding value) during the cooling process [78, 79]. It has a significantly large dielectric contrast between the metallic and the insulating state. In addition, the VO<sub>2</sub> nanocrystals fabricated in this work show a certain extent of robustness, which supports the structure to work for highly repetitive (>100) cycles through the phase transition without any structural damage. This work mentions another method for inducing VO<sub>2</sub> phase transition besides temperature, namely the pump irradiance, which uses the pump laser generate to illuminate the VO<sub>2</sub> sample. A variety of methods are used for the excitation of the phase transition, but ultimately, they are used to effectively control the properties of VO<sub>2</sub> to achieve different optical designs and applications. As a result, this thesis will focus on the form of temperature control.

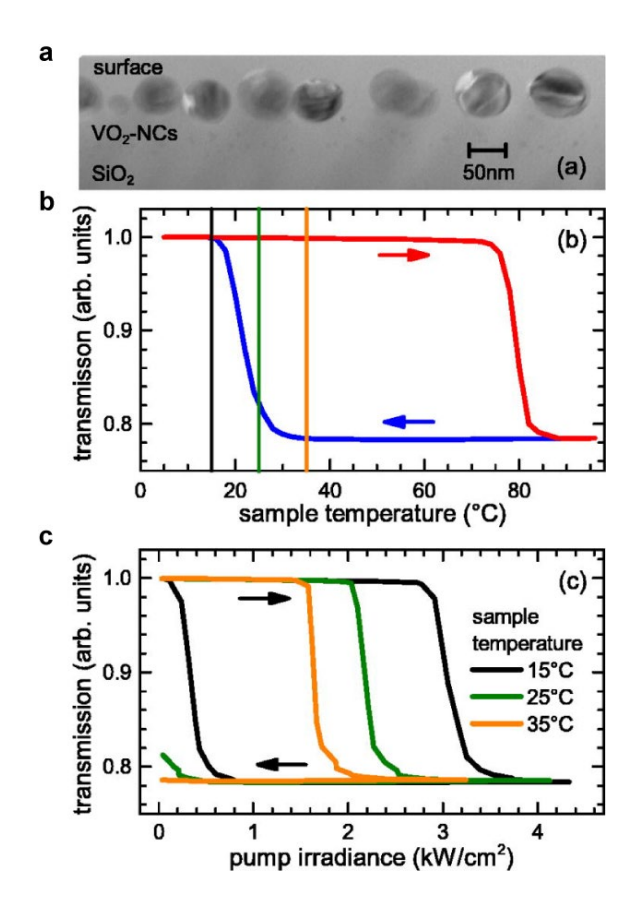


Fig. 3 Thermal hysteresis of VO<sub>2</sub> nanocrystals exhibited by transmission changes.

(a) TEM image of ion beam synthesized  $VO_2$  nanocrystals buried in a fused glass matrix. The cross-section is shown with a scale bar of 50 nm. A continuous-wave (CW) 532 nm pump laser is used to excite the phase transition, and a 1550 nm laser probe is used to collect momentary data including the intensity and phase of transmitted light. (b) shows the transmission recorded during the heating and cooling process. (c) shows three hystersis graphs that are produced by capturing data measured at three different temperatures as shown in (b). The figures (a)~ (c) are copied from [77]

In addition to temperature-sensitive optical properties and thermal hysteresis, another reason why VO<sub>2</sub> has attracted attention in the field of nanophotonics is the large contrast in its frequency response characteristics exhibited in different phases. This feature is widely applied in amplitude modulation in the visible and infrared bands, and the most typical application is full absorbers/ zero reflectors. Fig. 4 shows a VO<sub>2</sub>-based absorber that can be tuned between low and perfect absorption of incident light at specific wavelengths [80]. As shown in Fig. 4(a), a VO<sub>2</sub> layer of 180 nm is deposited on a c-plane sapphire substrate, which is a very common design as shown in Fig. 2. The thickness is determined according to the requirements of the lossy medium to form an asymmetric Fabry-Perot (FP) cavity (a device designed to produce

interference patterns by reflections between two parallel mirrors. The dimensions should be determined according to the wavelength of the light to control), aiming to completely confine the incident light within the medium [81]. To characterise the performance of this absorber, Fourier transform infrared (FTIR) spectrometer and mid-IR microscope are used to measure the absorption at normal incidence in a broad wavelength band from 2 µm to 15 µm. The phase transition of VO<sub>2</sub> is enabled by the temperature control plane placed at the bottom of the sapphire substrate. At the same time, this plane also has the function of blocking transmission, so the absorption status can be judged directly by observing the reflectivity. Since FTIR has a wide wavelength measurement range, continuously changing broad-spectrum measurement results can be obtained by combining different light sources [82].

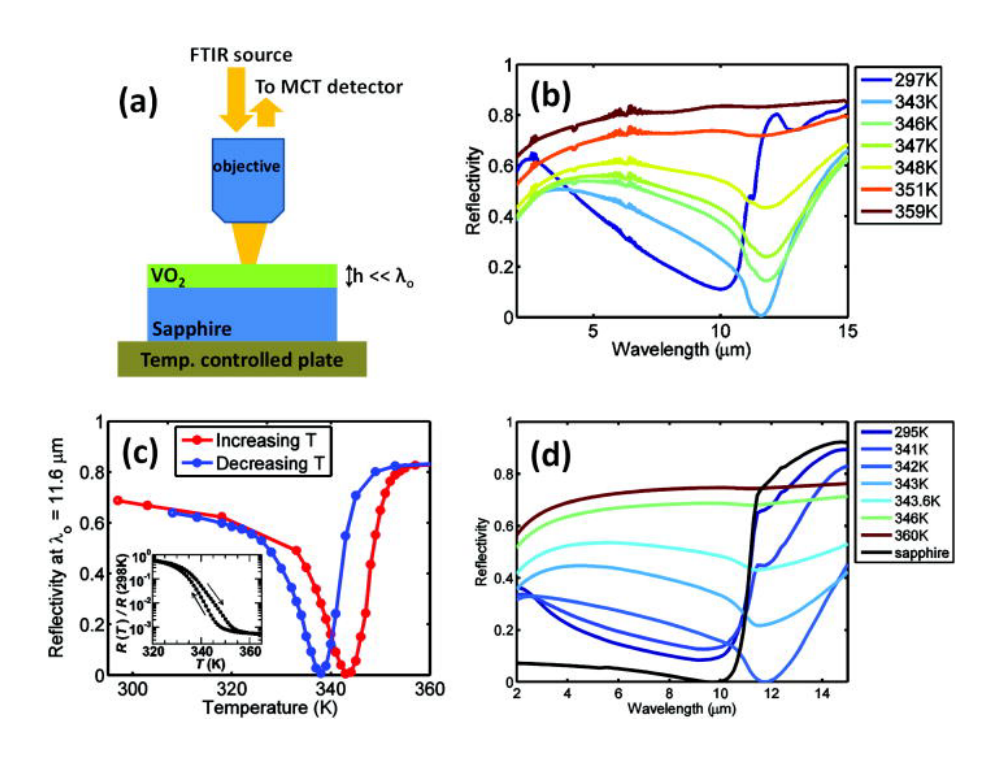


Fig. 4 Characterisation of a tuneable absorber based on VO<sub>2</sub> phase transition.

(a) Schematic diagram of the experiment setup to characterise the absorber. The absorber is a film device consisting of two layers. A VO<sub>2</sub> film of 180 nm is coated on the sapphire substrate to implement the tuning of absorption. (b) Experimental reflectivity spectra at temperature from 297 K to 360 K. At 343 K, a reflectivity valley appears at close to the wavelength of 11.6  $\mu$ m. (c) Data of reflectivity against temperature extracted at 11.6  $\mu$ m from the full-wavelength spectra. (d) Calculated reflectivity spectra at temperature from 295 K to 360 K. Bare Sapphire film is also measured for comparison. The figures (a)~ (d) are copied from [80].

Fig. 4(b) and Fig. 4(d) show the reflectivity spectra obtained by FTIR measurement and

calculation based on extracted physical parameters respectively. The FTIR works based on the fact that molecules vibrate at their characteristic frequencies under the infrared radiation. For a FTIR, a beam splitter is used to produce two light paths, and the reflected beams recombine to create an interference pattern, which is unique for a certain structure and a certain material. Then with post-processing assisted by physical models, different physical parameters are derived from the raw data. At each specific wavelength, there is a corresponding pair of hysteresis reflectivity graphs measured at the heating and cooling process as shown in Fig. 4(c). In the experimental group, a reflectivity of  $\sim 0.25\%$  (corresponds to 99.75% absorption) is measured at 343 K when the wavelength of incident light is 11.6  $\mu$ m. For the theoretical calculation group, the minimum reflectivity is  $\sim 0.07\%$ , which is observed at 342 K, and the wavelength is 11.75  $\mu$ m. The difference between the results of experimental measurement and analytical calculation is very small, which supports the conclusion that a tuneable perfect absorber based on VO<sub>2</sub> is achieved in this work.

Different from the work shown in Fig. 2 and Fig. 3, this work starts with theoretical calculations to find a specific double-layer structure that can achieve perfect absorption at certain wavelengths and supports the feasibility of this design through mutual verification of theoretical and experimental measurement. It provides a very versatile solution for the subsequent design of binary tunable VO<sub>2</sub> devices.

To summarize the very basic theoretical backgrounds about the VO<sub>2</sub> photonics, its frequency-response shows a strong dependence on the temperature (and the most important parameter to explore on is the tunable refractive index, which is the basis for the design of optical devices), and the change has obvious hysteresis features. Besides, it has the potential to design full-absorptive devices, which means the energy contrast between different states is very large.

#### 2.2. Effective medium models (EMM)

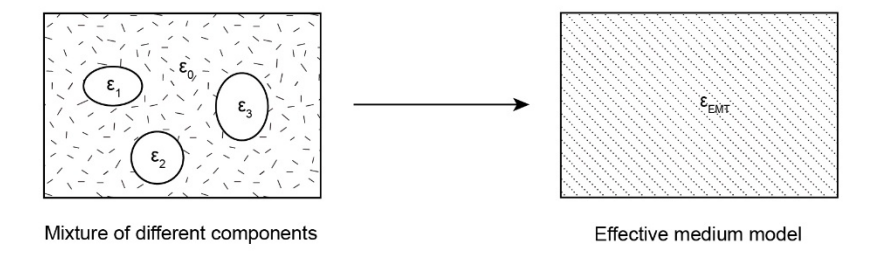


Fig. 5 The effective medium approximation for continuous multiple composites.

The mixture of four different materials is approximated as a homogenous medium.

The shape and dimensions of the impurities are taken into account in some EMM.

Effective medium theories (EMTs or EMT in short), also known as effective medium approximations (EMA), are originally proposed to describe the macroscopic characteristics of composite materials [83]. After being verified and developed in application scenarios, effective medium theories are widely used to predict and interpret the electromagnetic properties of composite materials that consist of two or more different constituent materials [84]. Although differ in detailed analytical approaches, these theories share a common and fundamental assumption: the two constituent materials are well mixed, making the whole mixture perform effectively as a homogenous, new kind of medium, which explains why it is named an effective medium [85, 86]. In an analytical sense, the definition of effective medium refers to the process of establishing a distribution model, assuming that a composite medium is in a doping state of a certain amount of inclusions randomly distributed in the intrinsic material [87]. One of the essential condition that a mixture can be regarded as the effective medium is, it doesn't matter how inclusions are distributed in this mixture. The electromagnetic properties of this effective medium can be affected by factors including the intrinsic properties of the constituent materials, their volume ratio, and the microscopic structure. The idea of EMT is in fact very general. For example, Lorentz proposed that the very foundation of macroscopic Maxwell electrodynamics itself can be regarded as a kind of EMT description based on the average theory [85]. Partly due to their importance and wide range of use, many different EMTs have been developed over the past half a century. Some EMTs have become popular in specific niche fields of research [87-89]. Specific to my PhD project, which concentrates on the material of VO<sub>2</sub>, several EMTs are noticeable, which include the Maxwell-Garnett equation [90], the Bruggeman model [91], and Looyenga's mixing rule [92].

At the beginning of EMT research, the Maxwell-Garnett formula was widely used. As a brief explanation, the theory treats inclusions as spheres or ellipsoids (this is actually in line with the description of the internal structure of atoms or molecules from a microscopic point of view) [4]. Subsequently, by focusing on polarizability, the theory derives an effective dielectric constant based on electrostatics analysis. The fundamental expression of Maxwell-Garnett used to predict the effective permittivity of a composite formed by two constituents can be written as:

$$\varepsilon_{eff} = \varepsilon_2 \frac{\varepsilon_1 (1 + 2f) + \varepsilon_2 (2 - 2f)}{\varepsilon_1 (1 - f) + \varepsilon_2 (2 + f)}$$
(3)

where f is the volume fraction (or filling factor) of the constituent  $\varepsilon_1$ . This theory nevertheless has a fundamental flaw. Following its analysis, particles (the inclusions) that distribute

randomly in the host material (the matrix) will always retain their role as the inclusions in the equation, even if the inclusions have increased significantly in their volume and have formed a matrix by themselves [3]. This problem of the Maxwell-Garnett formula was later addressed by Bruggeman, who discovered an approximation to treat the two composites symmetrically [85].

The starting point of Bruggeman's theory is to simplify the material in the mixing state into a binary system, that is, in a homogeneous system composed of an effective medium, spherical inclusions with an independent dielectric constant different from the intrinsic medium are embedded, which is shown in Fig. 10 [3, 93]. Describing Bruggeman's hypothesis from a general point of view, it mainly averages two or more components with different dielectric constants in the mixture according to a certain volume fraction-related law, so that the mixture can present the physical traits as a single material.

The specific procedures to derive the Maxwell-Garnett equations are from [4]. This thesis will put emphasis on the developed form of Bruggeman's model. To outline the guiding line of Bruggeman's theory, the most essential contribution to the development of EMT is the hypothesis that average flux deviations passing through the inclusions in the whole system should be equal to zero. This assumption is proposed based on optimal circumstances where no single-particle polarizations exist in an effective medium to interrupt the calculations [94, 95]. To a certain extent, this assumption avoids scenarios where the Maxwell-Garnett equation is not applicable. Though Bruggeman's model has developed a series of different forms of functions, this work uses the most widely known form that describes the effective medium, which can be expressed as:

$$f_1\left(\frac{\varepsilon_1 - \varepsilon_{eff}}{\varepsilon_1 + 2\varepsilon_{eff}}\right) + f_2\left(\frac{\varepsilon_2 - \varepsilon_{eff}}{\varepsilon_2 + 2\varepsilon_{eff}}\right) = 0 \tag{4}$$

Where  $f_I$  and  $f_2$  are the volume ratio of the two components in the composite material like the volume fraction factor f in the Maxwell-Garnett equation,  $\varepsilon_I$  and  $\varepsilon_2$  represent the dielectric constants of the two components respectively. In addition, what makes Bruggeman's model distinct from classic theories such as the Maxwell-Garnett formula is, that Eq. (5) gives rise to a critical threshold, which can be generalized to include a larger number of components without theoretical difficulty:

$$\sum_{i} f_{i} \left( \frac{\varepsilon_{i} - \varepsilon_{eff}}{\varepsilon_{i} + 2\varepsilon_{eff}} \right) = 0$$
 (5)

In addition, there are also other forms of Bruggeman's model, some of which define more than

one free variable besides the volume fraction parameter f. Difference between these BMM is mainly proposed based on different microscopic assumption of particles. So the factors introduced are mostly relative to the geometric parameters. For example, when the inclusion particles are modelled as ellipsoids, the depolarization factor along the long side of the ellipsoids q can be taken into consideration, and a different form of Bruggeman's model can be expressed as:

$$f_1\left(\frac{\varepsilon_1 - \varepsilon_{eff}}{\varepsilon_{eff} + q(\varepsilon_1 - 2\varepsilon_{eff})}\right) + f_2\left(\frac{\varepsilon_2 - \varepsilon_{eff}}{\varepsilon_{eff} + q(\varepsilon_2 - 2\varepsilon_{eff})}\right) = 0$$
 (6)

As will be seen in results of reflectance extracted from theoretical models in section 4.1.3, in addition to the Bruggeman model, the Looyenga model is the other EMT that is used to compare with the VGM that I propose. The mixing formula was proposed by H. Looyenga in 1965, originally only for calculating the dielectric constants of heterogeneous mixtures [92]. Several different forms of the original formula have subsequently been developed. In the context of VO<sub>2</sub>, where the effective medium is a mixture of the insulating and the metallic phases, a general form of Looyenga's mixing formula can be expressed as [96]:

$$\varepsilon_{eff}^{S} = (1 - f) \cdot \varepsilon_{ins}^{S} + f \cdot \varepsilon_{met}^{S} \tag{7}$$

where  $\varepsilon_{ins}$ ,  $\varepsilon_{met}$  and  $\varepsilon_{eff}$  respectively represent the permittivity of the insulating phase, metallic phase and the effective medium. S is a geometric parameter. For a block material, S takes the value of 1, while it takes the value of 1/3 for thin films [97]. The original version proposed by Looyenga [92] uses 1/3 for S parameter, which is the main basis that I use the same value in my work. Considering the consistency between different kinds of EMM as the compared target (the introduction of q factor makes it different in algebraic degrees of freedom for Looyenga's model and Bruggeman's model, which contributes to calculation errors), the Bruggeman's model used for analytical calculation in the methodology and results chapter only refers to the version that Eq. (4) describes [85].

This change in value is associated with the fact that the inclusion may not be completely surrounded by the host matrix in thin films. To verify the universality of this model in the study of  $VO_2$ , I select a definition function of f(T) for numerical analysis to explain how temperature is relative to the filling factor (share of the impurities), which can be expressed as [96, 98]:

$$f(T) = \frac{1}{1 + \exp\left[\frac{W}{k_B}(\frac{1}{T} - \frac{1}{T_{half}})\right]}$$
(8)

where W is a coefficient that describes the width of the temperature domain of the phase transition and  $T_{half}$  is the temperature at which half of the volume of the VO<sub>2</sub> film is in the metallic phase. The equation is modified from Eq. (5). Due to the existence of thermal hysteresis in  $VO_2$ , the value of  $T_{half}$  is different for the heating and cooling process [99]. In order to verify the reliability of this formula in analytical calculations involving EMM, I cited the VO<sub>2</sub> films and the correlative parameters in a literature for reproduction [96]. In this work, 1550 nm light source is used due to its versatility in near-infrared communications. The parameters required are measured from a sample of VO<sub>2</sub> thin films of 70±9 nm grown on the native oxide dielectric on a Si substrate, which is an example only used in this section [96]. The synthesis method is magnetron sputtering. Magnetron sputtering is a specific type of PVD that is widely used for coating and deposition of thin films. Materials are ejected from a target (cathode) by bombarding it with high-energy ions, typically from a plasma generated in a vacuum chamber. A magnetic field near the target confines the plasma, increasing ion density and sputtering efficiency. The ejected atoms travel through the vacuum and condense on a substrate, forming a uniform thin film. This method allows precise control over film composition, thickness, and morphology, making it ideal for applications in semiconductor devices [100, 101]. The necessary parameters for calculations and verifications according to Eq. (8) are listed in the table below. Parameters of other films constructed by different fabrication methods are also listed. Film 1 to 3 are all deposited by magnetron sputtering with different thicknesses and substrate materials, while film 4 is obtained by sol-gel method.

Table. 1 List of parameters of different films (n and k values are for wavelength of 1550 nm) [96]

	Film1	Film2	Film3	Film4
W (heating) (eV)	3.37	3.57	4.85	9.60
W (cooling) (eV)	2.75	3.79	4.15	7.14
$T_{half}$ (heating) (K)	351.5	351.1	348.1	345.1
$T_{half}$ (cooling) (K)	340.1	339.0	345.2	338.7
n (insulating)	2.88	3.01	3.23	2.98
k (insulating)	0.36	0.61	0.51	0.20
n (metallic)	1.58	1.35	1.34	1.84
k (metallic)	2.63	2.66	2.67	2.85

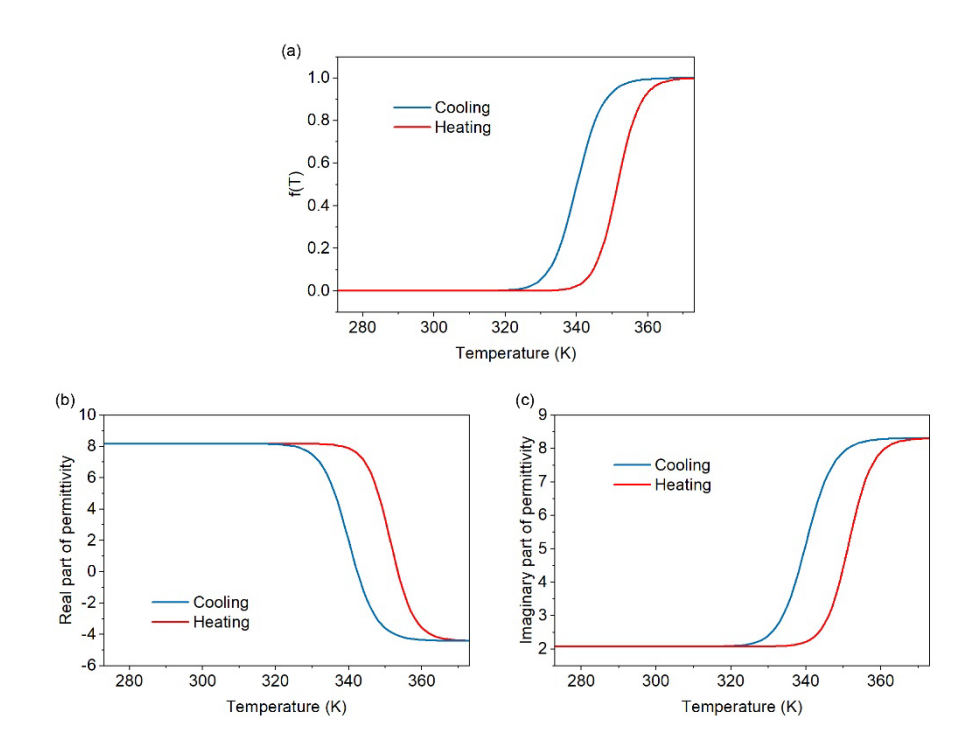


Fig. 6 Extraction of temperature-dependent parameters based on literatures. (a) Temperature-dependent volume fraction function f(T) from 273 K to 373 K. (b) and (c) Real and imaginary part of permittivity of VO<sub>2</sub> from 273 K to 373 K. Hysteresis characteristics can be observed in all three graphs.

From Eq. (7) and Eq. (8) and the parameters in the table, the model of volume fraction f(T) against temperature (298 K ~ 373 K, which is 25 °C ~ 100 °C) and the model of permittivity of 1550 nm light source against temperature (273 K ~ 373 K, which is 0°C ~ 100°C) are built to do further analysis. Note that the heating and cooling processes are separately considered to observe the influence of hysteresis. The graphs output is shown in Fig. 6. The temperature-dependent change in the filling factor f(T) shows high consistence to the change in permittivity, which includes the starting point, ending point and the width of temperature window of phase transition. The curves of f(T) and permittivity during the heating and cooling process show very typical hysteresis characteristics and ideal trend for polymerization at both ends of the transition [98, 102].

The most important output of reproducing results of the work from [96] is to build the numerical relationship between the filling factor f and temperature T. The volume fraction or filling factor f is a parameter that is challenging to directly measure under current technical conditions [103]. However, it is easy to set f as the main variable when theoretical models are used to predict the change in physical properties like refractive index during the phase transition. Temperature, on the other hand, is a parameter that is relatively easy to monitor in the experiment. However,

introducing a thermal parameter into an optical model will greatly increase the complexity of the numerical simulation or analytical calculations. As a result, it is necessary to establish a correlation between temperature and filling factor so that the values of f and T can accurately correspond to each other at the formula level. This explains why Eq. (8) is particularly important when analysing effective medium theories and other theoretical models.

#### 2.3. Overview of fundamental optical systems

#### 2.3.1. The focusing and zooming implemented by geometric optics

In this section, I briefly introduce some representative designs in the field of geometric optics to explain how focusing and zooming are implemented in conventional optical systems. Geometric optics [104, 105] is a branch of optics that simplifies the behaviour of light to rays, which makes it easier to explain the implementation of focus and zoom.

Before the  $20^{th}$  century, the concept of focusing was limited to the basic theory centred on the linear propagation of light. The core components used in geometric optics are converging and diverging lenses [105]. Converging lenses (convex) bring parallel rays towards each other, converging at the focal point. Diverging lenses (concave) cause parallel rays to appear divergent as if they originated from the virtual focal point. In a converging lens, parallel rays of light converge at a specific point called the focal point. The distance from the lens to the focal point is the focal length. In a diverging lens, the extension of backward-traced rays appears to converge at a virtual focal point. By summarizing the experience of using these lenses, the thin lens equation [106, 107] was proposed to describe the focusing phenomenon and relate the object distance u, image distance v, and focal length fl, which can be expressed as:

$$\frac{1}{fl} = \frac{1}{u} + \frac{1}{v} \tag{9}$$

Besides focusing, another essential function of lenses is zooming. Zooming in an optical system involves changing the effective focal length. Zoom lenses achieve this by having multiple lens elements that can be repositioned to alter the overall focal length. By adjusting the lens elements, the optical system can provide variable magnification without physically changing lenses [108, 109]. In the design of traditional optical systems, the size of the whole system is usually not a primary concern, so zooming is commonly realised by the movement of mechanical components. The same happens in the field of microscopy [110], where zooming can be achieved by changing the distance between multiple lenses. To reduce the number of free variables, many classic lens designs mainly use spherical lenses, with only a small number of

aspherical lenses for the correction of aberrations to improve the resolution [111]. It's important to note that while geometric optics provides a simplified model for understanding focusing and zooming, actual optical systems may involve additional considerations such as aberrations, diffraction, and the wave nature of light.

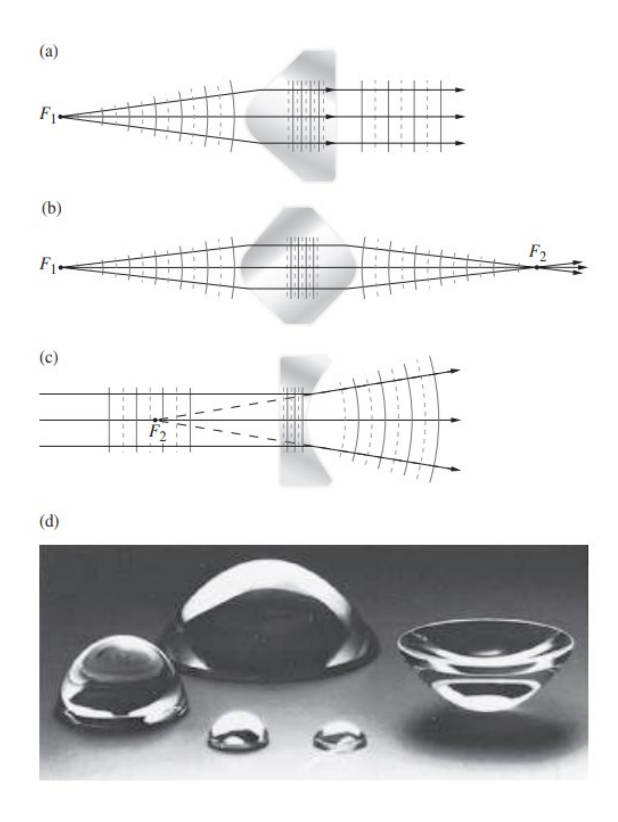


**Fig. 7 Several examples of single-piece lenses**. (a-c) Schematics revealing the optical paths of several lenses. (d) A photo of several lens examples. The figures (a)~ (d) are copied from [112].

By analysing the propagation characteristics of light waves, many types of optical devices have been designed. They appear in various forms, such as glass lenses, metallic mirrors and glass prisms [112]. Complicated optical and optoelectronic devices such as optical fibre systems, phase-controlled array radar, digital single-lens reflex cameras (DSLR), microscopes, telescopes and adaptive-optics systems with feedback are all developed based on these fundamental optical elements [113, 114]. These products can be considered an extension of the basic principles of geometric optics and also represent the development and exploration of focusing and zooming properties from the perspective of traditional optical systems.

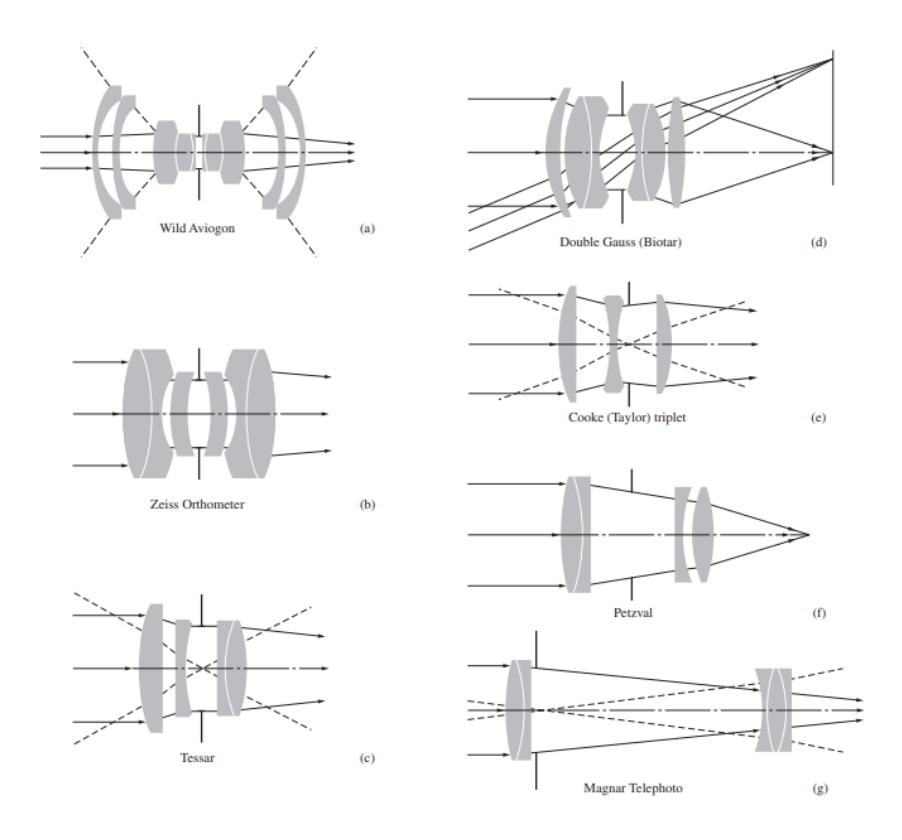


**Fig. 8 A selection of famous camera lenses design**. (a) Wild Aviogon, axisymmetric refractive system appears in 1950s. (b) Zeiss Orthometer, axisymmetric refractive system appears in 1960s. (c, d) Tessar and Double Gauss (Biotar) implement high image quality with less lens pieces, which are still commonly used nowadays. (e) Cooke (Taylor) triplet is an excellent objective design first appeared in 1893, which can effectively eliminate distortions and aberrations at the corner of lens. (f, g) Petzval and Magnar are two early design prototypes released in 19<sup>th</sup> century. The figures (a)~ (g) are copied from [112].

By analysing these systems in detail, it can be found that most of them involve wavefront control in two or three dimensions [115]. That is monitoring and reshaping the wavefront in a plane or space. Starting from Snell's law [116], for a lens that is an aspherical optic made of one single medium, the shape of the lens directly determines the direction of the optical path inside this medium, thereby affecting the wavefront distribution of the transmitted light. A multiple-piece optical system also needs to consider the optical path among multiple lenses [117, 118]. Fig. 7 gives some examples of aspherical single-piece lenses [112]. Because most of the traditional lenses adopt silica that has good transmission characteristics as the building material, the energy dissipation and attenuation of visible lights passing through the singe-piece lens is negligible.

A composite optical system can be viewed as an assembly of many of these thin lenses, where individual lenses follow Eq. (9) independently. The designed output can be obtained by applying this equation multiple times to describe the whole system. A typical example of this lens design approach is digital single-lens reflex cameras (DSLR) lenses and mirrorless camera lenses. In these complicated mechanical devices, spherical lenses, aspherical lenses and other special lenses (e.g., extra-low dispersion (ED) glass lenses) are arranged by certain patterns. Fig. 8 shows some examples of composite lens designs. Positions of some of the lenses are fixed such as the front and rear lenses, while some others are movable and can be driven either by manual operation or by motors with a very fine stroke [112]. In recent years, there have been two main directions for the design of conventional optics. (a) Optimising the propagation path of plane waves with the help of technological progress in manufacturing, thereby minimizing the aberration caused by lenses. This approach targets diffraction-limited resolution [119, 120]. (b) Sacrificing the size of the image field and image quality for obtaining a small device form factor [121, 122]. This second direction is suitable for compact camera lenses where the lens diameters have been reduced to the millimetre level.

#### 2.3.2. From refractive optics to diffractive optics

Except for some simple designs such as single-piece reflectors, which are based on the reflection principle, the vast majority of conventional optical devices should be classified as refractive optics (especially complex imaging systems, which involves tens or hundreds of pieces of lenses to implement the refraction). Refractive optics primarily relies on the phenomenon of refraction, where light changes direction as it passes through different media. This is typically achieved using lenses made of transparent materials like glass or high-transmission plastic. By combining converging and diverging lenses, the path of light can be manipulated. Among the methods to control the light path, The bending of light is governed by Snell's Law [116], which relates the angles of incidence and refraction to the refractive indices of the media. The basic formula can be expressed as:

$$n_1 sin\theta_1 = n_2 sin\theta_2 \tag{10}$$

where  $n_1$  and  $n_2$  represent the incident index and refractive index respectively, and  $\theta_1$  and  $\theta_2$  correspond to the incident angle and refracted angle. Through this basic formula, many complex optical systems can be decomposed into refraction problems occurring on many refractive interfaces, and complex analytical operations can be performed on these systems through iterative calculations.

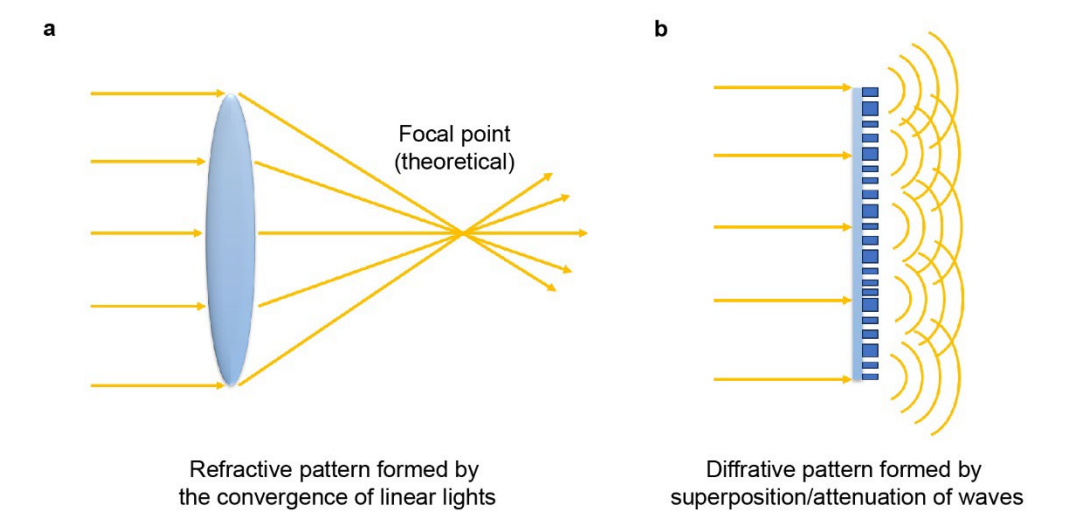


Fig. 9 Schematic comparison between refractive optics and diffractive optics. (a)

Under ideal circumstances (the light source is strictly monochromatic light), the lights passing through the lens converge to the focal point due to bending. (b) For diffractive lenses, light passing through the gratings or other 2D structures contribute to the diffraction waves. The diffractive pattern is formed by superposition and attenuation of these waves. The focus can be judged by analysing the intensity distribution.

In the development of refractive optics, the Fresnel lens is a representative single-piece lens design [123]. Instead of having a solid, thick lens, a Fresnel lens is composed of a series of concentric rings or grooves on a flat surface. These rings or grooves effectively divide the lens into multiple thin, stepped sections. The design is based on the principle that light waves can be redirected without the need for a solid lens. Each concentric ring or groove on the lens surface acts as a tiny prism, bending and focusing the incoming light, which is equivalent to wrapping the light distribution on a single lens with a huge curvature. The main advantage of the Fresnel lens compared to traditional lenses is obvious. To implement a similar focal length, the Fresnel lens significantly reduces the thickness and weight. At the same time, the Fresnel lens provides an example of the application of phase gradient that is widely used in modern lens design [124].

Based on the fundamental Fresnel lens, as the device size decreases and the lens order (the number of steps inside each groove) increases, the imaging quality of the refractive lens has significantly declined due to the influence of diffraction. On the other hand, as the wave characteristics of light have been explored for decades, diffraction characteristics are no longer simply considered a flaw, but also a feature to utilize in the design of lenses [125]. Unlike refractive optics, which rely on the bending of light through transparent materials, diffractive optics use the interference patterns that are observed when light passes through a structured

surface to achieve imaging [126, 127]. For imaging, an image can be regarded as an array of information expressed by different transmission intensity and phase values. When the information is input and goes through the optical system and then received at the output terminal, the imaging function is implemented by coding/decoding or other messaging process. Fig. 9 illustrates the main functional difference between diffractive and refractive lenses [128]. In refractive optics, a light source can still be described by innumerable straight-line light paths, and they will maintain their straight-line propagation characteristics when passing through the lens or optical system (but the propagation direction and intensity will change). In diffractive optics, the lights transmitting the lens will be regarded as point light sources, which exhibit obvious characteristics of waves. In practical use, due to the coupling of light sources of multiple wavelengths and the influence of external factors such as media, chromatic aberration cannot be completely avoided. Therefore, neither refractive optics nor diffractive optics can produce true point focusing.

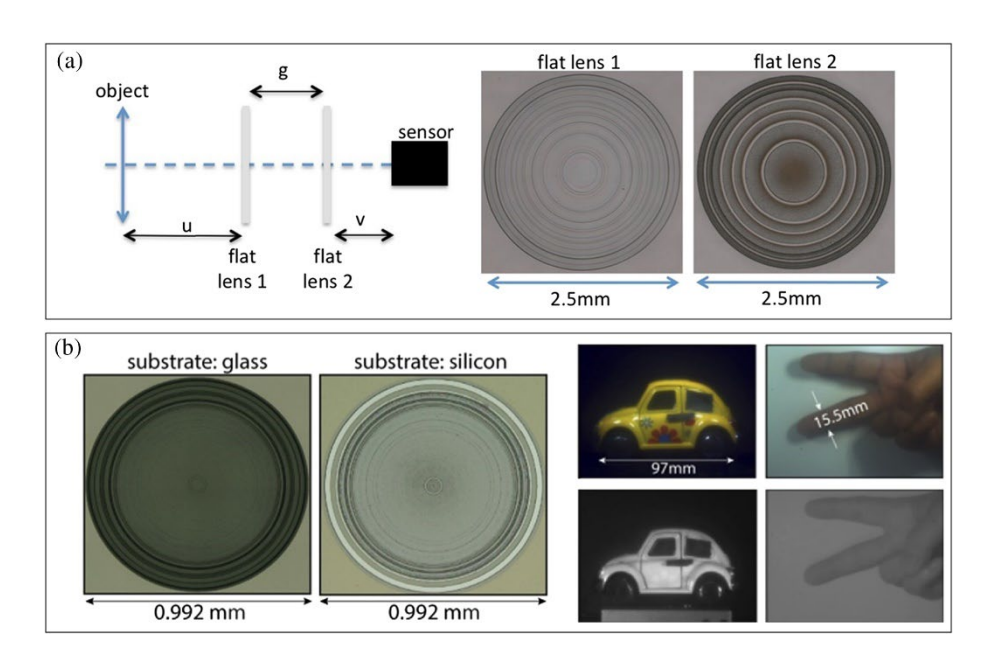


**Fig. 10 Two application examples of diffractive optics.** (a) Concatenated milli scale lenses. The imaging function is implemented by two flat lenses. The structural dimensions and numerical aperture (NA) can be optimised with the aid of improved fabrication processes. (b) A diffractive optical system that integrates multiple functions of traditional optics. This lens implements the correction of chromatic aberrations over broadband and can still maintain a high NA level (~0.81). The diffractive lenses shown in (a) and (b) use similar structures but different substrate materials. Silica is used for visible and infrared bands while Si is used for other wavelengths. The figure (a) is copied from [129]. The figure (b) is copied from [128].

Combining the two cases of diffractive optics shown in Fig. 10, several significant design features compared to refractive optics can be found through comparison: (i) Refractive optics tends to suffer from chromatic aberration due to its wavelength-dependent nature, while diffractive optics can be designed to handle different wavelengths more uniformly. As a result, diffractive optics attract strong attention in the design of multiwavelength optical devices [128]. (ii) Diffractive optics provide relatively higher flexibility in terms of design (e.g., structure dimension) and can achieve complex optical functions in a single element or a few elements [125]. However, it may also introduce additional challenges, such as sensitivity to incident angles and manufacturing complexities.

Entering the 21st century, enhanced by the rapid development of micro and nano-fabrication techniques, the design potential of diffractive optics has been further exploited. Mainly benefit from the development of the following techniques, the limit of design of optical devices has been broadened to the subwavelength range, thus truly taking advantage of the features of diffractive optics: (i) Top-Down approaches represented by photolithography [130]. Lithography is a key procedure in the patterning process, which allows designing devices with smaller scales. Techniques such as deep ultraviolet (DUV) lithography, extreme ultraviolet (EUV) lithography and multiple patterning have allowed for the fabrication of smaller and more intricate features on semiconductor chips, enabling the continued miniaturization of electronic or optical devices. (ii) Bottom-up approaches, such as self-assembly and molecular nanotechnology, have gained prominence, which leverage natural forces to arrange nanoscale building blocks into desired structures, offering the potential for high-throughput and costeffective fabrication methods [131, 132]. (iii) 2D materials [133]. The rise of graphene has opened up new possibilities for nanofabrication. Techniques such as atomic layer deposition have been developed to deposit ultra-thin and conformal films, which exhibit different features from the block materials or thick-film materials. 2D materials are widely used to design metasurfaces, which becomes a key to improving the performance of diffractive optics.

With the support of these technologies and the complete theoretical background of diffraction optics, the concept of metalens was proposed and quickly put into research and application. The next section will detail the basic characteristics of metalens and list several types of metalens designed based on different imaging mechanisms.

### 2.4. Metasurfaces and metalenses

### 2.4.1. The applications of metasurfaces based on VO<sub>2</sub> phase transition

Metasurfaces represent a paradigm shift in the design of optical devices, offering control over

the properties of light with ultrathin planar structures [134]. These structures, typically composed of subwavelength units or nanostructures arranged in a two-dimensional array, allow for precise manipulation of the amplitude, phase, and polarisation of incident light. The functionality of metasurfaces arises from the tailored response of individual elements to the incident electromagnetic wave. By engineering the size, shape, and orientation of these metaatoms (in applications of metasurfaces, meta-atom is used to refer to the minimum repeating unit. Some literatures also use unit cell, which is used in lattice analysis to describe the periodic structure), functions including beam shaping, polarization conversion, and wavefront control can be achieved [135-137]. Metasurfaces offer a versatile platform for designing optical elements, such as lenses, holograms (a type of imaging system. Through arranging meta-atoms by a certain order, the information carried by incident lights is transferred and reshaped as specific patterns), and waveplates (a kind of device used to alter the polarisation state of the passing light. It provides a phase shift between the orthogonal components of the light), in a compact and planar form factor. In this section, I list two metasurface designs that provide references for their various applications. Through introducing these designs, how the tunability of VO<sub>2</sub> is applied to the metasurfaces will be detailed. And two of the most important features of the VO<sub>2</sub> that makes it popular in metasurface designs are the low phase transition temperature (easy-tuning) and ultrafast response to the temperature change.

Fig. 11 illustrates Mie-resonance tuneable metasurfaces that are based on the VO<sub>2</sub> phase transition [138]. Generally speaking, the metasurfaces are units arranged on a plane following specific rules. Many dielectric metasurfaces leverage the frequency response characteristics of materials, thereby exhibiting optical features highly dependent on wavelength. The metasurface shown in Fig. 11 have three layers: PMMA substrate (a transparent organic material that doesn't affect the transmission of lights), VO<sub>2</sub> film and Si pillars. It possess some characteristics: (i) The reversible and hysteresis tuning of the VO<sub>2</sub> phase results in transmission modulation by two orders of magnitude. (ii) The near-complete absorption has spectral tuning. The reconfigurable metasurfaces can be rebuilt to work across a broad band of wavelengths. This work provides an example of how to find a universal solution to light intensity modulation, which is to implement binary control over various wavelengths by tuning the dimensional parameters, structure, or material composition of the metasurface units. The involvement of VO<sub>2</sub> allows this modulation to be achieved at relatively low temperatures, and its reversible and hysteresis properties provide a high degree of flexibility in practical applications. For example, when an imaging system is applied to portable devices like mobile phones that usually work at a limited temperature range, we will expect the temperature window of the tuning to be as narrow as possible.

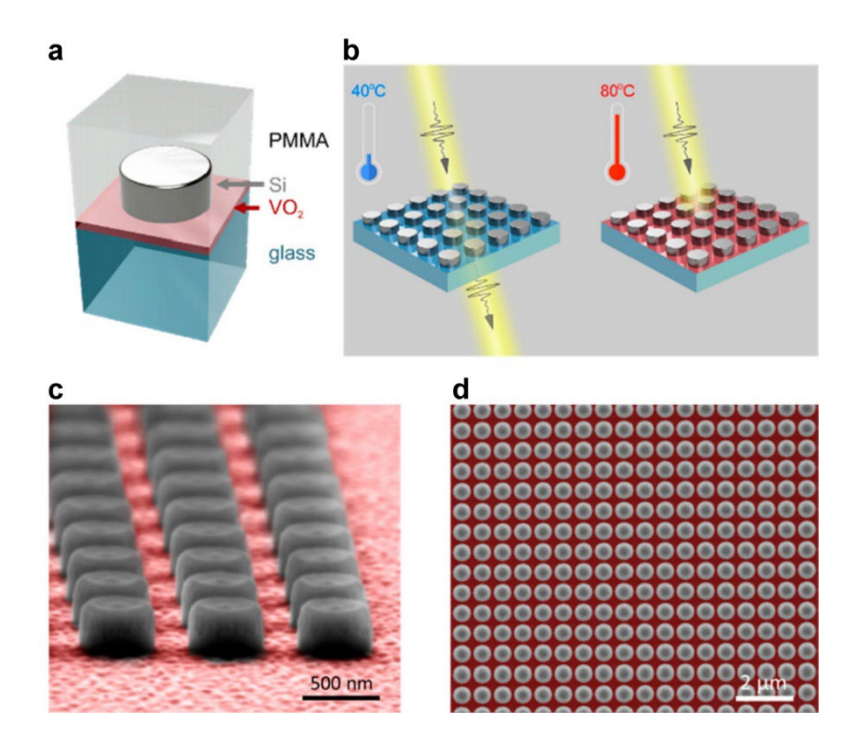


Fig. 11 Tunable Mie resonance-based tunable dielectric metasurfaces. (a) shows the unit structure. A 25 nm thick layer of VO<sub>2</sub> thin film is deposited on a glass substrate. Si blocks with a height of 240 nm and a radius of 255 nm are surrounded by PMMA. The periodicty of the Si blocks is 700 nm. (b) demonstrates the transmission reduces significantly when the metasurface is heated up to 80°C, which works as a blocking device. (c) and (d) show the microscopic views of the meta-atom produced in experiments. The PMMA coating is not present when taking these pictures. The figures (a)~ (d) are copied from [138].

In Fig. 12, another programmable metasurface using VO<sub>2</sub>-based structures, mainly applied in terahertz communication, is presented [139]. Similar to the design revealed in Fig. 5, by leveraging the reversible phase transition VO<sub>2</sub>, this metasurface employs a more complicated unit structure to amplify the contrast of this device before and after the phase transition. By coupling VO<sub>2</sub> with other metal materials, the composite unit exhibits significantly different resonance frequencies in its low-temperature and high-temperature working states, corresponding to 0 and 1 in optical coding. Although this work only demonstrates 1-bit and 2-bit coding metasurfaces that operate at switchable frequencies (for 1-bit, the work band is from 1 THz to 1.4 THz. For 2-bit, the band is extended to 1~1.5 THz), since multi-frequency or broadband coding is based on the same design rules, the solution can be generalised to other frequencies or functional materials. This work also exhibits another advantageous feature of VO<sub>2</sub> in the design of nanophotonic devices, which is the ultrafast switching response at the femtosecond level. This feature makes the design of switchable devices based on VO<sub>2</sub> phase

transition potentially applicable to optical computing [28, 140].

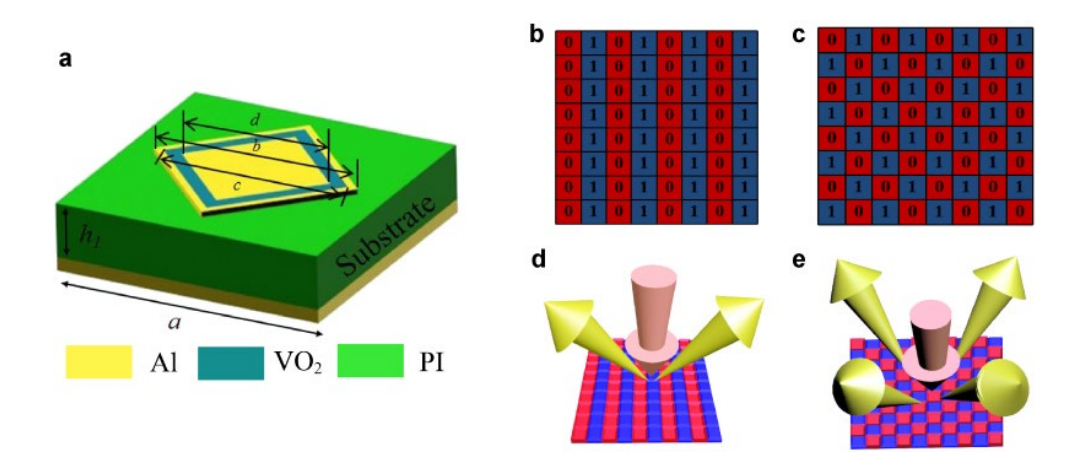


Fig. 12 Terahertz-band coding enabled by VO<sub>2</sub>-based switchable metasurfaces.

(a) The schematic diagram of metasurface units. The side length a is 110 µm, and height  $h_I$  is 20 µm. (b) and (c) are schematic diagrams of the coding sequences. Basic sequences 01010101/01010101 and 01010101/10101010 are respectively implemented. (d) and (e) are the reflex diagrams to exhibit the actual input and output traces of these certain sequences. The figures (a)~ (e) are copied from [139].

In addition to the two works listed above, metasurfaces have also received widespread attention in a spectrum of other disciplines, such as high-resolution imaging, signal sensing, telecommunications, quantum optics and artificial intelligence [6]. This report will put the focus on the applications of characteristics of metasurfaces in the design of optics, especially metalenses. It will provide a theoretical perspective for my work about the metalens design.

### 2.4.2. Introduction to metalenses and their categorisation

A metalens is a diffractive optical device designed based on two-dimensional structures at the subwavelength scale, the essential imaging mechanism of which is the modulation of the phase. It can be considered as a new form of diffractive optics after metasurface technology matures. Compared with traditional optical systems, metalens have the following important features [39, 40, 48]: (i) Nanostructure array. The nanoscale arrays composed of dielectric materials like Si provide high flexibility of design. (ii) Subwavelength resolution. Metalenses work at the nanoscale, allowing for the manipulation of light beyond the diffraction limit of conventional optics. (iii) Aberration correction even when operating at high numerical aperture. (iv) Tunable properties, allowing for dynamic adjustments in the focus, wavelength sensitivity, or other optical characteristics.

Unlike traditional glass lenses, which control the light path by changing their 3D geometric shape, metalenses are planar arrays of nanostructures that control the light by phase modulation. In theory, the lens thickness can be reduced to the order of wavelength (i.e., hundreds of nanometres) without changing the output wavefront. However, it is impractical in the manufacture of conventional lenses. Small device thicknesses that are at the order of subwavelength are instead achieved in metalenses, which use a fundamentally different approach to shape the output wavefront. The concept of wavefront reshaping refers to the manipulation of the spatial characteristics of light waves, typically with the goal of transforming their phase, amplitude, or both of them to achieve a desired output distribution or focus. The reshaped wavefront can be used to improve image resolution, focus light on specific locations, or create tailored beam profiles. The precise control of wavefronts is essential for overcoming diffraction limits and enhancing the performance of complex optical setups.

What brings widespread attention to metalenses in the research field is the flexibility of their tunable properties and the material selection. For singlet metalenses, a variety of methods are proven to be effective in focus tuning, such as deforming the metalens by mechanical [128], electrical [44] or thermal excitation [45]. Besides, plasmonically enhanced metalenses are proved to be effective, which leverage the interaction between light and surface plasmon polaritons (SPPs) to enhance their optical properties. These metalenses are typically made of metallic nanostructures that can manipulate light at subwavelength scales. In more functionally complex optical systems like double-layer metalenses or coherently controlled metalenses, the tuning is implemented by operating these plural elements or sources. Another way to achieve tunable properties of metalens is to change their functional materials. In this category of metalenses, the system exhibits different optical properties by using materials with tunable properties, and the variation inside these materials is implemented by changing the temperature or their resonance characteristics. The materials that have been explored include amorphous Si, Titanium dioxide (TiO2) [141], chalcogenide glass [142], polymer nanocomposites [143], liquid crystal [43], GaN [144], GeSbTe (GST) [145], GeSbSeTe (GSST) [146], graphene [147] and InSb [45]. Specific to a certain material, its crystal structure can be significantly changed (such as changing between amorphous and crystalline states or changing between different crystalline states) by applying external forces such as heating or mechanical deformation. To achieve functions like focus switching or intensity adjustment, different approaches are attempted and discussed in the research from 2016.

A significant amount of work has been conducted on metalens research, from the perspectives of working principles, design flows and performance. In this section, I list three representative works as the background information. They are basically designed based on different working

mechanisms, and through introducing these literatures, I will explain how I apply the VO<sub>2</sub> phase transition to the metalens design and which type of them fits the characteristics of VO<sub>2</sub> better.

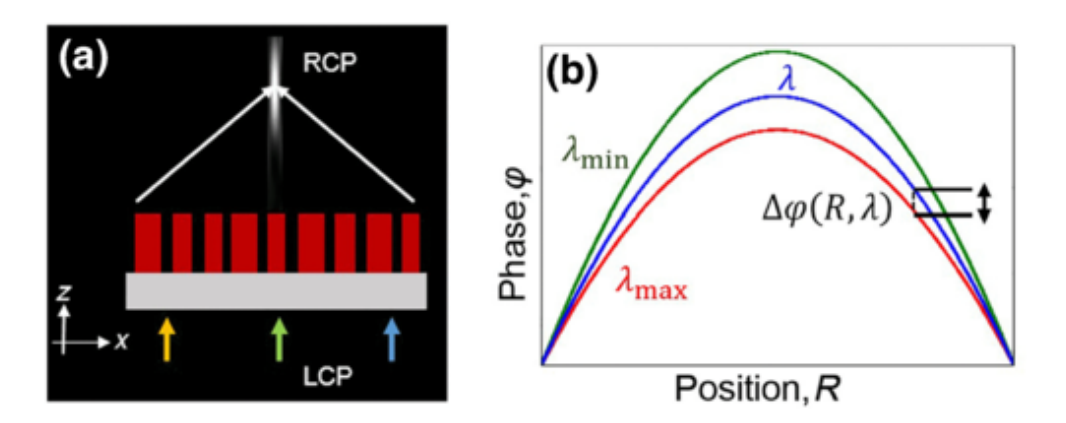


Fig. 13 Propagation phase metalens based on nanofin pair units. (a) Schematic of an achromatic metalens. The height of the nanopillars is 4  $\mu$ m, and the period of metaatoms is 1.8  $\mu$ m. A high aspect ratio is ensured to generate propagation phase. The focal length is unchanged as the incident wavelength is switched, resulting in a single spot at the designed focal point for a broadband achromatic metalens (BAML) with optimized phase compensation. (b) Phase profile for a BAML at a bandwidth of  $\Delta \lambda = \lambda_{max} - \lambda_{min}$ . The figures (a)~ (b) are copied from [148].

Fig. 13 demonstrates a novel design to implement arbitrary control of metalens dispersion over a large continuous wavelength domain in the mid-infrared band [148]. This work illustrates a propogation phase metalens. The structural basis of this design is the element composed of a pair of nanofins with different sizes. The structure and aspect ratio of the nanofin design are mainly based on the propagation phase transmission, but the whole device applies the light of different polarisation types. However, the propagation phase should not change the polarisation state of the light, which makes the design unique. Though this work combines PB phase metalens to the design to implement the precise control of wavefront (while the propagation phase is mainly used to eliminate the chromatic aberration), it explains how propagation phase is applied in the metalenses. This metalens works at a wavelength band from  $3.7 \,\mu m$  to  $4.5 \,\mu m$ , and the focusing intensity at  $4.5 \,\mu m$  is 20.7%.

From the structural point of view, the most significant feature of these nanofin-base elements is the high aspect ratio of the nanostructures. The phase distribution of light passing through these nanofins is similar to conventional optics. Inside these nanofins, light propagation has characteristics similar to propagation in waveguides. The approximately linear propagation of light through the unit elements allows the wavefront to be precisely controlled to form patterns

on the lens surface. The main advantage of metalenses designed based on the propagation phase is that they are less dependent on the resonance characteristics of single elements, so they can be applied to a wider band (the structure shown in Fig. 14 can operate in almost the entire visible light band). In addition, despite applying a phase modulation principle similar to conventional geometric optics, propagation phase metalenses still exhibit excellent performance in diffraction limit achromatic thanks to its flexibility in the design.

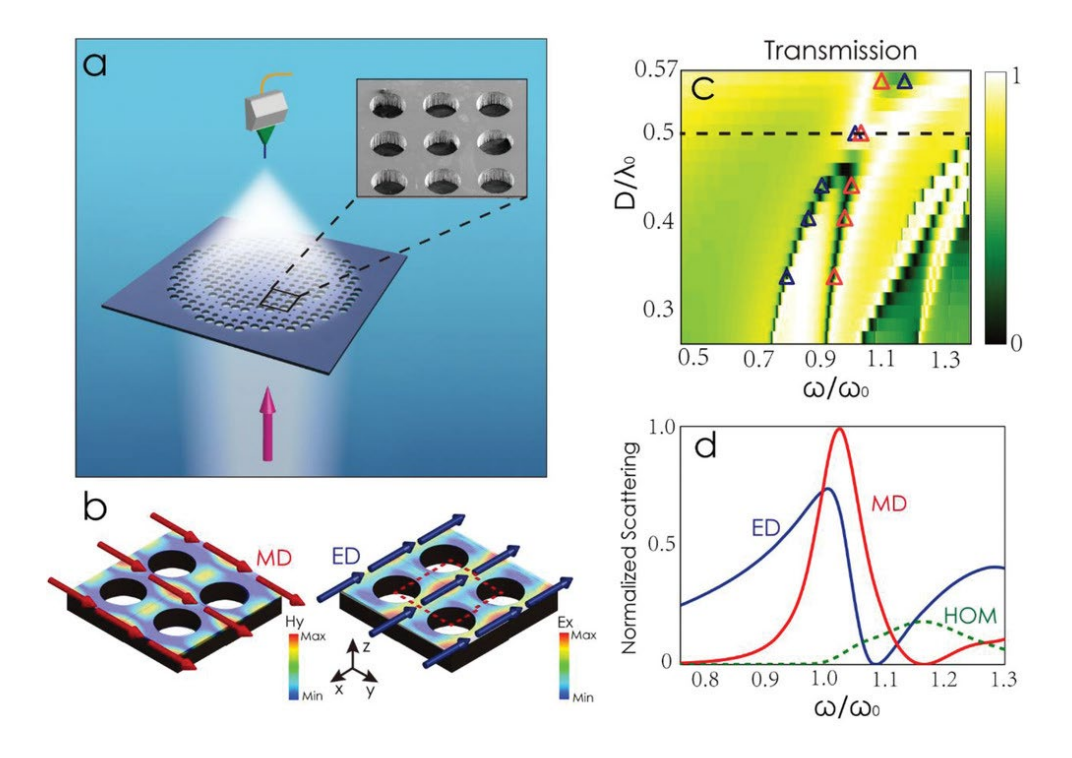


Fig. 14 Schematic and properties of Mie-resonance metalens. (a) Schematic of the metalens. The design is based on Huygens' metasurface on the ultrathin perforated dielectric membrane. A SEM image embedded shows the unit structure of this metalens. (b) The field distribution of MD (red arrow) and ED (blue arrow) on the surface of this metalens. The area marked by red dashed square is the meta-atom. (c) The transmission profile against the diameter of holes. The red and blue triangle represents the corresponding MD and ED decomposition.  $\omega_{\theta}$  and  $\lambda_{\theta}$  represent the theoretical frequency and wavelength to implement. (d) Total multipole contributions of ED, MD resonances, and sum of high order multipole (HOM). The figures (a)~ (d) are copied from [149].

Different from the propagation phase metalens, Fig. 14 shows a metalens design based on Mie scattering metasurfaces [149]. In a Mie-resonance type metalens, the lights interact with the dielectric nanostructure, then strong scattering and absorption occur at certain wavelengths (that is the work wavelength for these metalenses). The resonance features can be adjusted via the

structure dimensions, refractive index and the light path (shape of the device). Mie-resonance metalenses usually have a very high Q-factor that means the ability to concentrate the light and reduce the energy loss. The unit structure of this metalens is the holes of a specific size on a silicon substrate, using a high refractive index dielectric material substrate and low refractive index embedded elements (actually air in the holes) to achieve the function of subwavelength resonators. Compared with this new membrane design, traditional Mie-resonance metalenses grow high-refractive-index geometric structures (e.g., Si pillars or blocks) on low-refractive-index substrates (such as silica) to implement the resonance functions [150]. These two solutions to metalens design are based on similar principles, i.e., the Mie scattering as described above.

The Mie scattering occurs when waves interact with spherical particles, the size of which is comparable to the wavelength of the incident waves [151]. In subwavelength nanostructures (which metasurfaces and metalenses are formed as), strong Mie scattering is observed when the period of these repeated units approaches the wavelength of the incident light, which shows certain resonance characteristics such as transmission or reflection peak/valley at some specific wavelengths. Utilising this frequency-sensitive characteristic, it is possible to design light modulation devices dedicated to certain wavelengths to modulate the amplitude and phase of the incident light. Metalenses are one such application aimed at the precise control of wavefronts, as shown in the example in Fig. 14.

Compared with propagation phase metalenses, one major advantage of this type of metalens is the design flexibility. The resonant properties of individual elements can be amplified or hidden throughout the array (for example, defective elements have a limited impact on overall device performance when the number is reduced), allowing the design of more complex lens structures [149, 152, 153]. At the same time, Mie-resonance metalenses are often used to regulate a single-wavelength or narrower band of light, as the response of units of the same structure to different wavelengths shows significant differences. Considering that VO<sub>2</sub> samples show very large differences in their optical properties (especially refractive indices that I put my focus on), the ability to reduce the effect of single units on the entire metalens array will be a significant advantage for my design.

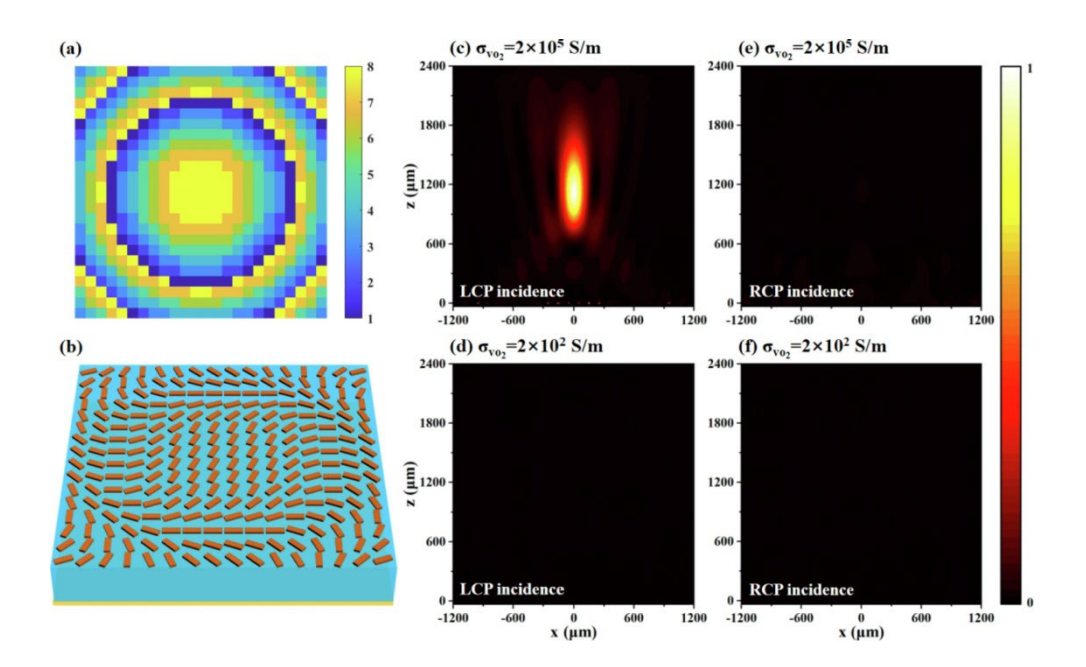


Fig. 15 Switchable Pancharatnam-Berry metalens working at the terahertz regime. (a) Phase distribution profile of the metalens. (b) Schematic of the structure. (c) and (e) show the normalized power distribution in xz-plane of LCP incident. (d) and (f) show the normalized power distribution in xz-plane of RCP incidence. Different conductivities are used in these maps.  $\sigma = 2 \times 10^5 \, S/m$  for (c) and (e).  $\sigma = 2 \times 10^2 \, S/m$  for (d) and (f). The figures (a)~ (f) are copied from [154].

Fig. 15 shows an example of Pancharatnam-Berry (PB) phase metalens [154], which is another category of metalens design. Different from the two previously described metalenses, to achieve free control of the wavefront, the way the phase difference is generated among the elements in a PB metalens is not derived from the difference in their physical dimensions. The phase response of each unit is determined by the orientation. By rotating the angle of each element in the metalens array, left-handed circularly polarized (LCP) waves and right-handed circularly polarized (RCP) waves are combined to obtain a full  $2\pi$  phase coverage, thus providing a prerequisite for precise wavefront control. My work will focus on the response to linearly polarised light, so the PB phase metalenses will not be discussed in detail.

#### 2.4.3. The general design method of metalenses

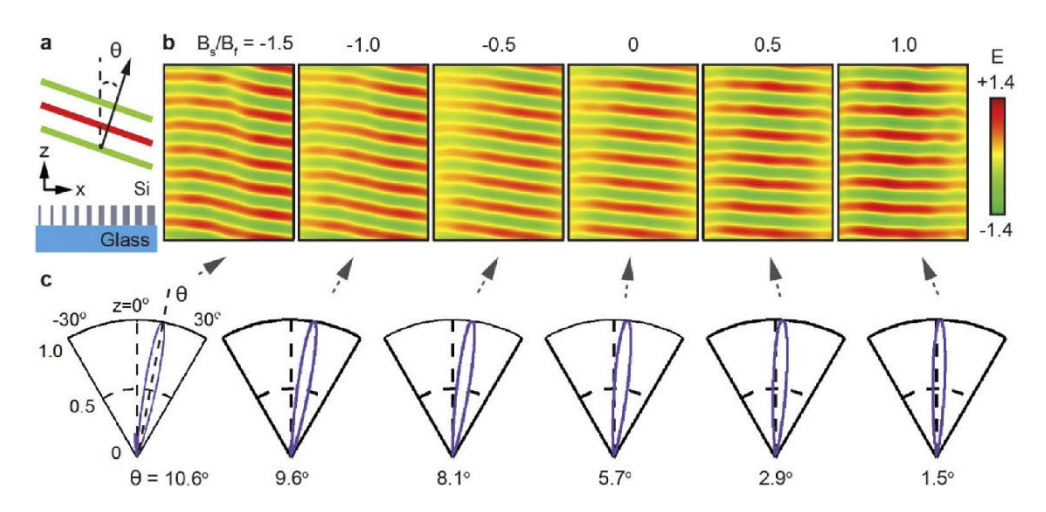


Fig. 16 Coherently controlled beam-steering implemented on a phase-gradient metasurface. (a) Cross-section view of the meta-atom and the schematic of how beam-steering is performed along the xz-plane. (b) Electric field distribution in xz-plane from 1  $\mu$ m to 5  $\mu$ m above the middle plane. Different coherent illumination conditions applied. (c) The angular distribution of output intensity which correspond to different phase gradient profiles shown in (b). The figures (a)~ (c) are copied from [155].

Before introducing the methodology of my own work, here I will outline the general process of metalens design and briefly explain the specific significance of each step, which is an essential reference for the research on metalenses.

In the concept of wavefront reshaping using metasurfaces or metalenses, phase gradient is a fundamental design target. For a unit that contributes to a certain phase difference, the step length of the phase difference produced by elements inside the meta-atom determines the resolution of the reshaped wavefront. In theory, if the phase difference between adjacent elements is too large, a step-like phase delay in the electric field distribution can be observed, which is similar to the sawtooth lens structure in the design of geometric optics [39, 128]. To this end, designing smooth phase gradients is necessary for high-precision wavefront reshaping. To present the implementation of phase gradient intuitively, Fig. 16 illustrates a metasurface design based on coherent light modulation [155]. There are 10 elements along the *x* direction. By changing their geometric dimensions, different phase output can be observed on these elements. Since the phase difference between adjacent elements is designed to be linear, it can be clearly seen from Fig. 16(b) that an approximately linear phase gradient is output.

The basic structure of this design is that Si pillars of different sizes are grown on a glass

substrate. Coherent lights are used to change the illumination conditions, which make these silicon pillars work at electrical field and magnetic field antinodes (corresponding to the positions where the resonances are observed), thereby outputting different phase differences. As the nanopillar array shows similar geometric features to the deflection gratings, the deflection angle is relative to the wavelength of incident lights. There is the following relationship between the deflection angle  $\theta$ , wavelength  $\lambda_0$ , phase difference and unit spacing:

$$\sin\theta = \frac{\lambda_0}{2\pi} \frac{d\varphi}{dx} \tag{11}$$

where  $d\varphi$  represents the phase difference between any two elements and dx is the distance between them. According to Eq. (1), given any specific deflection angle, the phase gradient profile can be calculated, then corresponding Si pillars can be selected to form the element library (a database that includes dimensional parameters of all units that are obtained by parametric sweep). For a metalens that is usually a circular 2D array, the arrangement of elements follows different formulas (such as Eq. (12) given below), and the complexity of the phase profile is relatively higher, involving two directions on the plane. With phase gradient as the basis for the arrangement of units in metalens, below I will outline a common metalens design process.

Fig. 17 shows the meta-atom design of coherently controlled tunable metalens [156]. Its design can basically be regarded as an extension of the work shown in Fig. 16. The focusing function of this metalens is achieved by the modulation of the wavefront by Si pillars arranged in a specific order on the glass substrate. The phase contrast of the Si pillars working in the Eantinode mode and B-antinode mode is the foundation of the focus-switching function. The basic element of this metalens is a Si nanopillar. The height of all Si pillars is set to 500 nm. The semi-axis length  $R_x$  and  $R_y$  are variables. By sweeping these two parameters, the element library that meta-atoms are chosen from can be established, as shown in Fig. 17(b) and Fig. 17(c). The elements in the library will be used to satisfy the phase distribution to implement target metalens parameters. By comparing Fig. 16 and Fig. 17, the phase profile to implement in the metalens design involves two directions (xy-plane), which is more complicated than 2D linear metasurfaces. For the phase profile of metalenses, Since the arrangement of the units on the metalens involves two dimensions (x-position and y-position), a formula to describe the projection of a spherical wavefront on a planar surface for calculating the phase difference required to be output by each element can be obtained by the Pythagorean theorem and Eq. (11), which is expressed as:

$$\varphi(d,\lambda,fl) = \frac{2\pi}{\lambda} (\sqrt{d^2 + fl^2} - fl)$$
 (12)

Here, d is the distance between each element and the centre of metalens,  $\lambda$  is the wavelength of the incident light, and fl is the focal length designed for the metalens. By determining the target focal length and design size (diameter) of the metalens, for each element on the lens array, the theoretical output phase can be calculated using the distance relative to the centre point, thereby constructing the ideal phase profile for comparison. By matching the elements in the library with the theoretical phase profile, an approximate output wavefront to achieve focusing can be obtained.

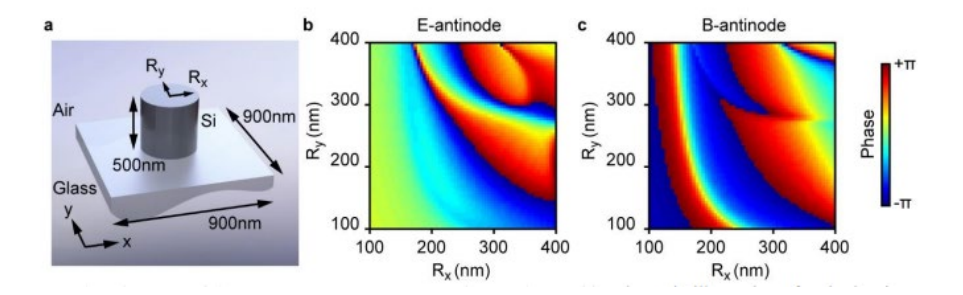


Fig. 17 Unit nanostructure and the phase library produced through parametric sweep on it. (a) Schematic of the meta-atom. A Si pillar with a height of 500 nm is grown on the glass substrate. The side length  $R_x$  and  $R_y$  vary from 100 nm to 400 nm with a step of 5 nm during the parametric sweep. The period of the element is 900 nm. Colourmaps in (b) and (c) show the phase library produced under E-antinode and B-antinode illumination conditions respectively. Two axies correspond to the variables  $R_x$  and  $R_y$ . The phase value is wrapped into a range from  $-\pi$  to  $\pi$ . The figures (a)~ (c) are copied from [156].

With Eq. (12), calculating the ideal phase distribution map based on the functional parameters of the metalens only requires simple analytical calculations. The real challenge for metalens design is how to establish a library providing a sufficient number of elements with high phase accuracy. The very basic approach to building an element library is to do parametric sweep on the dimensions of meta-atoms, which can be implemented by numerical simulation or analytical calculation. By determining constants like the period of meta-atoms and height of them, the rest variables such as the horizontal dimensions can be swept within a range, then the phase and amplitude output can be measured and collected as an element in the library. With all units selected and arranged in the metalens array, the performance of the entire metalens can be predicted.

For a metalens with a single focus (i.e., only has one working state), achieving the target phase distribution only requires arranging elements of specific dimensions, which strongly depends on the size of the element library. For a tuneable metalens, for example, the binary tuneable metalens, the design should follow more guidelines, which can be summarized as these two points. (i) A full  $2\pi$  phase coverage. For a spherical wavefront, the scope of the phase profile curve is not constant. When the phase changes rapidly (shown by a very large slope of the phase profile), too few elements for matching contribute to larger errors. Generally, libraries that cover at least  $2\pi$  phase have higher tolerance for design faults. (ii) Relatively high contrast. From an application perspective, it is difficult to prove that a significantly limited tuning range is credible, and systematic errors may cause experimental results to be completely opposite to those predicted by simulations. For the element library, a large contrast between different working states provides higher flexibility of design.

Specific to each certain metalens design, due to the differences in functional materials, illumination settings, and methods of achieving focus switching, the rules that should be followed when building an element library based on theoretical phase profile will also be different. The approach I use to establish the element library will be detailed in the methodology chapter.

# 3. Methodology

### 3.1. Fabrication techniques of VO<sub>2</sub> films

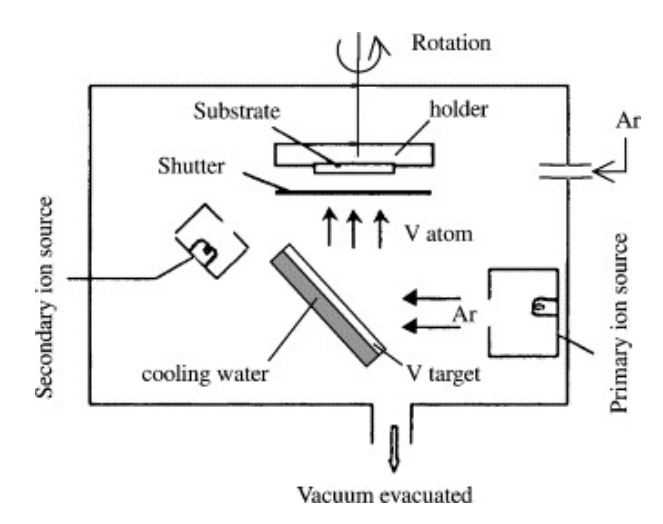


**Fig. 18 Schematic diagram of an ion sputtering system.** In the vacuum chamber, ion source (Ar) generates a high-energy ion beam. The ions are accelerated towards target material (V). When they collide with the target material, the V atoms are ejected or sputtered from the surface and form a thin film on the substrate by travelling through the vacuum condenses. The figure is copied from [157].

Early research related to the fabrication of VO<sub>2</sub> thin films dates to around two decades ago when ion beam sputtering was used to deposit metal vanadium thin films on Si or SiO<sub>2</sub> substrates [158, 159]. High-energy ions collide with the atoms in the target (such as the vanadium target shown in Fig. 18), making them ejected or sputtered off the surface, then travel onto the substrate to produce the vanadium film. Oxidation is then carried out after the deposition to convert the vanadium thin film to a VO<sub>2</sub> thin film [157]. Fig. 18 is a schematic of an ion beam sputtering system. The vanadium target is placed near the bottom of the system, while the substrate is mounted on a rotation holder at the top of the chamber. A tube at the side of the chamber feeds Argon gas into the chamber. The primary and secondary ion sources are placed on opposite sides of the chamber. The main advantage of this deposition method lies in the relatively fast growth rate of films, enabling the fabrication of larger geometric shapes such as blocks and pillars. However, ion beam sputtering has some notable drawbacks. It is easy to cause metal contamination in the chambers of the experimental system [160]. Besides, in designs that involve coating process that grows vanadium or VO<sub>2</sub> on the side walls, growth with higher isotropy is required. Sputtering is not such a flexible method to grow films along different directions.

Ion beam sputtering is only one of many methods to fabricate VO<sub>2</sub> thin films. Currently, VO<sub>2</sub> thin films can be fabricated using a range of different methods including magnetron sputtering, pulsed laser deposition (both physical vapour deposition methods) [161, 162], chemical vapour deposition [163], sol-gel [164] and epitaxy.

In comparison to these methods, recent developments in ALD (Atomic Layer Deposition) have made it a powerful method that is especially attractive for research on nanoelectronics and nanophotonics [93, 165, 166]. The fundamental principles of ALD can be summarised by breaking down the entire growth process into numerous independent cycles. In each cycle, the precursor materials used to synthesize the target product are injected into the chamber in a specific sequence, achieving the growth with a minimum precision of one single molecular layer [167, 168]. For a product that requires two precursors, a purging step is necessary between any two impulses to inject precursors, which is the basis of control of atomic layers and conformal deposition. The details will be introduced below.

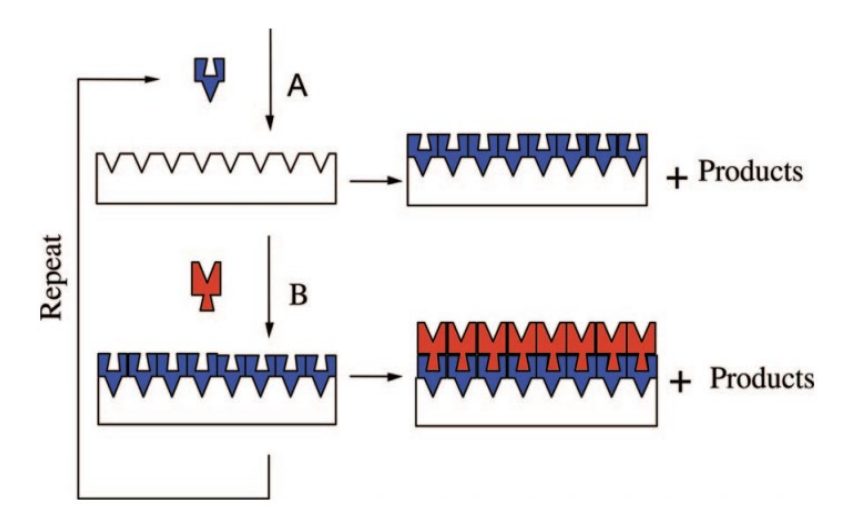


Fig. 19 Schematic representation of ALD using self-limiting surface chemistry and an AB binary reaction sequence. In each cycle, precursor A is firstly pulsed into the chamber and attached to the substrate. Before the injection of precursor B, the chamber should be purged to remove the rest precursor A. After pulsing precursor B, same purging process is required. Then repeat this cycle to deposit the compound of A and B one layer per cycle. The figure is copied from [169].

Fig. 19 reveals the basic procedures in a cycle of ALD. ALD is a sequential and cyclic process (these are also two most important features of ALD) involving a series of self-limiting surface reactions, and the core mechanism is similar to the replacement reaction in chemistry. The minimum periodic time interval of ALD is a cycle. One deposition process consists of hundreds

or thousands of repeating cycles. In a cycle, there are several steps that we could describe to explain what happens during the ALD process.

Combining with Fig. 19, the steps include: (a) Substrate preparation: The substrate is cleaned to remove contaminants and provide a suitable surface for chemical reactions. This ensures optimal adhesion and uniformity of the deposited film. (b) Precursor pulse (reactant A introduced): A gaseous precursor is introduced into the reaction chamber, where it adsorbs onto the substrate surface. The reaction is self-limiting, meaning only a single monolayer or submonolayer of the precursor molecules binds to the available reactive sites on the surface. Any excess precursor remains in the vapour phase. (c) The first purge: Inert gas, such as nitrogen or argon, is flowed through the chamber to remove any unreacted precursor and by-products from the last step. This ensures the subsequent reaction occurs only with the adsorbed layer, avoiding gas-phase reactions. (d) Co-reactant pulse (reactant B introduced): A second reactant, often referred to as the co-reactant (e.g., water vapour, oxygen, or hydrogen plasma), is introduced into the chamber. This reactant reacts with the adsorbed precursor layer to form the desired thin film. (e) Second purge: Similar to first purge, inert gas is introduced to remove any by-products and residual co-reactant gases, ensuring that the surface is ready for the next cycle.

Sequential and self-limiting surface reactions are the main characteristics and advantages that ALD brings. For inorganic substances with simple structures such as metal oxides, the essence of binary reaction can be regarded as the combination and replacement of different components in the precursor mixture which occur on the deposition surface [170]. Binary reaction sequences are viewed as the basis of the principles of ALD, where reactions of two surfaces occur and deposit binary compound films between them. Limited by the finite number of surface sites, each round of the reactions can only deposit a certain number of species. Then if all rounds of reactions follow the self-limiting rule, the reaction A and B can proceed sequentially to deposit an optimal thin film with precise atomic level control [171].

Fig. 19 introduces a very general flow of a ALD cycle. Specific to VO<sub>2</sub>, the reactant A can be chosen from a variety of precursors that contain vanadium. In the Table. 2 below, several commonly used precursors for the growth of vanadium oxide (V<sub>x</sub>O<sub>y</sub>, the value *x* and *y* are determined by the process design) are listed according to the valence state of vanadium in the precursors. Vanadyl acetylacetonate (VO(acac)<sub>2</sub>) and vanadyl tetramethyl heptadionate (VO(tmhd)<sub>2</sub>) are two typical organic precursors for vanadium growth. However, their usability in the ALD process is limited by many conditions. For example, VO(acac)<sub>2</sub> turns into vapour phase at around 170 °C and thermally decomposes at around 180 °C, which makes the control of experimental temperature very difficult. For VO(tmhd)<sub>2</sub>, the low reactivity of it makes its

reaction incomplete, thus increasing the possibility of excessive oxidation by ozone to produce V<sub>2</sub>O<sub>5</sub>. Different from them, Vanadium oxy-tri-isopropoxide (VTOP) is widely used as the precursor to produce V<sub>2</sub>O<sub>5</sub>. Since the vanadium ions exist in the pentavalent form, we usually do not use it as the first choice for ALD process of VO<sub>2</sub>.

Table. 2 Comparison between commonly used precursors for the ALD process of vanadium oxide [166]

Precursor		Vapour pressure	Reactivity		Thermolysis	
			H <sub>2</sub> O	$O_3$	O <sub>2</sub> -Plasma	threshold
$V^{3+}$	V(iPr-Me AMD) <sub>3</sub>	6.6Pa @70°C	×	$\sqrt{}$	-	-
$V^{4+}$	V(N Me <sub>2</sub> ) <sub>4</sub> (TDMAV)	133Pa @64°C	$\sqrt{}$	$\sqrt{}$	$\sqrt{}$	120 °C
	V(N Et Me) <sub>4</sub> (TEMAV)	13Pa @25°C	$\sqrt{}$	$\sqrt{}$	$\checkmark$	> 175 °C
		24Pa @70°C				
		57Pa @82°C				
	VO(acac) <sub>2</sub>	0.21Pa @96°C	×	$\sqrt{}$	-	180 °C
	VO(tmhd) <sub>2</sub>	0.24Pa @96°C	×	×	$\checkmark$	160 °C
$V^{5+}$	VO(O <sup>i</sup> Pr) <sub>3</sub> (VTOP)	6Pa @25°C	$\sqrt{}$	$\sqrt{}$	$\checkmark$	100 °C
		39Pa @45°C				
		268Pa @82°C				

Among all other precursors, it is particularly noteworthy that tetrakis ethylmethyl amino vanadium (TEMAV) and tetrakis dimethylaminovanadium (TDMAV) are widely used in the ALD for growth of VO<sub>2</sub> (annealing process is required to determine the ratio of vanadium and oxygen in the oxide). TEMAV and TDMAV precursors are implemented with H<sub>2</sub>O, O<sub>3</sub> and O<sub>2</sub>-plasma. When using H<sub>2</sub>O or O<sub>3</sub> as the reactant, vanadium with +4 oxidation state is deposited while O<sub>2</sub>-plasma contributes to +5 oxidation state. The decomposition of TEMAV can be observed at around 175 °C, and the self-limiting reaction of TEMAV is commonly observed at 150 °C, which means there is a temperature window of 25 °C that allows a wider temperature control tolerance. Similar to TEMAV, TDMAV also provides large flexibility in the settings of conditions for ALD. The reaction of TDMAV precursor usually occurs between 150 °C to 200 °C, then thermal decomposition is observed. Compared with TEMAV, TDMAV has a higher decomposition temperature, which makes it easy to use H<sub>2</sub>O as the oxidation reactant at low

temperature. However, it also brings some drawbacks, such as the longer purging time, which affects the efficiency of growth process. Besides the difference in these precursors, other details including the temperature and reaction time I set for my ALD process will be introduced in the results section 4.1.1. There won't be more parametric information given in this section.

Due to its low-temperature, layer-by-layer and self-terminating deposition mechanism, ALD provides a high level of control over film thickness and uniformity, compatibility with a wide range of substrates, and the capability of conformal film deposition [76, 172, 173]. This mechanism provides easy control over the progression and the termination of deposition. The reaction can be stopped by simply changing the supply of reactants. Practically, similar to the traditional chemical vapour deposition (CVD) method, the deposition rate can vary across a large substrate due to several factors (e.g., a variation in precursor gas fluxes [174]). At the same time, it's possible to precisely control the precursor quantity that a cycle pulse could bring by changing the pressure, temperature or other parameters. Another obvious advantage of ALD process in the growth of vanadium oxide is the isotropy of growth brought by its high selflimiting feature. For certain structures that have a high aspect ratio, the growth on sidewalls or in the gaps is a problem, especially for those efficient deposition techniques such as sputtering. Though the growth rate of ALD is also affected by the relative dimensions of different parts of a structure, it contributes to a much better uniformity in terms of spatial distribution. In summary, ALD remains an optimal method for the deposition of VO<sub>2</sub> thin films (especially those ultrathin films such as a 40 nm sample). Due to these features, during my PhD project, ALD is used to deposit VO<sub>2</sub> thin films.

### 3.2. Transfer matrix methods for analytical calculations

When it comes to predicting the performance of optical devices, analytical calculations and numerical simulations are commonly used methods. When extracting optical parameters using theoretical models (such as the Bruggeman's model and Looyenga's model), the most common approach is to input optical parameters such as refractive index and dielectric constant and output the physical quantities we need for analysis and comparison through a series of formulas, such as transmission or absorption through a multilayer film structure. Among them, transfer matrix method is an effective tool to calculate the output of complicated systems composed of multiple films.

Specific to my work on the vertical growth models used to predict the phase transition behaviours of VO<sub>2</sub> films, there are certain parameters involved when using the transfer matrix method. The input variable of the transfer matrix is the refractive index (instead of the dielectric

constant) of materials in each layer at a specific wavelength, and the output is the reflection of the entire system (it can also be transmission, but it depends on the setup design, which determines how difficult the measurement process is).

The transfer matrix method is used in my work to implement the modelling of VO<sub>2</sub> phase transition at the analytical level through MATLAB, which enables me to establish a numerical model of different theoretical models to describe the phase transition of VO<sub>2</sub> and compare them. As introduced above, the transfer matrix method [175, 176] is a mathematical tool that is commonly used to calculate the optical properties of coherent thin-film multi-layer structures. Its main principle lies in the repeated use and iteration of the Fresnel equation [177] to solve the problem of repeated transmission and reflection of multiple component vectors of light in complex optical structures. After years of experimental demonstration and development, this method has high reliability in a two-dimensional multi-layer structure [176, 178]. The difficulty of applying the transfer matrix method mainly points to the realization and derivation at the software level.

According to Maxwell's equations, continuity conditions exist during the process when electric fields cross the boundaries between different media [179]. With the initial condition given, by calculating the product of matrices of all layers and deriving the reflection and transmission coefficients from it, the output field can be derived. For the medium at layer *I*, the transfer matrix can be defined by:

$$M_{i} = \begin{bmatrix} \cos(p_{i}) & -\frac{i}{c_{i}}\sin(p_{i}) \\ -i\sin(p_{i}) & \cos(p_{i}) \end{bmatrix}$$

$$(13)$$

where  $p_i$  is the wave vector of the medium, and  $c_i$  is the wave impedance that is relative to the refractive index. The transfer matrix is strongly dependent to the incident angle and the correlative trigonometric variables. As each layer in the system has a transfer matrix as described in Eq. (1), the equivalent transfer matrix can be expressed as:

$$M = \prod_{i=1} M_i \tag{14}$$

The reflection coefficient of the whole system can be directly derived from the transfer matrix.

To verify the results calculated by MATLAB based on the transfer matrix are correct, I have performed the same calculation design using the finite element simulation tool COMSOL. According to this design of the unique vertical growth models (will be introduced as a part of

my results), approximately 5-6 points on a reflection curve are selected for verification. The main rationale for this method is that the simulation of periodic structures assumes each layer is infinitely large and uniform along the horizontal plane, so transfer matrix analysis can be directly compared with simulation results. The results calculated by the transfer matrix and COMSOL match well.

The settings of geometric structure and physical boundaries in COMSOL and the verification results are detailed in Appendix A. In summary, with same physical parameters given (the thickness of each film layer and the refractive index of each material), COMSOL generates almost same reflection output as the MATLAB calculation via the transfer matrix functions, which proves that the MATLAB script can be used to estimate the reflection output of the multilayer films.

## 3.3. Characterisation enabled by spectroscopic ellipsometry

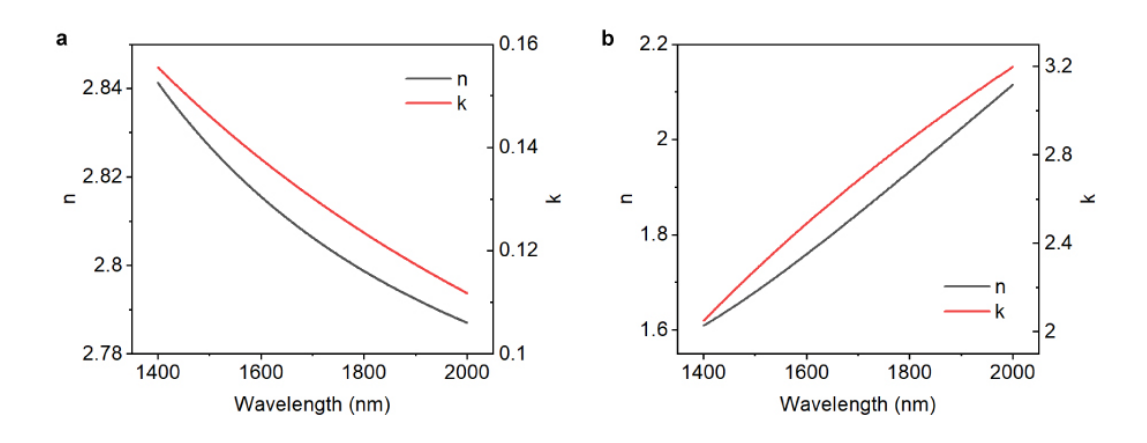


Fig. 20 Ellipsometry fitting results of n and k of  $VO_2$  at (a) room temperature (25°C) and (b) high temperature (110°C). In both states, n and k show monotonic change as the wavelength varies from 1.4  $\mu$ m to 2  $\mu$ m.

My work on phase transition models involves the comparison between different analytical models, and this comparison requires knowing the refractive index of  $VO_2$  at a high accuracy. This is achieved by conducting ellipsometry measurements on  $VO_2$  thin films. The thin films used here were fabricated by Dr Kai Sun, and the ellipsometry measurements were conducted by our collaborators at the University of Nottingham [180, 181] (the original data measured from 1.4  $\mu$ m to 2  $\mu$ m can't be measured again as the  $VO_2$  samples usually die after several months or one year without special storage techniques. However, the  $VO_2$  samples can be reproduced with same fabrication process when there is a difference in the properties.). I analysed the raw data provided by our collaborators and extracted the refractive indices. The

refractive indices are shown in Fig. 20 above. From 1.4  $\mu$ m to 2  $\mu$ m, the real part and imaginary part of the complex refractive index are measured at room temperature (~25 °C) and high temperature (~110 °C). At room temperature, both n (phase velocity) and k (extinction coefficient) decrease as the wavelength increases, while it is totally opposite at high temperature.

Here I would like to introduce the ellipsometry in detail. Ellipsometry is a non-destructive optical technique used to characterize thin films and their optical properties. It is based on the measurement of changes in the polarisation state of light reflected from a sample surface, then the changes are recorded as certain optical parameters for further analysis. Ellipsometry is particularly valuable for determining parameters such as film thickness, refractive index, and extinction coefficient of thin films [55, 66, 72, 113]. In this work, ellipsometry is mainly used to measure the refractive indices of VO<sub>2</sub> across the broadband, and the thicknesses of each layer of the film structures.

In ellipsometry, polarised light at a certain wavelength illuminates a sample at a specific angle of incidence. The reflected light undergoes changes in polarisation, and these changes are measured by an ellipsometer. The ellipsometer provides information about the ratio of the amplitude of the reflected p-polarized light to the s-polarised light, known as the ellipsometry parameters ( $\Psi$  and  $\Delta$ ). These two parameters are also regarded as the raw data of ellipsometry as many other physical parameters can be extracted from them via certain models and formulas. By analysing these ellipsometry parameters, I can extract information about the optical properties and thickness of thin films on the sample surface.

Spectroscopic ellipsometry has some advantages such as the non-contact and non-destructive characteristics. In addition, it is less sensitive to fluctuations in the power of the light source and ambient light. Nevertheless, it also has some flaws. The first is that it requires a high level of flatness for the sample surface. The second is that it requires modelling to extract the refractive index.

As the extraction of the refractive index from the raw experimental data requires modelling, it is crucial that correct physical models are used here. For the insulating phase of VO<sub>2</sub>, the Tauc-Lorentz model [182] and Gaussian model [183] are applied to extract n and k values. For the metallic phase, the Drude model [184] is used instead of the Tauc-Lorentz model. Tauc-Lorentz model combines the Tauc model that is used to calculate the adsorption coefficient near the bandgap of amorphous semiconductors, and the Lorentz oscillator model that describes the dispersive refractive index of the materials. As the VO<sub>2</sub> doesn't show the features of semiconductors anymore at its metallic phase, Tauc-Lorentz model doesn't apply to the high-temperature situation. Drude model is designed to describe the electrical and thermal

conductivity of metals by considering the behaviour of free electrons, which is applicable to the calculation of refractive index of VO<sub>2</sub> at metallic phase.

The wavelength varies from 1.4  $\mu$ m to 2  $\mu$ m. Within this range, the refractive index can be considered as continuously changing. The extraction results are shown in Fig. 20. To align different theoretical models, these n and k values are also used in the simulation of EMT and vertical growth models. According to the design of this work, the interval of 1.4  $\mu$ m  $\sim$  2  $\mu$ m is sufficient for data comparison and analysis, so the following sections will use the values of n and k within this range.

# 3.4. Parametric sweep on multiple dimensional variables

This section is mainly relative to my work on the metalens design. A key to the metalens design is finding a basic element structure that can provide the full  $2\pi$  phase coverage through geometric tuning. Just as explained in the background, a full  $2\pi$  phase coverage allows more precise control of the wavefront output by the metalens, and it also means more tolerance when some of the units in the array do not match the phase profile well. According to Eq. (11) revealed in section 2.4.3, the phase difference is dependent on the incident angle and traveling distance inside a medium. For a complex three-dimensional structure (e.g. cylindrical elements including the air in the gaps), it's extremely difficult to analytically estimate the specific light path inside the structure. As an alternative, numerical simulation tools like COMSOL Multiphysics and Lumerical are used to complete the calculation. In the numerical simulation, the calculation process is similar to the 'black box' design. By setting all relative parameters as input, the output will be given after calculating. In the design of units of metalenses, the dimensional parameters directly determine the phase output (this can also be extended from Eq. (11).). To determine the structure of each unit in the metalens array, a tool to improve the efficiency is required.

Before performing a parametric sweep, it is essential to determine the model of a single metaatom to be used for simulation. My design of the unit is inspired by the Si pillar structure shown in Fig. 17, which is proposed by [156]. The materials used to build the unit is determined to be Si-VO<sub>2</sub>-Si. VO<sub>2</sub> works as the functional material to enable the tunability of the metalens, while Si contributes to the full  $2\pi$  phase coverage benefiting from its high n characteristics (to some extents higher n value means stronger refractivity, which leaves more obvious effect on the phase) [155, 156]. The next step is to determine the period of the repeating unit, and then the height, width and depth (xyz dimensions) of the nanopillars. Parametric sweep is an effective method to filter parameters or parameter sets that satisfy specific regulations. In experiments or simulations of controlled variables, monitoring multiple variables simultaneously can greatly increase the amount of computation. For example, a sweep on two dimensional parameters of the nanopillars with 50 numbers for each parameter will generate a matrix that has 2500 sets of results. Here I design a simplified workflow of the parametric sweep: (1) Starting with pure Si pillars. Initial parameters are set as referred from [156]. The period is set to 900 nm, and the height of Si is 500 nm. To improve the efficiency, two side lengths of the pillar are set to be same, which will not affect the phase coverage but only the accuracy. (2) By adjusting the height, the lowest height to contribute to  $2\pi$  phase coverage is found to be 280 nm. Then VO<sub>2</sub> layer is added beneath the Si with same side lengths. (3) Do the parametric sweep on the side length again and adjust the height of VO<sub>2</sub> layer, which produces a good contrast between the insulating and metallic phases but do not affect the phase coverage. (4) Adjust the period (as well as the gap) to do optimisation on the phase coverage. (5) With the height of each layer, the period and the range of side length determined, the length of two sides are set as the variables for the final parametric sweep to build the element library.

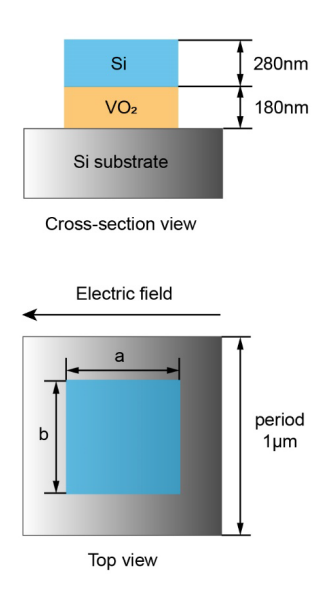


Fig. 21 Schematic of the basic unit of the metalens. The planar dimensions of the meta-atom is 1  $\mu$ m by 1  $\mu$ m. It contains a nanopillar that has a Si segment on top of a VO<sub>2</sub> segment. The thickness of the Si segment and the VO<sub>2</sub> segment is 280 nm and 180 nm, respectively. The planar dimensions a and b of the pillar serve as tunable parameters. They vary from 100 nm to 800 nm in the parametic sweep. The whole metalens is a reflective metalens. In the simulation, a plane wave with a wavelength of 1550 nm illuminates the meta-atom from the top.

Fig. 21 above shows the structure determined by the parametric sweep process after step (4). This unit structure is designed for reflective metalenses. The basic functional unit is a double-

layer structure composed of Si and VO<sub>2</sub>, which are grown on a Si substrate. The period of the element is 1 µm (for diffractive optics, the period should be smaller than the working wavelengths, but large enough to allow larger tunability). The side lengths of Si and VO<sub>2</sub> layers stay the same, which vary from 100 nm to 800 nm when being swept to establish the element library. The thickness of VO<sub>2</sub> and Si are 180 nm and 280 nm respectively, which reduces the effect of the propagation phase when analysing this design. Here I want to highlight that the metalens I design works based on Mie-resonance, which allows larger tolerance for defective elements. With such a flexible mechanism, it is easier to satisfy the phase coverage required by the metalens design. Besides, considering that I focus on the single wavelength 1550 nm for near-infrared communications, a Mie-resonance metalens will work well [149, 152, 153].

It is worth noting that the metalens is designed to function in the reflection mode (i.e., it generates a focus in the reflection). This is different from many metalenses, which work in the transmission mode (i.e., they generate a focus in the transmission). Transmissive metalenses arguably have a wider application scope than their reflective counterparts. Nevertheless, a reflective design is chosen here, because it is easier to obtain the full  $2\pi$  phase coverage. This observation is derived from the equation of phase propagation:

$$\varphi = m \frac{2\pi \cdot n}{\lambda} \cdot H \tag{15}$$

where n is the refractive index of the medium,  $\lambda$  is the vacuum wavelength of the incident light, and H is the thickness of the structure. The factor m is the number of trips that light passes through the structure. It takes the value of 1 for a transmissive device and the value of 2 for a reflective device. It is obvious that, for fixed values of n and H, if the planar dimensions are allowed to vary in a limited range, it is easier for  $\varphi$  to achieve the full  $2\pi$  phase coverage for m=2 (i.e., in reflection) than for m=1 (i.e., in transmission).

Parametric sweep is completed by finite-difference time-domain (FDTD) calculation enabled by Lumerical. By entering the sweeping range of side length a and b from 100 nm to 800 nm with a step of 5 nm, element library can be generated as the form of colourmap or dataset. The data of side lengths are stored corresponding to the output phase and amplitude, which means they are ready for being selected to build the metalens array. The specific parameters and other involved details will be revealed in results section 4.2.1.

### 4. Results and discussion

# 4.1. Vertical growth models

### 4.1.1. Vertical growth models

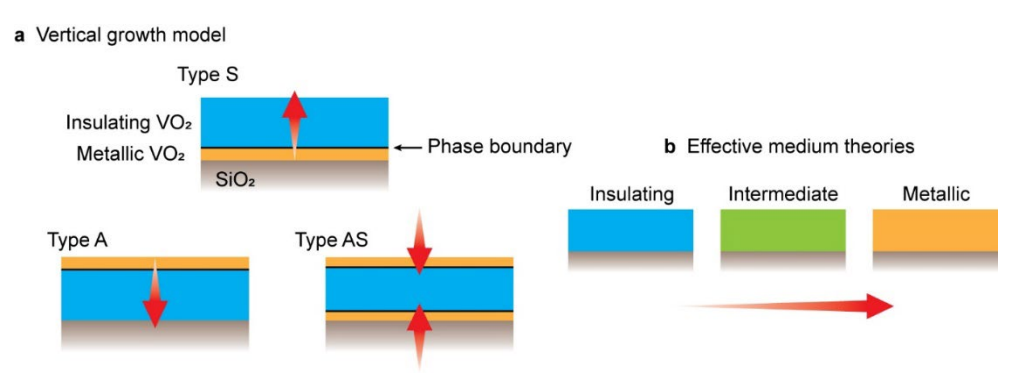


Fig. 22 Different analytical interpretations of VO<sub>2</sub> phase transition, illustrated here using an example configuration that contains a VO<sub>2</sub> thin film on top of a SiO<sub>2</sub> substrate. (a) In the vertical growth model (VGM), heating-induced transition is viewed as a layer-by-layer conversion of the low-temperature, insulating phase (blue) into the high-temperature, metallic phase (orange). This conversion initializes at the surface(s), resulting in threes variants: Type S, Type A, and Type AS. The red arrows indicate the propagation directions of metal-insulator phase boundaries. (b) In the effective medium models (EMMs), the VO<sub>2</sub> film is always treated as a homogeneous medium, and a unique effective permittivity is used to describe the whole film at each intermediate state (green).

Traditional EMTs have certain limitations when describing micro-scale structures. For example, as mentioned in section 2.2, Maxwell-Garnett equations assume that particles (the inclusions) that distribute randomly in the host material (the matrix) will always retain their role as the inclusions in the equation, even when the inclusions form a new matrix. They cannot reflect the favoured changes of composite materials in specific directions, which make it less effective to use most EMMs on inhomogeneous media. Here I start from a different perspective. The basic assumption of vertical growth models is shown in Fig. 22(a) that any intermediate phase between pure insulating and metallic phase can be defined as a mixture including VO<sub>2</sub> at two pure phases in certain proportions. The insulator to metal transition is regarded as the growth behaviour of the metallic VO<sub>2</sub>. This is fundamentally different from the EMTs, which can numerically define countless intermediate states. Next, I will explain why the assumption of vertical growth models may contribute to more accurate predication of the behaviour of phase

transitions in the real world.

For a VO<sub>2</sub> thin film (40~100 nm) grown on the substrate or any other materials, obviously, the thickness of VO<sub>2</sub> is extremely small compared with the other two dimensions, as the width or length of this device can be scales of millimetres or even centimetres. Therefore, it is considerable that there is a difference between the reaction rates in all directions if we apply external excitations like heating the sample from the bottom or the top. The directional preference of the phase transition is sometimes negligible when we study bulk materials or there is no external energy input. However, considering that the commonly used triggering methods for VO<sub>2</sub> phase transition are electrical or thermal excitation, the directional inhomogeneity cannot be ignored. In fact, it is difficult to effectively predict the specific growth direction (or there is more than one direction for all equivalent vectors used to describe the growth) inside the material and reflect it in the simulation of the periodic structure by current research methods [185]. As a result, in this work, I propose several simple forms of vertical growth models to describe the phase transition behaviour of VO<sub>2</sub> and compare them with EMMs.

Fig. 22 reveals the vertical growth models (VGM) and the main difference between VGM and EMM. It schematically highlights the distinctions between the VGM and the EMM, by using an example nano-device that contains a VO<sub>2</sub> thin film on top of a SiO<sub>2</sub> substrate. The VGM assumes that the phase transition always initializes at the top and/or the bottom surfaces of the VO<sub>2</sub> thin film, progresses atomic layer by atomic layer towards the film interior, and maintains a flat boundary between the two phases throughout the phase transition [Fig. 9(a)]. Three representative variants are plotted in Fig. 22(a), which are Type S (the phase transition progresses only from the interface with the substrate), Type A (only from the interface with air), and Type AS (from both interfaces and progresses at equal speed towards the film centre). This kind of vertical growth is in sharp contrast to the EMM [Fig. 22(b)], which requires all the intermediate states to be a macroscopically uniform mixture of the two phases. As VGM has one or two more interfaces than EMM, what happens at these interfaces will make them numerically different from each other, though they are both simplified theoretical models.

### 4.1.2. Multi-layered VO<sub>2</sub>-based films

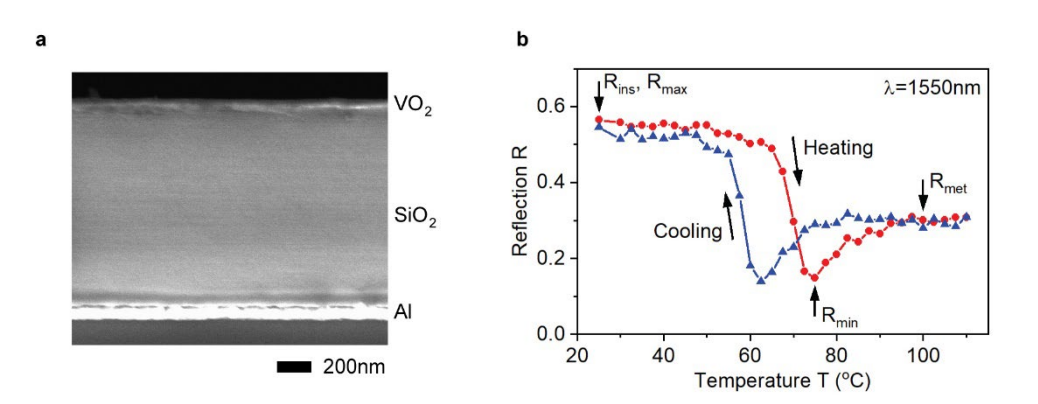


Fig. 23 SEM image and optical reflection measured on one of the two VO<sub>2</sub> thin films. (a) SEM image of a cross section of the sample, where the three optically functional layers of the multi-layered stack are labelled. The layer thickness is 40 nm (VO<sub>2</sub>), 1225 nm (SiO<sub>2</sub>), and 100 nm (Al). The scale bar is 200 nm. (b) Reflection of the film measured at near-normal incidence with the wavelength at 1550 nm. The temperature of the sample changes between 25 and 110 °C at a step of 2.5 °C, except at the low temperature end. The four distinct reflection values ( $R_{ins}$ ,  $R_{met}$ ,  $R_{max}$  and  $R_{min}$ ) used in further analysis are highlighted.

As the experimental benchmark used to compare and analyse different theoretical models, two high-quality VO<sub>2</sub> thin films have been fabricated and measured. These two films are very similar but target different wavelengths, and one of the samples is shown in Fig. 23. The sample is a multi-layered stack grown on top of a Si substrate that is revealed in Fig. 23(a). From the top to bottom, the layers are VO<sub>2</sub> (40 nm in thickness), SiO<sub>2</sub> (1225nm), Al (100 nm), and SiO<sub>2</sub> (200 nm). This sequence follows that of the optical solar reflectors developed by us recently [186], but it bears no planar nano- or micro-structures. Therefore, this structure has a great advantage when used to analyse optical quantities such as reflection or absorption during phase transitions as flat films reduce the complexity of the system, which ensures the analytical calculations will not involve complicated 3D structures. Only the top three layers (i.e., VO<sub>2</sub>, SiO<sub>2</sub> and Al) are optically functional in this experiment, as incident light cannot penetrate the 100-nm thick Al layer (in simple verification via a normal incidence model built in COMSOL, from 1.4 µm to 2 µm there is no transmission detected below a 50 nm Al layer, which means there is no loss for the system composed of the air and materials above the metal layer). The thicknesses of the VO<sub>2</sub> and SiO<sub>2</sub> layers are optimised to provide a large optical modulation during phase transition. Al<sub>2</sub>O<sub>3</sub> can be the alternative of SiO<sub>2</sub> used here as both have very limited effect on the transmission of lights from visible to infrared bands. However, thermal-deposited

SiO<sub>2</sub> has advantages in terms of the good heat-transfer feature, and it is more economic to use SiO<sub>2</sub> rather than a thick Al<sub>2</sub>O<sub>3</sub> layer under our fabrication conditions. The thickness is not specifically determined for my work, as it is only required to be large enough to avoid the reaction between VO<sub>2</sub> layer and metal reflection layer during the fabrication process.

It is worth highlighting that the VO<sub>2</sub> films were deposited by using the ALD (atomic layer deposition) method [187]. Many different methods are available to fabricate VO<sub>2</sub> thin films, including sol-gel [188, 189], magnetron sputtering [190-192], pulsed laser deposition [193, 194], chemical vapour deposition [195], epitaxy [196, 197], and ALD [198, 199]. We have chosen the ALD method for this work because it provides a high level of control over thickness, stoichiometry, and uniformity in thin film deposition. Our samples consequently can serve as a good experimental benchmark for examining analytical models. The specific experimental process is listed below (here the sample show in Fig. 23 is discussed only).

A Bühler Helios sputtering system is used to sputter an Al layer (100 nm) and a SiO<sub>2</sub> layer (1225 nm) on a SiO<sub>2</sub>-coated (200 nm) Si substrate. A VO<sub>2</sub> layer (40 nm) is then deposited on the top using ALD. The ALD is carried out in a Savannah S200 system, using TEMAV (98%) from Strem Chemicals and deionized water (oxidant). The VO<sub>2</sub> film is deposited at 200 °C, and the growth cycle number set to grow a 40 nm layer is 1100. The VO<sub>2</sub> film is then subsequently annealed in an AJA sputter in O<sub>2</sub> atmosphere (pressure at 40 mTorr, time for 1 hour, and temperature at 450 °C) to generate crystalline VO<sub>2</sub> (M1). The experimental conditions is also detailed in [200].

Fig. 23(b) shows the sample's reflection measured at near-normal incidence in a Fourier transform infrared microscope (FTIR) [82]. The microscope provides a broad spectrum, but to simplify the discussion, Fig. 23(b) only shows the wavelength of 1550 nm, a wavelength that is critical for telecommunications, which is the focus of this work. The full set of data is plotted in Fig. 24 below. In the measurement, the sample's temperature was first increased from 25 to 110 °C, and then ramped back to 25 °C, at a step of 2.5 °C except at the low-temperature end. A clear non-monotonic temperature dependence is observed in both the heating and the cooling processes of the thermal cycle. The reflection of the insulating phase ( $R_{ins}$ , taken at 25 °C) is 0.56, higher than that of the metallic phase ( $R_{met}$ , taken at 100 °C), which is 0.29. While the maximal reflection ( $R_{max}$ ) occurs at 25 °C and equals  $R_{ins}$ , the minimal reflection ( $R_{min}$ ) occurs at an intermediate temperature, which is 75.0 °C and 62.5 °C in the heating and the cooling processes, respectively. The value of  $R_{min}$  is between 0.14 and 0.15, a small value that approaches the critical coupling condition [80] where perfect absorption occurs (critical coupling in optics refers to the condition where the coupling rate of light into a resonator, such

as a microcavity or waveguide, is optimised to achieve maximum energy transfer. It occurs when the external coupling loss matches the intrinsic loss of the system, leading to complete absorption of the incident light without reflection or transmission). These four distinct parameters of  $R_{\rm ins}$ ,  $R_{\rm met}$ ,  $R_{\rm max}$  and  $R_{\rm min}$  are used to compute figures of merit such as the degree of non-monotonic nependence (DoND), which are used to compare the models against the experiment. This will be discussed in section 4.1.5.

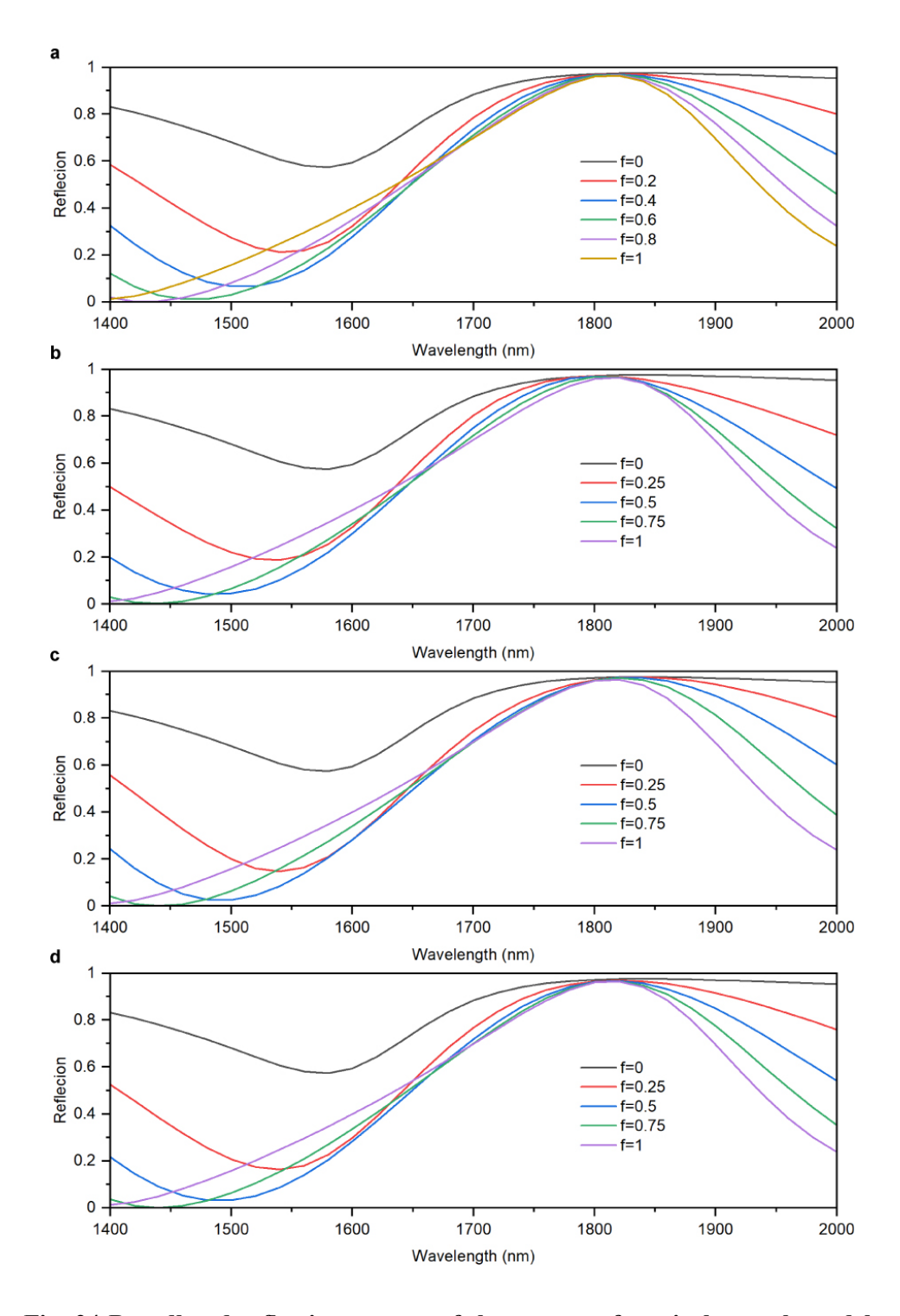


Fig. 24 Broadband reflection spectra of three types of vertical growth models

and Looyenga's model. (a) Looyenga's model. Since the available resolution of Looyenga's model in simulation is infinite, the step length of filling factor f is different from vertical growth models. (b) - (d) correspond to vertical growth model type S, type A and type AS. Very few differences can be observed from the broadband spectra.

Due to the lack of decisive technical support to verify the differences between the three hypotheses of vertical growth models (type A, type S and type AS), this work uses the reflection spectra of broadband simulation to expand the exploration of these models, and the results are shown in Fig. 24. As Bruggeman model and Looyenga's model are two of the most commonly used tools to describe the characteristics of mixtures, here Looyenga's model is selected for comparison. A comparison between Bruggeman model and Looyenga's model will be given in section 4.1.4 to verify these two models show high consistence in each other when using the VO<sub>2</sub>-based films discussed in my work as the benchmark.

#### 4.1.3. Temperature-dependent reflection measured at certain wavelengths

To explore how different theoretical models are used to describe the  $VO_2$  phase transition, the three main physical parameters involved in the experimental results and calculations of this work are reflection R, temperature T and volume fraction factor or filling factor f. The experimental results from Fig. 23(b) can directly reflect that the reflection is dependent on the temperature. However, both VGM and EMM are proposed based on the assumption that the characteristics of  $VO_2$  during the phase transition is dependent on the volume fraction factor f, which also means the reflection is dependent on f. Because the experimental data from the laboratory is measured at different temperatures, while the variable used for calculations is volume ratio, it is fundamental to prove that there is a direct correlation between the two variables, and the changes in the reflection characteristics caused by their monotonic changes are consistent before I can compare the calculated results and experimental results.

A useful method for establishing the relationship between two variables is to use an intermediate variable directly related to both of them to filter pairs of target variables that can produce the same or similar intermediate variable values, to establish a model that can describe the relationship between these two variables through mathematical fitting and other methods. In this work, the main difficulties that can be predicted are: (i) If there is a certain difference between the experimental data measured in the two pure phases and the values of two ends of the simulation model, it will greatly affect the accuracy of the fitting, which reduces the credibility of the entire method; (ii) Compared with the EMT models that allow adjustment of the interval of volume fraction factor, the vertical growth models are limited by the resource

requirements of finite-element calculation and cannot achieve dense sampling so that the fitting error may increase. (iii) The concept of volume fraction or filling factor is introduced by EMM to analyse homogeneous media. As I pointed out when introducing VGM, the basic assumption of EMM (the inclusions and the matrix are mixed to homogeneous media) does not match the actual situation, so volume fraction f and temperature T can only correspond numerically, but not physically. Next, I will explain how I establish the numerical relationship between f and T for further analysis.

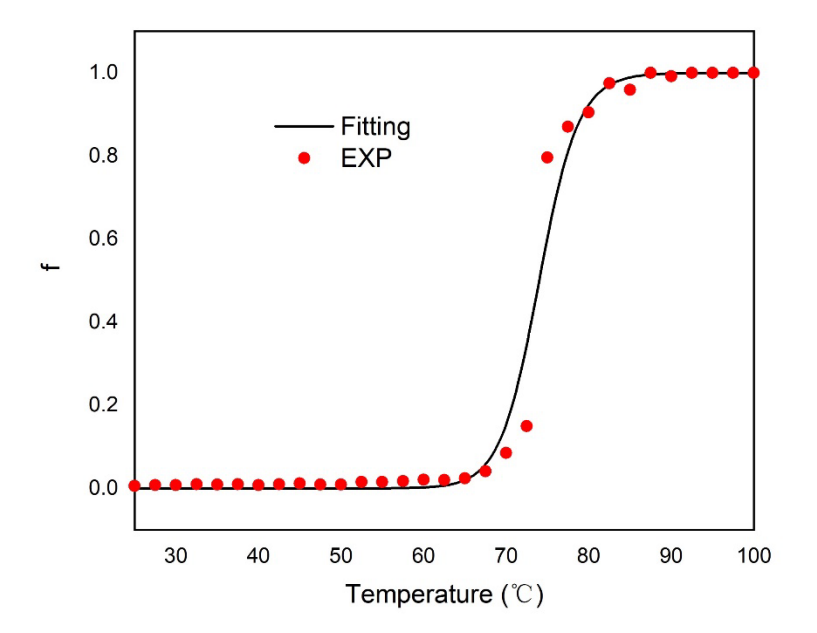


Fig. 25 Example of a relationship curve to convert temperature T and volume fraction factor f to each other (1550 nm). The y-axis variable f is selected from simulation data that the corresponding reflection is equal to experimental results measured at certain temperature. The values of temperature are set manually, and calculations are executed by MATLAB. (The fitting parameters calculated:  $W = 7 \times 10^{-19}$ ,  $T_{half} = 347$  K.)

The thermal hysteresis data (measured during the heating and cooling process respectively) of reflection versus temperature for the fabricated VO<sub>2</sub> sample illuminated by a light source whose wavelength varies from 1.4  $\mu$ m to 2 $\mu$ m is measured to extract the *R-T* (reflection-temperature) data pairs. For any certain wavelength (still begins at 1550 nm), establish a vertical growth model and an effective medium model and extract *R-f* (reflection-filling factor *f*) data pairs by simulation. By Eq. (8), filling factor *f* can be expressed as a continuous function related to *T*, which means for any value of *T* within the domain where Eq. (8) is applicable, a corresponding *f* can be found. The reflection efficiency is selected as the correlating variable. For the reflection value of every sampling point in the experiment (step length is 2.5 °C), a pair of temperature

and filling factors can be found that contribute to the same reflection. These data pairs are used to describe the relationship between temperature and filling factor by non-linear fitting. With plenty of data pairs, other coefficients in the equation can be determined. For those points where the corresponding value cannot be precisely located in the vertical growth model or EMT model due to accuracy limitations, select the one with minimum error in reflection instead. It is because the step length of experimental measurement is 2.5 °C, which affects the accuracy of reflection graphs of the experiment group, particularly the area where the reflection changes sharply. On the contrary, the curve produced by analytical calculation consists of an infinite number of data points theoretically. The main effect of this difference is the loss of experimental data points as shown in Fig. 25, when the temperature increases from 70 °C to 80 °C.

Fig. 25 shows a curve plotted by pairs of f and T. By filtering out the f and T whose reflections under the effective accuracy are closest to the experimental values, MATLAB can fit these two variables with mathematical modules (according to Eq. (8)). Since the formula depicts the dependence of f on T, the data pairs of f and T that contribute to the same reflection values are directly plotted as red scatters in Fig. 25, and the relationship fitting curve is plotted in the same graph. From the f curve it is more obvious that how fast the phase transition is. Actually, limited by the temperature step length, there is more error at the deep than expected, which is also what to improve in the future. However, as the values at the two ends (pure insulating and metallic phases) always overlap, and there are also a few effective points that overlap well near the deep, the fitting results can still be though to be reliable.

### 4.1.4. Reflection analytically derived from theoretical models

I first test the Bruggeman model and the Looyenga model, two frequently adopted EMMs, by trying to reproduce the experimental results (temperature-dependent change in reflection) shown in Fig. 23(b). Both models regard VO<sub>2</sub> undergoing the phase transition as a binary mixture, and they assign a unique effective permittivity  $\varepsilon_{eff}$  to each of these intermediate states [92, 201] Although they differ in the exact form of the formula, both models use these three parameters to calculate  $\varepsilon_{eff}$ :  $\varepsilon_{ins}$  (the permittivity of the pure insulating phase),  $\varepsilon_{met}$  (that of the pure metallic phase), and f (the volume fraction of the metallic phase, a real number that ranges from 0 to 1). The Looyenga EMM has a rather straightforward formula [15, 16, 25], which is the Eq. (7) given in section 2.2.1. Meanwhile, the Bruggeman EMM is more complicated and bears several variants. Here we choose the fundamental, symmetric formula [3, 4] following the original deviation, which is Eq. (4). At the beginning, the section will only discuss the single wavelength 1550 nm.

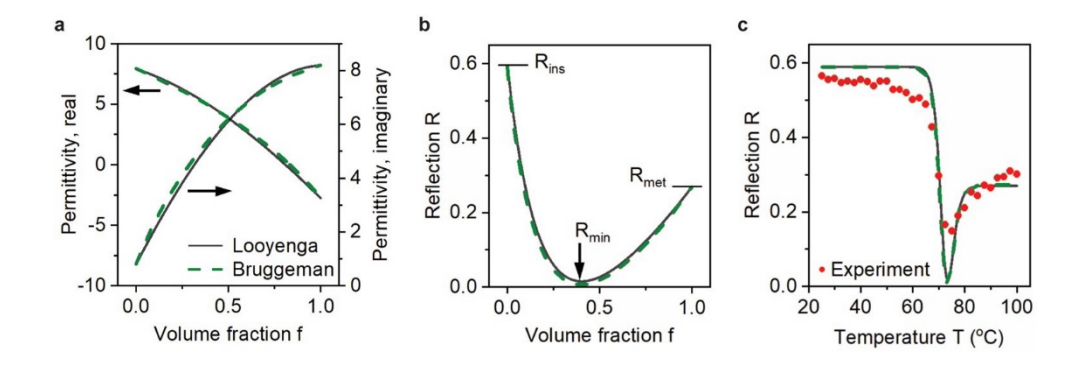


Fig. 26 Effective permittivity and reflection calculated based on the Looyenga (the solid black lines) and the Bruggeman EMMs (the dashed green lines). The wavelength is 1550 nm. (a) Treated as an effective medium, VO<sub>2</sub> possesses an effective permittivity  $\varepsilon_{eff}$  that changes continuously during the phase transition. Each state of this effective medium has a unique volume fraction f, which ranges from 0 (corresponding to the pure insulating phase) to 1 (the pure metallic phase). (b) Analytically calculated optical reflection of the multi-layered stack. Reflection at the pure insulting phase ( $R_{ins}$ ), the pure metallic phase ( $R_{met}$ ), as well as the maximal value ( $R_{max}$ ) and the minimal value ( $R_{min}$ ) in the whole phase transition are highlighted. (c) The analytically calculated reflection can be compared with the experimental reflection measured in the heating process, which are the red dots, first shown in Fig. 23(b), by translating f into temperature T.

These two formulas are used to produce the effective permittivity  $\varepsilon_{eff}$  of all the intermediate states [Fig. 16(a)]. In the calculation,  $\varepsilon_{int}$  and  $\varepsilon_{met}$  take the values of 2.82 + 0.14 *i* and 1.72 + 2.39 *i*, respectively, which are obtained in our ellipsometry measurement at the wavelength of 1550 nm [200]. As Fig. 26(a) shows, these two models produce almost identical values of  $\varepsilon_{eff}$  throughout the phase transition. Both the real and the imaginary parts of  $\varepsilon_{eff}$  show an almost linear and featureless dependence on *f* (note that the temperature dependence is nevertheless nonlinear, as *f* does not change with temperature linearly). Although both sets of plots of the real and imaginary parts of permittivity can be observed to exhibit a certain degree of curvature, they have been confirmed to change monotonically throughout the phase transition process (as volume fraction *f* varies from 0 to 1).

The reflection of the multi-layered stack shown in Fig. 23 is then calculated based on these values of  $\varepsilon_{eff}$  and shown in Fig. 26(b). The standard transfer matrix analysis is used, where the thicknesses of the VO<sub>2</sub> and the SiO<sub>2</sub> layers take the experimental value, while that of the Al layer is assumed to be infinite. The refractive indices of SiO<sub>2</sub> and Al are set as 1.4431 and 1.5750 + 15.6556 i, respectively [202, 203]. Because of the high similarity in  $\varepsilon_{eff}$ , the two

reflection curves produced by the Looyenga and the Bruggeman models are also very similar [Fig. 26(b)]. The reflection shows a profound non-monotonic dependence on f: it decreases from 0.59 (annotated as  $R_{ins}$  and  $R_{max}$  in the figure) at f = 0 to nearly zero ( $R_{min}$ ) at f = 0.4, before increasing to 0.27 ( $R_{met}$ ) at f = 1.

To directly compare with the experimental results in Fig. 23(b), the R-f curves (reflection versus volume fraction) in Fig. 26(b) are then converted to R-T curves (reflection versus temperature) and shown in Fig. 26(c). The details of this conversion has been explained in section 4.1.3. By viewing the co-existence of the two VO<sub>2</sub> phases as a first-order chemical equilibrium [18, 22, 204], this conversion is achieved by using Eq. (8). Fig. 26(c) shows the R-T curves calculated with  $T_{\text{half}} = 347$  K and  $w = 7 \times 10^{-19}$  J  $\approx 4.37$  eV, and the two curves are compared against the experimental results of the heating process in Fig. 23(b). The two analytical R-T curves well reproduce the experimental data in most of the temperature range, but deviation at around  $R_{\text{min}}$  is also easily noticeable. The analytical  $R_{\text{min}}$  is very close to zero (0.007 and 0.016 in the two models), as opposed to an experimental  $R_{\text{min}}$  of 0.15. It is worth noting that, the conversion from the R-f curves in Fig. 16(b) to the R-T curves in Fig. 26(c) does not influence the value of  $R_{\text{min}}$ ; the deviation in  $R_{\text{min}}$  can be traced back to Fig. 26(a), the starting point of effective medium modelling.

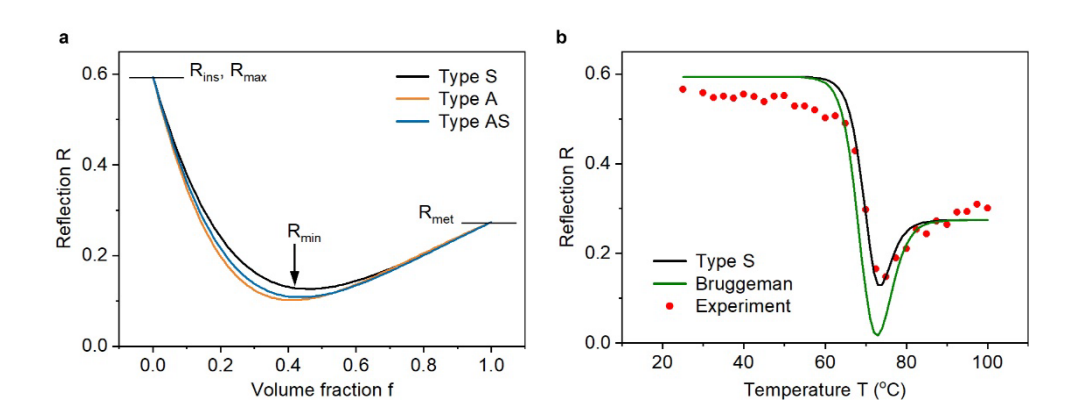


Fig. 27 Reflection derived from the VGM at the wavelength of 1550 nm. (a) The dependence of reflection on the volume fraction f for all the three variants, with  $R_{ins}$ ,  $R_{met}$ ,  $R_{max}$  and the approximate location of  $R_{min}$  highlighted. (b) The corresponding R-T curve of Type S, compared against the curve produced by the Bruggeman model and the experimental results. The curves of Type A and AS are omitted here due to their similarity to the Type S curve, and the Looyenga curve is omitted as well for a similar reason.

As illustrated in Fig. 27, the new VGM views the VO<sub>2</sub> phase transition differently from the classical EMMs. Nevertheless, the concept of volume fraction f remains useful: it is now simply

the thickness ratio of the metallic layer(s) and the whole film (40 nm here). The R-f curves of the three variants (i.e., Types S, A, and AS) are calculated [Fig. 27(a)], by using the same transfer matrix analysis and the same values of  $\varepsilon_{ins}$  and  $\varepsilon_{met}$  that are used for Fig. 26. These three R-f curves are very similar, and all show a clear non-monotonic dependence on f. Due to this high similarity and to improve visualization, only Type S is shown in Fig. 26b as the representative of vertical growth models. It doesn't mean that Type S shows better consistence than other two models, but just to facilitate the comparison between different theoretical models. The transformation from the R-f curve in Fig. 27(a) to the R-T curve in Fig. 27(b) uses the same values of w and  $T_{half}$  as in Fig. 26.

Fig. 27(b) also shows the R-T curve produced by the Bruggeman model which is shown previously in Fig. 26(c) and the experimental results that are shown previously in Fig. 23(b). The analytical values of  $R_{ins}$  and  $R_{met}$  are invariant between the VGM and the BMM, simply because they correspond to the two pure phases that are model-independent. The biggest difference between the two theoretical models is in  $R_{min}$ : the VGM generates a value that is much closer to the experimental data. To be more precise, the VGM gives better prediction near the deep ( $R_{min}$ ). As VGM and BMM have the same starting and ending point (in fact, any theoretical model has the same starting and ending point as only pure insulating or metallic VO<sub>2</sub> exists at these two points), the value of the deep determines the shape of entire reflection curve.

As far as the results are concerned, the advantages of vertical growth models are obvious, especially in the region where the phase transition is most rapid, the vertical growth models match the experimental results represented by the red scatters well, while BMM produces a certain gap. This is basically caused by their difference in the minimum value. Since the shape of a single-valley-shaped non-monotonic curve is mainly determined by the two ends and the lowest value, the lowest value closer to the experimental result means that the graph is much more consistent with experiments to a higher degree.

When comparing the data obtained on the experimental sample and the results of the two kinds of theoretical models, the comparison of absolute values mainly depends on the R-T curve, while the R-f curve is used for the comparison of shape. The reason is that the R-T curve is basically determined by three points ( $R_{ins}$ ,  $R_{met}$  and  $R_{min}$ ), and the influence of non-monotonicity on the curve shape is relatively limited, while the R-f image is highly likely to change shapely with the change of non-monotonicity.

### 4.1.5. Benchmarking using Degree of Non-monotonic Dependence (DoND)

As shown in Fig. 23(b) and the two figures in section 4.1.4, the temperature response of VO<sub>2</sub>

at the wavelength 1550 nm exhibits a characteristic that the reflection does not change monotonically with increasing temperature. When describing a physical process involving potential non-monotonic changes, a physical variable that can reflect the trend of change is very beneficial to the research. Some studies on VO<sub>2</sub> are based on its potential for perfect absorption (such as the solar absorber proposed in [186] and THz absorber in [205]). If I assume that the reflectivity of VO<sub>2</sub> varies monotonically with temperature over most wavelengths, perfect absorption is difficult to achieve at pure insulating or metallic phase. Therefore, a parameter that can describe the monotonic change (i.e., the relative depth of the deep of reflection curve) is of great significance for predicting the performance of VO<sub>2</sub> samples. A key novelty of this work is that I propose a new figure of merit called Degree of Non-monotonic Dependence (*DoND*) to judge which analytical approach is close to what happens in the real world. The *DoND* can be defined as:

$$DoND = Min(R_{ins}, R_{met}) - R_{min}$$
 (16)

where the variables correspond to the names marked in Fig. 18 below respectively.  $R_{ins}$  is the reflection value at the pure insulating state (starting point of R-f graph).  $R_{met}$  is the reflection value at pure metallic state (ending point of R-f graph).  $R_{min}$  is the minimum reflection value of the whole graph, which can overlap one of  $R_{ins}$  or  $R_{met}$ . Since the reflection value can be any value between 0 and 1 in theory, the theoretical domain of DoND can also be changed from 0 to 1. A DoND of zero means that the minimum point lies in one of the two ends, which also means that the curve changes monotonously. Take the heating curve in Fig. 28 for example, DoND can be used to describe the drop of a non-monotonic curve and the extent of its rise from the lowest valley. Two different wavelengths, 1345 nm and 1417 nm are selected to show different cases when  $R_{ins}$  or  $R_{met}$  is used to calculate DoND.

It is important to note that the phase transition of VO<sub>2</sub> involved in this work has been extensively researched. Its temperature-dependent changes are predictable. If any further research involves a very complex physical structure that produces temperature-dependent change that does not follow the case where only a single maximum or minimum value can be observed, then the concept of *DoND* or even this work itself cannot be used as direct guidance.

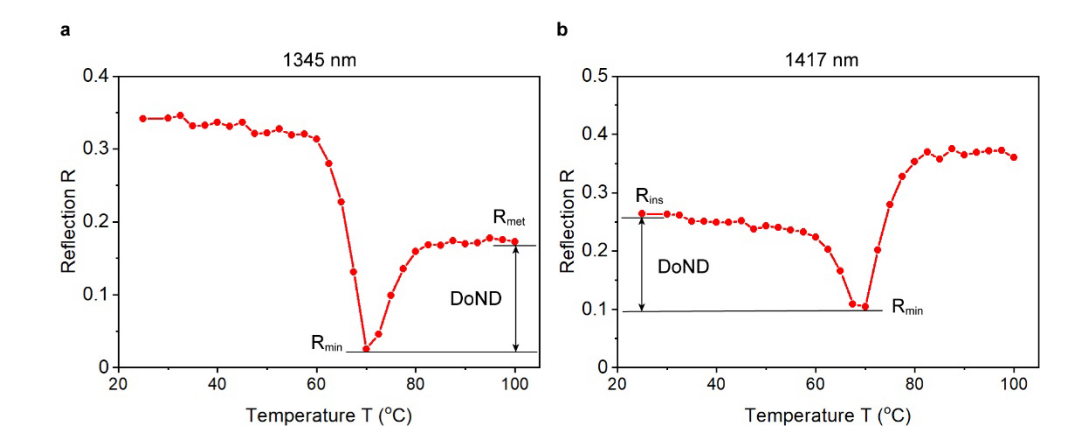


**Fig. 28 Definition of** *DoND* (**Degree of Non-monotonic Dependence**). To assist the interpretation of the parameter *DoND*, two examples are provided here, taken at (a) 1345 nm and (b) 1417 nm on the second sample. The formula of *DoND* is Min( $R_{ins}$ ,  $R_{met}$ ) -  $R_{min}$ . In panel (a), as  $R_{met}$  is smaller than  $R_{ins}$ ,  $DoND = R_{met}$  -  $R_{min}$ . In panel (b), as  $R_{met}$  is larger than  $R_{ins}$ ,  $DoND = R_{ins}$  -  $R_{min}$ .

Fig. 28 shows an example of extracting DoND from an R-T graph at two specific wavelengths. For the wavelength of 1345 nm, the reflection measured or calculated at the metallic phase (high temperature) is smaller than that of the insulating phase (low temperature). The DoND for this wavelength is the absolute difference between  $R_{\rm met}$  and  $R_{\rm min}$ . For the wavelength of 1417 nm, the reflection measured at the metallic phase is higher than that of the insulating phase, then the DoND should be  $R_{\rm ins}$  -  $R_{\rm min}$ . This rule applies to all wavelengths within the domain chosen for analysis.

With an analytical method for converting R-f and R-T graphs, it is possible to compare the measured results of the VO<sub>2</sub> sample with theoretical models including effective medium models and vertical growth models at multiple wavelengths. Since the optical properties of VO<sub>2</sub> for the light of different wavelengths (especially the near-infrared band) are quite different, in order to verify the applicability of different models, it is essential to simulate and compare simulation results of different wavelengths. In the initial stage of this work, it is shown that the wavelength range to be explored is 1.4  $\mu$ m  $\sim$  2  $\mu$ m, and the experimental data is collected accordingly. Firstly, it is necessary to ensure that the structure has no systematic defects. As mentioned before, the Al layer should achieve a reflection of more than 98% in this wavelength domain. Therefore, the structure designed in this work (also the dimensions of the experimental sample) can be regarded as satisfying the requirements of full reflection [206].

## 4.1.6. Quantified comparison against the experiment

In section 4.1.3, the experimental results of temperature-dependent change in reflection over the wavelength band from 1.4  $\mu m$  to 2  $\mu m$  are provided and 1550 nm is highlighted as an example. Then in section 4.1.4, VGM and BMM are applied for analytical calculations, which I use to derive the reflection from these two theoretical models. Before drawing any conclusion about the vertical growth models over 1.4  $\mu m \sim 2 \mu m$ , a comparison at 1550 nm can already show some clear results: (i) Near the starting and ending points, both VGM and BMM have some matching errors with the experimental data but give almost the same predictions. (ii) the main difference between these two models is located at the deep, where the phase transition occurs. The deep produced via VGM shows better consistence with the experimental results than that of BMM. (iii) At 1550 nm, for the VO<sub>2</sub>-based multilayer films, the VGM shows better performance on the prediction of phase transition behaviour than BMM.

The next and the most significant step is to extend this conclusion to a wider wavelength band and other  $VO_2$  samples, which provides the evidence that VGM is applicable to the research on phase transition materials. The extension of comparison is carried out in the wavelength band between 1.4  $\mu$ m and 2  $\mu$ m, where the experimental results can be used as the benchmark. For each wavelength where the comparison among VGM, EMM and experimental data is carried out, temperature changes from 25 °C to 100 °C, then the temperature-dependent reflection output measured or calculated via theoretical models is extracted.

Since each reflection value now corresponds to two variables: the wavelength and temperature, line plots can no longer show the relationship between reflection and these two variables. As a result, colourmaps with two variable axes are used to present the results, as shown in Fig. 29. Taking Fig. 29(a) as an example, here I'll simply explain how to read the results in a colourmap. The horizontal axis represents the wavelength varying from 1.4  $\mu$ m to 2  $\mu$ m, while the vertical axis corresponds to the temperature from 25 °C to 100 °C. For each combination of wavelength and temperature, a reflection value can be found on the colourmap (note that due to measurement error, the reflection can be larger than 1 sometimes in the experimental results). By observing the changes in brightness in the colourmaps (the higher the brightness, the higher the reflection), the changing trend of reflection with wavelength and temperature can be read from these maps.

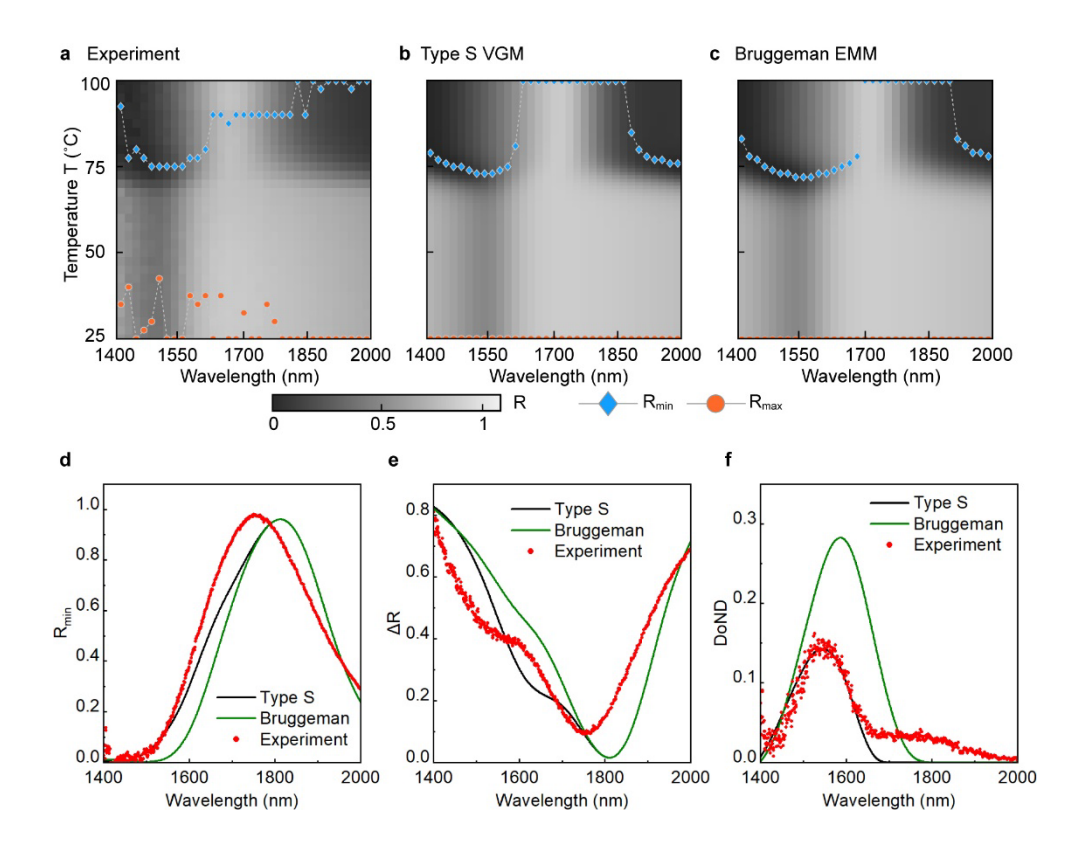


Fig. 29 Maps of reflection R, together with curves of figures of merit extracted from the maps. (a-c) Reflection maps in the wavelength range between 1.4 and 2.0 μm and the temperature range between 25 and 100 °C, obtained from (a) the experimental measurement, (b) the Type S VGM, and (c) the Bruggeman EMM. The experimental wavelength increments at approximately 1 nm, while the temperature points are as shown in Fig. 2(b). The upper limited of the scale bar is set at 1.1, as the experimental R is occasionally slightly above unity due to intensity fluctuation in light source. At each wavelength, the maximal reflection  $R_{\text{max}}$  and the minimal reflection  $R_{\text{min}}$  are highlighted using an orange circular and a blue diamond symbol, respectively. The theoretical  $R_{\text{max}}$  always stays at the bottom of the map, overlapping with  $R_{\text{ins}}$ . (d-f) Figures of merit derived from these three maps, showing (d) the minimal reflection  $R_{\text{min}}$ , (e) the modulation depth  $\Delta R$ , and (f) the degree of non-monotonic dependence DoND.

Fig. 29 shows how this comparison between VGM, EMM and experimental measurement is extended to a broad wavelength range between 1.4 to 2.0 μm. The calculation takes into account of the dispersion of SiO<sub>2</sub> and Al [202, 203], as well as that of VO<sub>2</sub>. Due to space constraints, Fig. 29 picks Type S of the VGM [Fig. 29(b)] and the Bruggeman EMM [Fig. 29(c)] to compare with the experimental results [Fig. 29(a)]. Results of the other two VGM variants (i.e., Types A and AS) and the Looyenga EMM can be found in Appendix B.

The three colourmaps of Figs.  $29(a) \sim 29(c)$  show a considerable variety of wavelength dependence (along a horizontal line in the maps) and temperature dependence (along a vertical line). Both the vertical growth model [Fig. 29(b)] and the Bruggeman model [Fig. 19(c)] can well reproduce the experimental results [Fig. 29(a)] across the whole wavelength and temperature ranges studied here. Nevertheless, consistent with the discussions in the previous two sections, small but noticeable differences exist between Figs. 29(b) and 29(c). To magnify these difference, other parameters need to be introduced based on the colourmap, which shows the reflection value corresponding to each temperature in the entire wavelength range to compare VGM and BMM.

From Fig. 29(d)  $\sim$  (f), I introduce  $R_{min}$ ,  $\Delta R$  and DoND as the figures of merit.  $R_{min}$  is the minimum reflection directly extracted from the colournaps, which is relative to the design of full absorber or low reflection solar devices. The modulation depth  $\Delta R$  is the absolute drop from maximum to minimum reflection. It's the theoretical limit of design with modulation function. For example, if the VO<sub>2</sub> films can be stabilized at a certain intermediate state where the R reaches the minimum value, a larger contrast can be obtained than that between the two pure phases. The last figure of merit DoND has been introduced in section 4.1.5 in detail, which won't be explained here.

Tabulation of these figures of merit (i.e.,  $R_{\rm min}$ ,  $\Delta R$  and DoND) involves one, two and three parameters, respectively, from the pool of  $R_{\rm ins}$ ,  $R_{\rm met}$ ,  $R_{\rm max}$  and  $R_{\rm min}$ . Consequently, Figs. 29(d) ~ 29(f) provides three different perspectives of the original experimental and theoretical data, allowing for a thorough examination of the theoretical models. They show that the Type S VGM and the Bruggeman EMM are mostly equivalent in their accuracy, with the VGM slightly outperforming the EMM in certain cases. The contrast between these two theoretical models is particularly clear in the DoND of a 100-nm window centred at approximately 1550 nm. The VGM provides an excellent fitting to the experiment, while the EMM can overestimate by as much as 0.17.

To further compare these two kinds of models (i.e., the VGM versus the EMM) and also exclude the peculiarities of the results extracted from a single sample, a second VO<sub>2</sub> film was fabricated and measured, and the same analysis as described above was conducted. This sample was fabricated following the same procedures, and the only difference from the first sample was in the thickness of the SiO<sub>2</sub> layer, which was changed from 1225 nm to 1100 nm. As seen in Fig. 30, this change in reflection against wavelength keeps the overall shapes of the optical features but shifts them to shorter wavelengths. To meet with this change, the beam splitter of the Fourier transform infrared microscope was changed from KBr to CaF<sub>2</sub>, allowing us to access shorter

wavelengths down to 1.0  $\mu$ m. Nevertheless, the shortest wavelength of the data produced via theoretical models could not be adjusted and remained at 1.4  $\mu$ m. It is not limited by the ellipsometer, as the original refractive indices used to build both VGM and EMM are from a measurement from 1.4  $\mu$ m to 2  $\mu$ m. Consequently, only the wavelength ranges from 1.4 to 2.0  $\mu$ m can facilitate the model comparison. Nevertheless, on this new sample, we can arrive at the same conclusions as mentioned in the preceding section. The VGM and the EMM are mostly equivalent in their accuracy in reproducing the experimental results, and the former slightly outperforms the latter in some aspects [most noticeable in Fig. 30(c)].

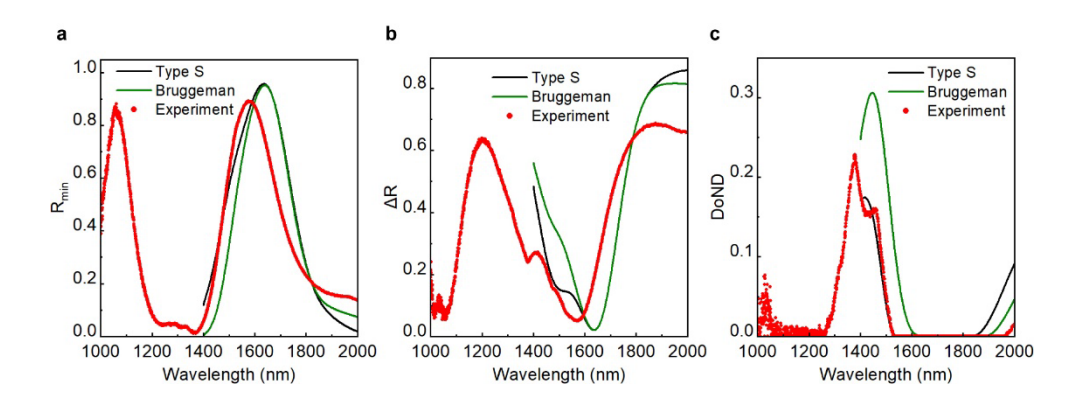


Fig. 30 The three figures of merit, (a)  $R_{min}$ , (b)  $\Delta R$  and (c) *DoND* for the second sample, which has a similar geometric configuration, but wavelength-shifted optical features as compared to the first sample. The experimental reflection covers a different wavelength range, now from 1.0 to 2.0  $\mu$ m, but the wavelength range available for modelling remains to be from 1.4 to 2.0  $\mu$ m.

The results of Figs. 29 and 30 provide critical insights into modelling VO<sub>2</sub> phase transition. Firstly, it is worth highlighting that, the analytical results of these two figures are computed following the same approach of Figs. 26 and 27. The VGM and the EMM use the same input values (i.e., the permittivity of VO<sub>2</sub>, SiO<sub>2</sub> and Al, and the thicknesses of VO<sub>2</sub> and SiO<sub>2</sub>) and there is no freely tunable parameter. Consequently, the differences between the two analytical models seen in Figs. 29 and 30 solely originate from their assumptions of the phase transition, i.e., a layer-by-layer transition in the VGM, versus a homogeneously mixed medium in the EMMs. Because these two opposite assumptions can both reproduce the experimental results, also considering that recent TEM observation has excluded the existence of a phase mixture in epitaxial VO<sub>2</sub> thin films [26], we conclude that the fundamental assumption of the EMMs could be wrong for VO<sub>2</sub> thin films. Good fitting between EMMs and experiment does not imply that the VO<sub>2</sub> thin film under study has any macroscopically uniform phase mixture.

Interestingly, although the VGM and the EMMs represent two opposite views of the VO<sub>2</sub> phase

transition, we can transfer one view to the other by allowing for some changes in a VO2 thin film at the microscopic scale. For example, consider the Type S variant of the VGM shown in Fig. 22(a), where the metallic phase forms a uniform layer at the bottom of the VO<sub>2</sub> film. If we slice this uniform layer into tiny pieces and allow them to flow freely upwards to different heights inside the film, we will obtain a macroscopically uniform mixture of the two phases. However, there is still no effective method that allows us to directly observe the changes in different components within the mixture during the phase transition process. Therefore, hypothetical models (like VGM and EMM) based on different calculation methods are still the main means for predicting experimental results, which is also the purpose that I propose the VGM. The similarity between the VGM and the EMMs is seen in Figs. 26 and 27 can be attributed to the fact that, for a VO<sub>2</sub> thin film at an intermediate state, its linear optical properties are relatively insensitive to the vertical distribution of the metallic phase. This conclusion is supported by the similarity between the three variants seen in Fig. 27(a). At the same f values, these variants produce similar reflections, even though they differ in the spatial distribution of the two coexisting phases. It is worth noting that, this analysis does not apply to thicker films, where optical interference will amplify the differences between these variants of the VGM, as well as the differences between the VGM and the EMMs.

## 4.2. VO<sub>2</sub>-enabled tunable metalens

#### 4.2.1. Parameters of elements in the metalens array

From the fabrication perspective, benefiting from the support provided by the cleanroom, I can grow a VO<sub>2</sub> layer with a thickness as low as 40nm, which has been verified in the previous work by experiments. The phase transition characteristics of VO<sub>2</sub> at this thickness are observable at the optical level, while thinner films might not contribute to obvious contrast between its two pure phases. In Appendix G, I provide the results to show contrast between pure insulating and metallic phase VO<sub>2</sub> films when the thickness decreases to 2nm. There is some evidence to support that ultra-thin VO<sub>2</sub> films may be detrimental to phase transition applications: (i) when the thickness comes to 10 nm, the contrast between two pure phases experiences a significant drop. (ii) For films thinner than 30 nm, the error in thickness increases a lot, which is limited by the ALD process (by using same processing parameters, the error in a 20 nm film reaches 36.3%, which is unacceptable).

However, from Eq. (15), it is convincing that  $VO_2$  films of this thickness are insufficient to achieve  $2\pi$  phase coverage and be used in metalens designs that have high requirements for phase modulation ability. As introduced in section 3.4, I did parametric sweep on the thickness

of both Si and VO<sub>2</sub> layers to obtain a combination that provides good phase coverage. Over all combinations, Si of 280 nm is chosen to provide a large phase coverage, as materials with higher refractive indices (also means large difference between the material and air) show more significant light modulation capability. VO<sub>2</sub> thickness is set to 180 nm to balance the tuning ability and the negative effect on phase coverage. The relationship between them can be explained by Eq. (15) as well: (i) the ability of light modulation (I focus on the phase here) is determined by the refractive index *n* and thickness, which makes a thicker layer of Si necessary. (ii) The tunability of the device is endowed by the VO<sub>2</sub> film. A thicker VO<sub>2</sub> film contributes to a large contrast between its two pure phases. However, as the *n* of VO<sub>2</sub> at any state is lower than that of Si, a too thick VO<sub>2</sub> layer will affect the performance of the device. (iii) For a complicated device like this, parametric sweep enabled by cluster computing is an efficient way to find a proper combination of thicknesses of Si and VO<sub>2</sub> layers.

Then a parametric sweep on side lengths is executed to obtain the element library. The main reason for choosing 100 nm to 800 nm as the sweeping range of side lengths originates from the planar dimensions of the meta-atom. Here the free-space wavelength  $\lambda$  is 1550 nm. To be able to create a smooth output wavefront from the scattering of discrete meta-atoms, the planar periodicity of the meta-atoms has to be smaller than  $\lambda$ , ideally by at least a few times. It is because diffraction occurs when the light passes through structures (slits or periodic gratings) whose dimensions are smaller than the wavelength of the light itself [119, 125]. The metalens works based on diffraction, which requires the period of its elements smaller than the work wavelength. By balancing several design limitations, I choose a periodicity of 1 μm, as specified in Fig. 21. The upper limit of pillar side lengths a and b obviously has to be smaller than this value. In fact, a large value of a and b can make the gap between adjacent pillars very small, and this creates two problems. First, the adjacent nano-pillars can produce near-field crosstalk, and the output wavefront will deviate from analytical prediction. Second, a small gap means a high spatial resolution in nanofabrication, which could make future experiment verification very challenging. Through my individual etching experience, the etching rate of a certain material strongly depends on the aspect of the structure to be etched. For drying etching of Si, a gap under 100 nm may cause a large drop in the etching, which consequently results in errors in the height of nanopillars. To ensure the etching rate is formal along the entire surface, a minimum gap of 200 nm is reserved in the design, which sets the upper limit of pillar side lengths a and b as 800 nm. The step length is set to 5 nm, which is possible to achieve with the support of E-beam lithography.

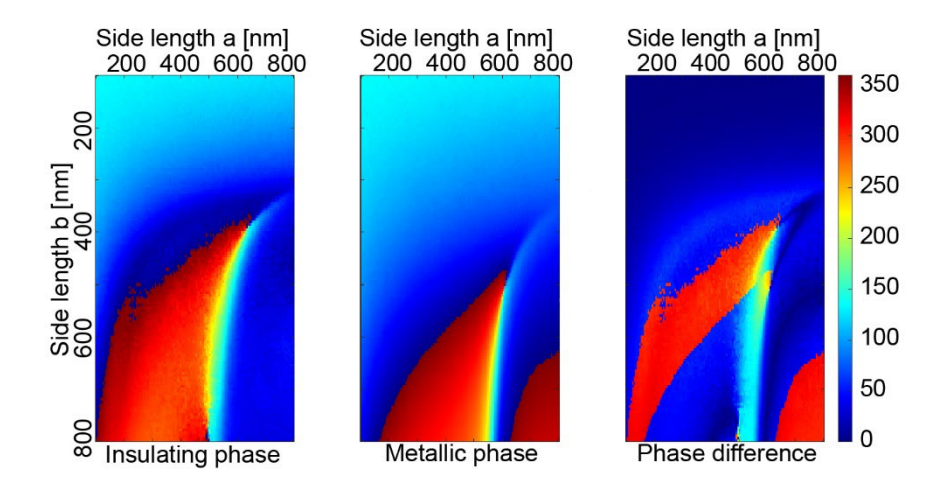


Fig. 31 Reflection phase with respect to different side length a and b obtained by parametric sweep via Lumerical simulation. The values of a and b change at a step of 5 nm. The colour corresponds to the reflected phase recorded at the height of  $2\lambda$  above the structure (from 0 to 360 degrees). The difference in the optical phase between the two material phases of VO<sub>2</sub> is also show to highlight the contrast. The incident light is 1550 nm.

Before analysing the results of Fig. 31, here I describe the simulation method that I used to produce the results. Considering the advantages of FEM simulation, it is easier to converge (FDTD uses rectangle mesh, which is not as accurate as triangle mesh used in FEM, especially at the corners) when performing parametric sweeps on a single-unit model and the results can be accessed and saved at any time, here I used COMSOL to collect the data required to establish the element library. The geometric structure is built according to the design shown in Fig. 30 with all dimensional parameters set as Fig. 30 illustrates. A plane wave source of 1550 nm is used, which is incident from the top. As the unit works in a metalens array, the boundaries along the x and y directions are set to be periodic (for a general separate model, PML can be used instead). Perfect Matched Layers (PML) are set on the top and bottom boundaries to avoid reflection occurring at these boundaries, as they have special absorption characteristics that make them act as effective absorptive buffers in numerical simulation. Side lengths a and b [Fig, 21] are variables for the parametric sweep, which correspond to the x and y axis in Fig. 31. The colour represents the reflected phase calculated at the height of  $2\lambda$  above the structure, changing from 0 to 360 degrees.

Fig. 31 shows the optical phase of light reflected by the meta-atoms, under plane wave illumination from the top. The phase shown in the colournaps has been wrapped into a range from 0 to  $2\pi$  (360 degrees). With the VO<sub>2</sub> segment at the insulating phase, a full  $2\pi$  phase coverage is observed in the library. The same observation can be made with the VO<sub>2</sub> segment

at the metallic phase. This observation suggests that a metalens can be created by extracting elements from the library. By comparing the optical phase between the insulting and the metallic  $VO_2$ , a large contrast is observed, which also covers a full  $2\pi$ . This observation suggests that tuning in the light focus could be achieved by changing the material phase of the  $VO_2$  segment. The colournaps in Fig. 31 can be regarded as a collection of side length data, and each set of side length a and b and their corresponding phase can be extracted from the datasheet file, which makes it the 'element library'.

#### 4.2.2. Metalens design and setup of simulation environment

Once the element library in Fig. 31 is built, the next step of the metalens design is selecting suitable elements from the library. This is also often the most challenging step of the whole design process. What makes it difficult is many factors contribute to the overall performance of the metalens, such as the dimensional parameters of each meta-atom and the size of the metalens array. Reserve design is widely used as a general solution to it, which means determining the details of a metalens derived from the results we want (such as the specific phase profile output).

The process mainly involves mathematical and analytical methods and also applies some programming skills. The selection program can be divided into three stages, which are produced and run on MATLAB. The first stage includes the definition of key parameters such as the dimensions of metalens and the input of the library (read all the variable pairs of side lengths a and b and corresponding phase data from the simulation results of parametric sweep). The second stage includes the determination of the centre element by exhaustion, the production of the theoretical hyperbolic phase profile, the matching between the elements from the library and the theoretical profile, and the calculation of the error. The third stage is mainly responsible for outputting the results in the form of datasets that can be exported to other software for further processing and plotting the results as images for direct access to key information. Some critical details of the program will be explained next. Table. 3 below gives a brief outline of the procedures.

Table. 3 Procedures to select metalens elements with the aid of an adaptive algorithm

Step	Procedure	Parameters involved	
1	Extract data (phase) from COMSOL and	a, b and corresponding	
	output as spreadsheet format.	phase $\varphi$	
2	Read the data and write them to MATLAB	a, b and corresponding	
	matrices.	phase $\varphi$	

3	Define the parameters of the metalens. The	Focal length $fl$ , $x$ and $y$ to	
	number of elements determined.	locate each single element	
		in the array	
4	Loop 1: determine the centre element by	$\varphi_{offset}$ which is explained	
	exhaustion.	in Eq. (14)	
5	Produce the ideal phase profile based on	The calculation is based on	
	the centre element and the hyperbolic	Eq. (14)	
	formula		
6	Loop 2: match the phase profile curves by	MSE, cumulative error	
	all elements in the library	ΔMSE	
7	Determine the elements located in all		
	positions that contribute to a minimum		
	cumulative error		
8	Output the parameters of these elements	a, $b$ and corresponding $x$	
	with respect to their position (distance to	and y to locate these	
	the centre)	elements	

The results of the parametric sweep are derived from the simulation software COMSOL and then written in the form of numerical matrices (for MATLAB processing, usually text form or datasheets are applicable) after a series of preprocessing such as normalizing the phase to the range of  $0 \sim 2\pi$ . In these matrices, each unique element design is recorded by a pair of side lengths a, b and the corresponding phase  $\varphi$ . New matrices are defined in MATLAB to store these parameters. [Steps 1 and 2 in Table. 3] The most important step in stage one is to input the size of metalens and the designed focal lengths of both insulating and metallic states [Step 3 in Table. 3]. As explained by Eq. (12), there is a trade-off between the radius and focal length of the metalens. For a given radius, an excessively large focal length means a smaller numerical aperture and a consequent reduction in the number of phase periods that fit the hyperbolic distribution defined by Eq. (12), resulting in significantly lower power efficiency and quality of focus [46]. Conversely, if the focal length is too short, the output from the edges of the metalens is bent at a large angle, and the focus can be easily affected by near-field interference between adjacent nanopillars. Besides, since the number of elements arranged on the radius is fixed, too many phase periods mean fewer data points on every single period, which greatly reduces the resolution of the actual phase profile and might cause a failure in focus. By considering all these factors, the radius is set to 20.5 µm with 21 elements on the radius including the centre element, and the focal length is set to 30 µm at insulating state and 40 µm at metallic state respectively. The incident light remains as a plane wave with a wavelength of 1550 nm. This specific combination of focal length and metalens size can be determined by

referring to the NA of the existing designs. For different materials and illumination conditions, different initial conditions should be selected for the first attempt, and adjustments should be made based on feedback.

The matching process in the second stage is mainly based on the error between the whole set of elements and the theoretical pattern [Steps 4 to 7 in Table. 3]. The main indicator used to compare different solutions is the sum of the mean square error (MSE) of all units. The element that requires special treatment in the selection program is the centre unit. Its phase determines the phase offset required to match the theoretical hyperbolic profile and thus plays a decisive role in the entire array. Excessive deviation in the initial phase can strongly interfere with the unit selection. To avoid this situation, the MSE-based selecting program is split into two main loops: the first loop is used to exhaustively enumerate the centre unit to ensure that all selections are compared when each element in the library works as the centre unit [Step 4 in Table. 3]. The second loop follows a general idea that matches each unit in the metalens array in order and obtains the sum of MSE for comparison [Step 6 in Table. 3]. This program can efficiently find a set of solutions with the smallest MSE at both phases of VO<sub>2</sub> when the number of selectable elements is limited. The formula used to produce target phase profiles is the modified hyperbolic formula, which is modified from the general form in Eq. (12), but with an offset phase value that is equal to the phase produced by the centre element:

$$\varphi(d,\lambda,fl) = \frac{2\pi}{\lambda} \left( \sqrt{d^2 + fl^2} - fl \right) + \varphi_{offset}$$
 (17)

It is also worth mentioning that this scheme defines the weight factor of insulating state and metallic state, and results with a relatively smaller error in one of the states can be obtained by changing the weight factor value. In this work, the weight factors of the insulating and metallic state are 0.5 and 0.5 respectively, while it can be tuned for other designs (e.g., switchable metalens that focus at one phase but defocus at another working state). The matching results are shown in Fig. 32. The phase profiles of the insulating state and metallic state are plotted separately. The continuous curves are the theoretical profiles produced by hyperbolic functions. The hyperbolic function applied in this step is Eq. (17). The offset phase is equal to the phase of the centre unit. For Fig. 32(a) and 32(b), the focal length fl is set as 40  $\mu$ m. For Fig. 32(c) and 32(d), fl is set as 30  $\mu$ m.

To exhibit the periodic phase gradient and highlight the periods, Fig. 32 (a) and (c) are produced by wrapping the original profiles shown in Fig. 32 (b) and (d). The dots correspond to the units arranged along the radius. Among these graphs, blue curves correspond to the phase profiles when VO<sub>2</sub> work at the insulating (low temperature) phase, while the red curves represent the

metallic phase (high temperature). The phase profiles produced based on Eq. (14) are smooth curves as Fig. 32 (b) and (d) show, which can be approximated by arranging several discrete elements along these patterns. Black dots represent the simulation phase of the selected elements from the library. It can be observed that the matching to the theoretical curve of the insulating phase is much better than that of the metallic phase in terms of the first  $2\pi$  period. The main reason is that the refractive indices extracted from these metallic elements are far from the optimal profiles. However, if we unwrap the phase distribution curve in Fig. 32 (c) and obtain the plots in Fig. 32(d), the errors actually contribute to a limited effect on the phase gradient along the radius of metalens.

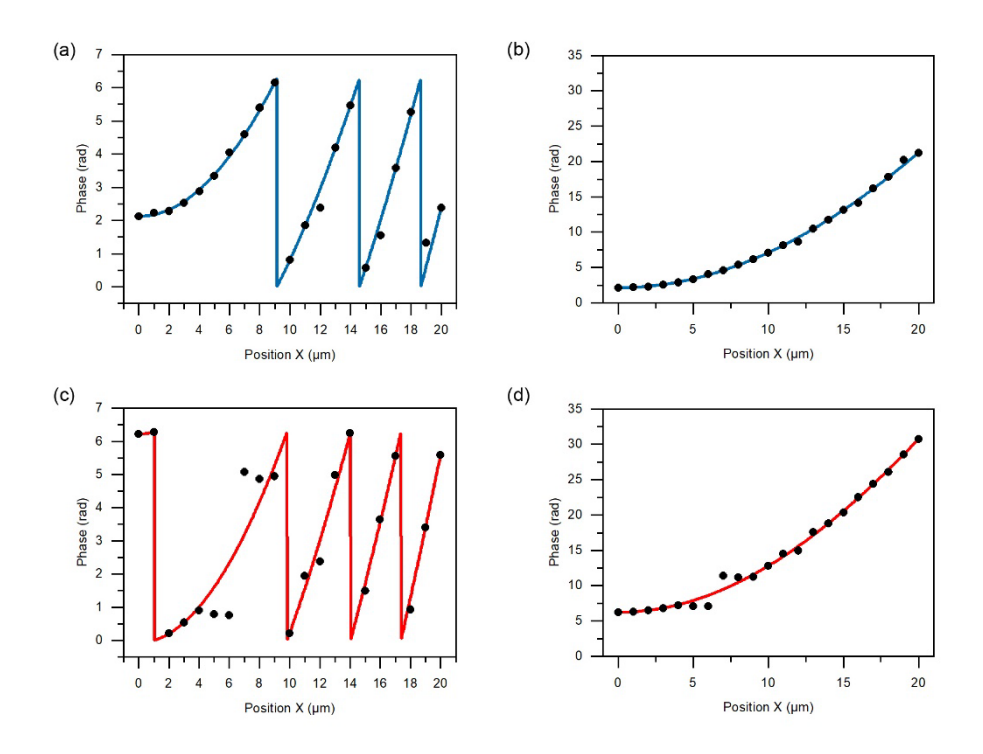
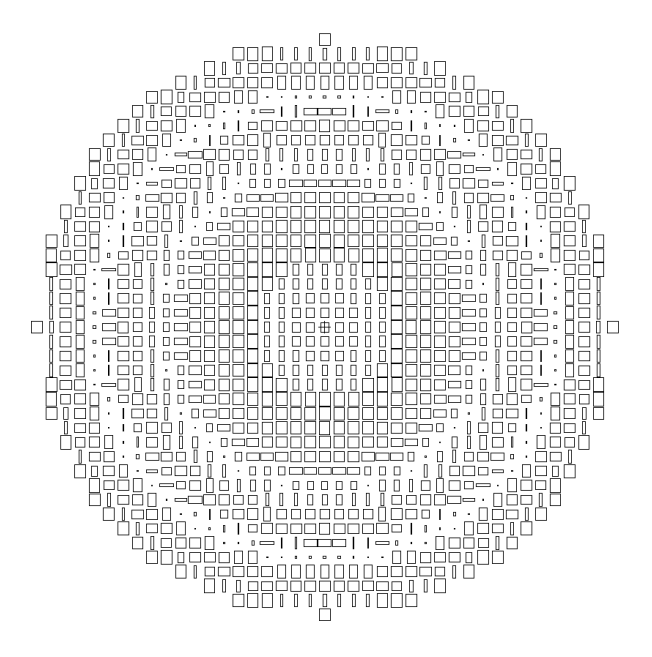


Fig. 32 Target (solid lines) and simulated (dot) phase profile along the x direction. (a) and (b) are phase profiles for the insulating  $VO_2$  metalens determined by hyperbolic distribution. The phase of matching elements are plotted as black dots. (a) is obtained by wrapping (b) back at  $+2\pi$ . (c) and (d) are phase profiles for the metallic  $VO_2$  metalenss, with (c) as the wrapped version of and (d). The 21 dots in each panel correspond to the elements along the radius of metalens.

The last stage of the design is the export and visualization of data. FDTD is used to implement this step. FDTD is a numerical method that discretises the simulation space into rectangular mesh, then calculates the electromagnetic fields in these mesh cells by Maxwell's equations. The calculation is repeated within the set time domain, which allows the calculation to be

extended to an extra-large structure or a huge amount of mesh cells. The platform I use for FDTD is Lumerical, which is widely used in numerical simulations of nanophotonics and optical devices.

Since the metalens structure is ultimately to be implemented in FDTD simulation on Lumerical, I use an efficient workflow: as the main variables in this design, side lengths a and b, and the distance to the centre d for positioning are exported as data sets. I have written a set of programs that can automatically draw the pattern from the top view based on the official instructions of L-edit. By running this macro script on L-edit, the pattern of metalens can be exported in GDSII format and used directly for geometric model creation on Lumerical. This means that only the thickness and physical conditions need to be defined during the simulation. There is no need to review the dimensions of specific meta-atoms, which improves the efficiency of repeated simulation and verification. Considering the scale and mesh size of the metalens, to reduce the simulation load, I take advantage of the four-fold rotational symmetry of metalens and only simulate a 1/4 of the total area. The output of the whole metalens can be derived from the simulated results based on the symmetry. The pattern generated in L-edit is shown in Fig. 33 below. The parameters of elements are listed in Appendix C.



**Fig. 33 Layout of the designed metalens pattern viewed from above**. The dimensions of each element are determined by using a MATLAB program. The values are then imported via c++ scripts. This layout view is output by L-edit.

L-edit is usually used to design masks and provide patterns for photolithography and other patterning processes in the fabrication process. Here I mainly use its function of outputting GDSII files to reduce the complexity of the model design by completely importing the metalens structure into Lumerical. By simply replacing the dimensional parameters and focal length of the metalens to design, different matrices generated by MATLAB can be quickly imported into the simulation tool in this way, thus significantly saving preparation time before simulation.

## 4.2.3. Binary focus tuning implemented by numerical simulation

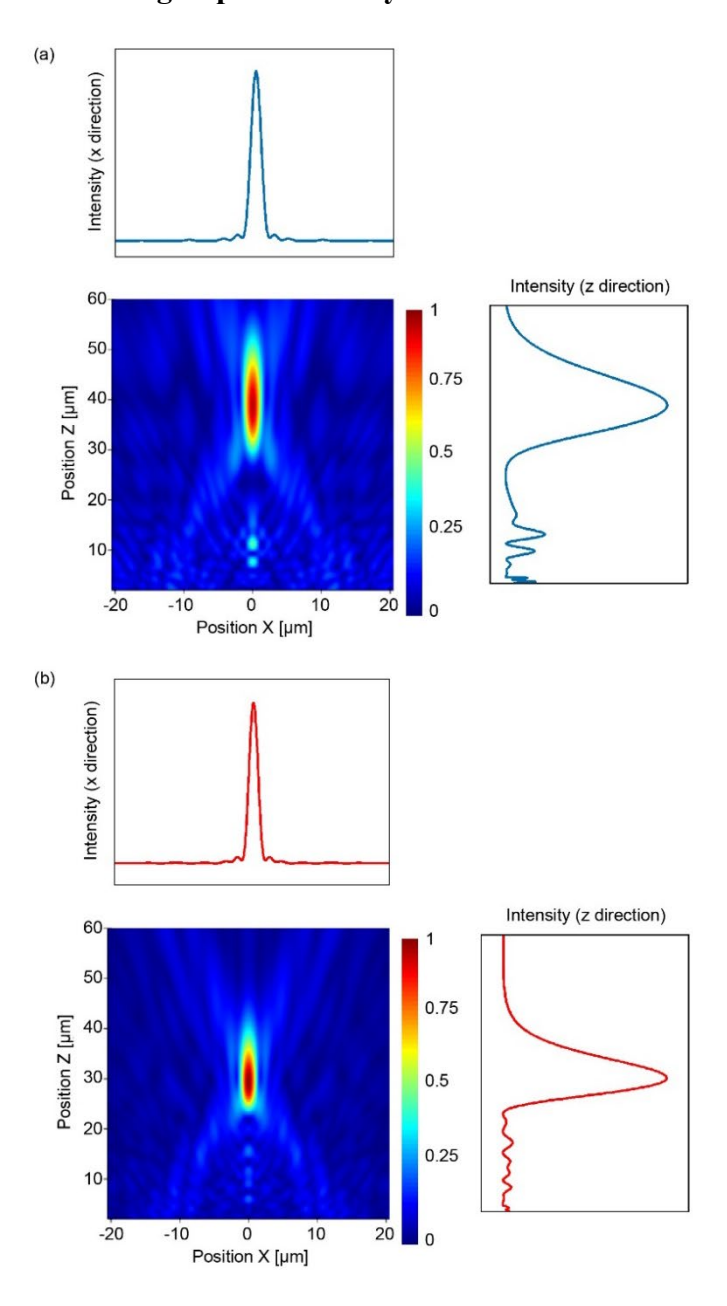
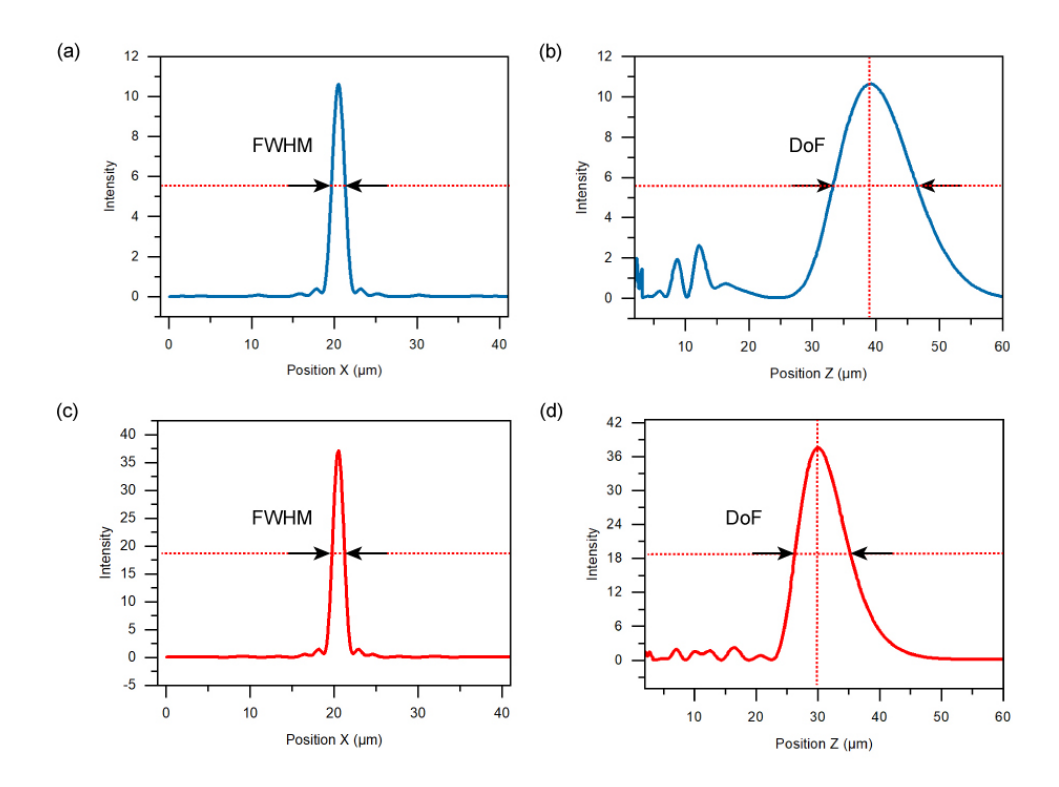


Fig. 34 Distribution of electric field intensity to show binary tuning of the metalens. (a) Normalised electric field intensity in the reflection, clearly revealing a focus. The focal length extracted from the results is  $39.27 \, \mu m$ . The VO<sub>2</sub> is at the pure insulating phase. (b) The output of the same metalens corresponding to the pure metallic phase. The focal length is now  $30.00 \, \mu m$ .

As described in the previous section, the target functionality of this VO<sub>2</sub> metalens is binary focus tuning. The metalens is designed to focus light at a distance that differs between the pure insulating phase and the pure metallic phase. This binary tuning is successfully observed in numerical simulation, and its characteristics are analysed in detail in this section.

After importing the GDSII file into Lumerical, a 2D planar pattern is generated, in which the length and width of each single unit are directly imported. Following the parameters shown in Fig. 21, the thicknesses of the  $VO_2$  layer and Si layer are set to 180 nm and 280 nm respectively. A square Si substrate is used as the substrate of the metalens. Its thickness is set as 4.65  $\mu$ m. The structural dimension is an integral multiple of the incident wavelength, which is beneficial to the settings of ports and monitors), following the value used in the COMSOL simulation. The diameter of the entire metalens is 41  $\mu$ m, and 41 repeat units are arranged along the diameter including the centre unit. The Si substrate is a square with a side length of 41  $\mu$ m. The edges of the substrate set the boundaries of the FDTD simulation range in the *xy*-plane. For the *z* direction, the simulation extends from the bottom surface of the Si substrate all the way up to 60  $\mu$ m above the surface of metalens.

Fig. 34 shows the binary focus tuning of the metalens, with the  $VO_2$  at the low-temperature insulating phase and the high-temperature metallic phase in Fig. 34(a) and 34(b), respectively. The colour maps show the normalized intensity of the output electric field intensity in the *xz*-plane. They reveal the position and the size of the focus. It is clear that the metallic phase corresponds to a shorter focal length. The target functionality of binary focus tuning is successfully observed in these simulated device outputs. To numerically observe the pattern of intensity change, the curves of the field intensity changing along the x and z directions are displayed on the side of the 2D image of the electric field distribution map. These curves will be used later to show how to extract physical parameters, as shown in Fig. 35.



**Fig. 35 Extraction and calculation of focus parameters at insulating state**. (a) and (b) Intensity distribution along x and z direction for insulating phase. (c) and (d) Intensity distribution along x and z direction for metallic phase. The horizontal dot line corresponds to the half-maximum intensity, where the erengy fall is -3dB with respect to the peak. The vertical dot line corresponds to the vertical position where the intensity peak appears, which can be used to measure the focal length. The method to extract full width at half maximum (FWHM) and depth of focus (DoF) are marked on the graphs.

The size and the depth of the focus can be extracted from the field maps shown in Fig. 34, by plotting out the field intensity along straight lines that pass across the centre of the focus. These graphs are shown in more detail in Fig. 35. Based on the intensity distribution along the x-axis, the full width at half maximum (FWHM) of the focus can be extracted. Based on the intensity distribution along the z-axis, the focal length and the depth of focus (DoF) can be extracted. Both FWHM and DoF are parameters to describe the shape and size of the focal point, which are significant for the evaluation of the device design. These values are listed in Table. 4 as shown below. It is worth mentioning the focal length here. The designed values are 40  $\mu$ m and 30  $\mu$ m for the insulating and the metallic VO<sub>2</sub>, respectively. The corresponding simulated values are 39.27  $\mu$ m and 30.00  $\mu$ m. The design and the simulation match very well. Considering that the units used to build the metalens are not perfect, this matching results show the design tolerance of the metalens I design.

**Table. 4 Focus parameters calculated at the insulating and metallic phases.** Focal length *fl* and reflection intensity are directly read from the simulation results. Full width at half maximum (FWHM) and depth of focus (DoF) are extracted to be compared with the wavelength of incident light (1550 nm) to show the change in focus during binary tuning.

VO <sub>2</sub> phase	fl (designed)	fl (simulation)	FWHM/λ	DoF/λ	Reflection intensity
insulating	40 μm	39.27μm	0.563	8.845	0.093
metallic	30 μm	$30.00 \mu m$	0.485	6.161	0.13

From Fig. 35 and Table. 4, the change in size of the focus point is acceptable and supports the implementation of binary focus tuning. Considering that the optical properties of VO<sub>2</sub> show continuous changes during the phase change process, I selected several intermediate states for simulation calculations and extracted their focusing conditions. The specific results are elaborated and discussed in the next section.

## 4.2.4. Quantified analysis of the tunable metalens

After achieving binary focus switching at the simulation level as stated in section 4.2.3, I make attempts to explore the possibility of implementing other optical functions such as continuous tunability. To this end, I conduct the analysis based on the original metalens array (i.e., retaining the choice of units from the previous section).

In Appendix C, the dimensional parameters of all 21 units along the x-direction have been obtained. Based on this, I extract the output phase of these 21 units in a separate simulation. The simulation settings are totally same to that I use for parametric sweep: I set one unit and all boundaries periodic, then the unit works individually without the effect from other structures. In order to more clearly show the regulations of phase change rather than change in the absolute values, I normalize all the output phases to obtain Fig. 36 below. The basis is from Fig. 32. If the phase profile of the entire x-axis of the metalens is wrapped into  $2\pi$ , it can be found that the output phase of the unit at some positions increases with the phase transition from the insulating state to the metallic state. On the contrary, the output phase at some positions decreases. Therefore, in an ideal situation, if the phase change of each unit at the corresponding position follows the change law of the phase profile, it is theoretically possible to achieve continuous focus tuning.

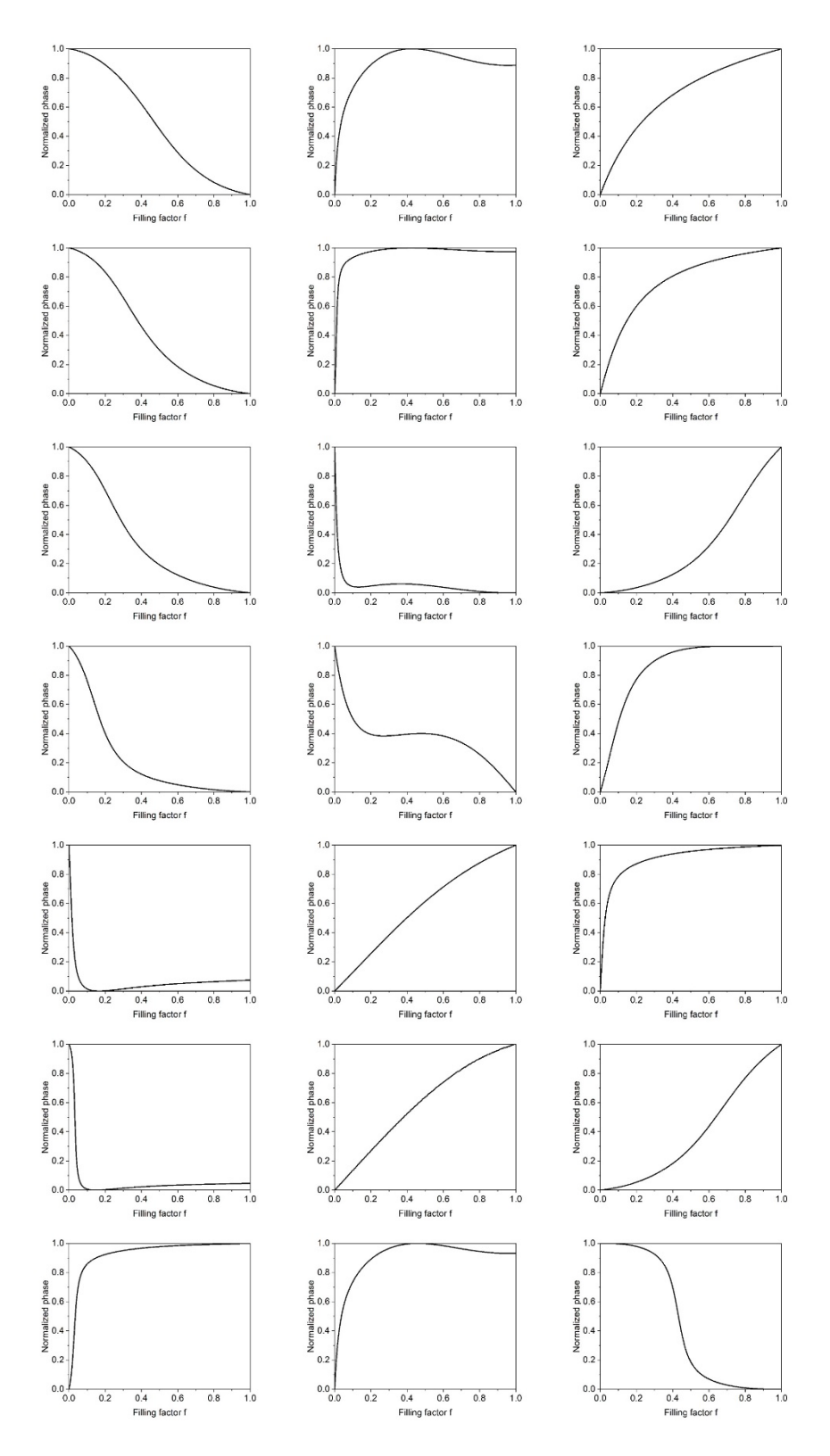


Fig. 36 Graphs of normalised phase against filling factor f of units along x-axis.

The phase is normalized to  $0 \sim 1$  to show the changing trends in similar scales. First column corresponds to element  $1 \sim 7$  from centre, which are arranged along the radius. The second and third columns show output phase graphs of element  $8 \sim 14$  and  $15 \sim 21$ , respectively.

Fig. 36 shows the change in the output phase during the phase transition of several representative elements to support the conclusion that the reflection characteristics of elements in the metalens array are not regular, which makes it difficult to generalize a useful conclusion for further design of continuously tunable metalenses. As the filling factor *f* increases from 0 to 1, some elements show a monotonic change in the phase, while some exhibit a non-monotonic change. The change doesn't follow any patterns such as the dimensions of these elements. As a result, I failed to explain the implementation of continuous focus tuning based on the reflection characteristics of these individual elements. Nevertheless, given that the metalens is somewhat tolerant to imperfections in some of its units (since the output of the metalens is the result of all the units working together, it does not necessarily match the behaviour predicted by a single unit), I still do simulation on the continuous focus tuning, and the results are described in detail in section 4.2.5.

## 4.2.5. Continuous focus tuning and extended applications

As discussed in results of vertical growth models stated in 4.1, the refractive index of VO<sub>2</sub> changes continuously in the phase transition, and this change can be described using various theoretical models. Although the metalens here is designed to produce a binary focus change, I have calculated its focal properties with the VO<sub>2</sub> segment at a series of intermediate states. Interestingly, a gradual change in the focal length is observed in the simulation, and the results are discussed in this section.

To extend the simulation from the two pure  $VO_2$  phases to the intermediate states, the complex refractive index of these intermediate states has to be calculated first. Here, I choose the Looyenga effective medium model and list the calculated results in Table. 4. I have not used the vertical growth model described in the previous chapter. There are two reasons to stop me using the vertical growth model proposed by myself: (i) the structure used in this work (Si- $VO_2$ -Si) involves a large amount of interfaces, which contributes to a significant increase in simulation workloads. (ii) For analytical methods, the 3D structure is not multilayer film anymore. Instead, there are air gaps between the units, which makes it impossible to apply transfer matrix methods or other calculation tools that are only applicable to flat films. As a result, Looyenga's model is used as an alternative. It is expected that the vertical growth model would produce similar results here, based on the conclusions of the previous chapter. Following the discussion of the previous chapter, the filling factor f is used here to characterize the intermediate states. In Table. 4, its value is tuned from 0 to 1 at a step of 0.1, and the complex refractive index associated with each f value is listed. The wavelength is 1550 nm. Both the real part and imaginary part of the refractive index show a monotonic dependence on f.

Table. 4 Refractive indices of  $VO_2$  used in the metalens simulation. The refractive indices of the two pure phases (i.e., f = 0 and 1) are experimental values obtained in our own measurements. The refractive indices of the intermediate states are computed using the Looyenga effective medium model. The wavelength is 1550 nm.

Volume fraction factor f	Real refractive index n	Imaginary refractive index k
0 (insulating)	2.469	0.0557
0.1	2.400	0.297
0.2	2.331	0.538
0.3	2.263	0.779
0.4	2.194	1.020
0.5	2.125	1.261
0.6	2.056	1.502
0.7	1.987	1.744
0.8	1.919	1.985
0.9	1.850	2.226
1 (metallic)	1.781	2.467

By using these refractive indices in the same simulation process, a total of 11 field maps are obtained, each corresponding to a unique value of f. Fig. 37 below lists all of these maps.

Fig. 37 lists the 11 field maps corresponding to the work states of metalens during the VO<sub>2</sub> phase transition as the filling factor f changes from 0 to 1. The focus exhibits a regular change in both its size and position. When f = 0 (VO<sub>2</sub> works at pure insulating phase), the focal length reaches the maximum value (39.27  $\mu$ m). As f increases with a step of 0.1, the focal point moves down along the z direction, which means the focal length decreases. The decrease in focal length continues until f = 1 (VO<sub>2</sub> works at pure metallic phase). As for the size of focus, it experiences a certain degree of expansion when f increases from 0 to 0.2, and then shrinks all the way down to its minimum until f = 1. Judging from only the 11 points selected and listed in Fig. 36, during the entire phase transition process of VO<sub>2</sub>, this metalens achieves a monotonic and continuous change in its focal length (serious monotonicity needs to be verified).

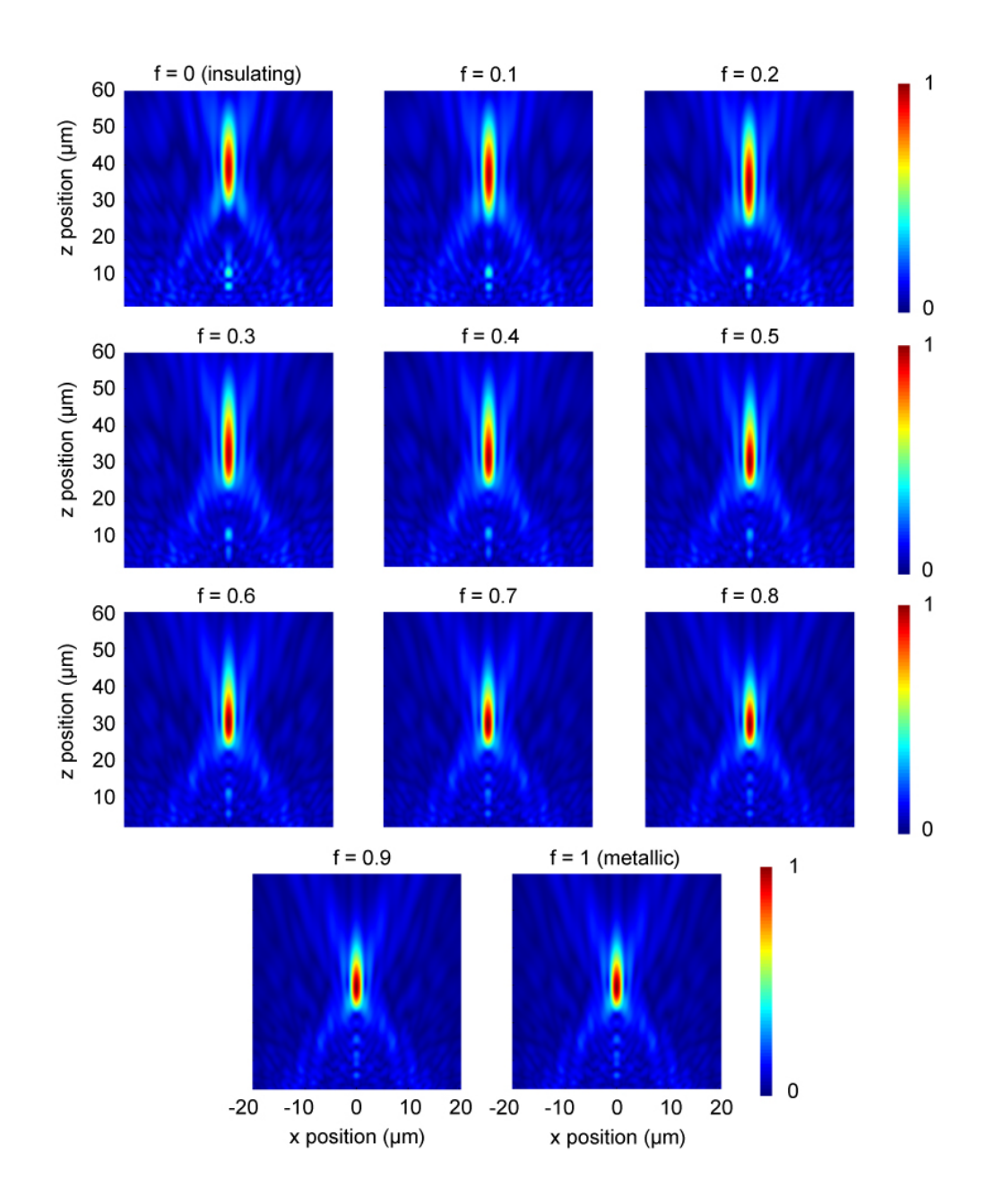
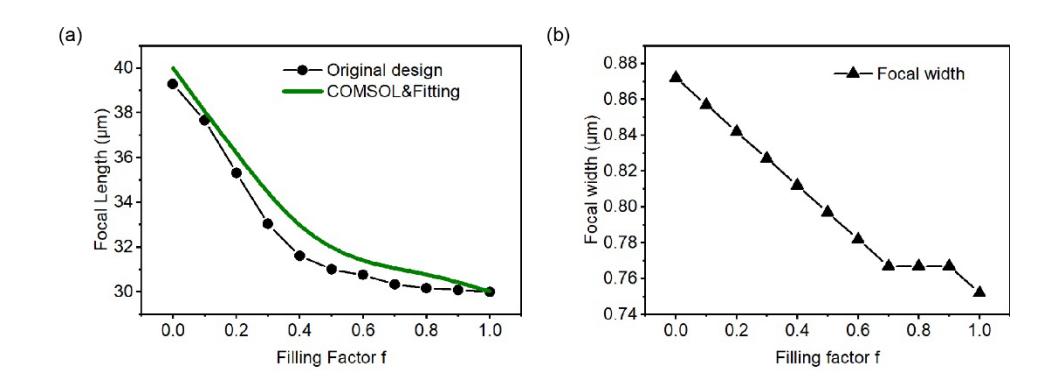


Fig. 37 Electric field distribution in xz-plane that shows the position and shape of focusing point. The x-axis of all graphs are the position along x direction. The y-axis of all graphs are the position along z direction. The colourmap represents the normalized electric field intensity. Filling factor f varies from 0 to 1 with a step of 0.1, which simulates the phase transition of  $VO_2$  from pure insulating phase to metallic phase.

The focal length and the FWHM of the focus are then extracted using the same method that is used for Fig. 36 shown in section 4.2.4. To summarise this method, it contains these main steps: (i) The output electric field is simulated first. (ii) The focal length is then extracted from an intensity monitor that passes through the centre of the metalens in the vertical xz plane. The

extracted value provides the information of the focal length. (iii) The simulation model is then slightly modified by adding an intensity monitor in the horizontal xy plane. The vertical position (i.e., the z position) of the monitor depends on the result of the previous step, which reveals the height of the focus centre. (iv) The simulation is then repeated, and the new monitor provides the information on the FWHM of the focus. By repeating these four steps over all the f values, I obtain the results shown in Fig. 38.



**Fig. 38 Continuous tuning of the VO<sub>2</sub> metalens**. (a) The dependence of the focal length on the filling factor f. The scatters and lines are simulation results from Lumerical on the whole metalens. The green curve is obtained by non-linear fitting based on the original phase output by COMSOL. Note that the scale of y-axis (focal length) is from 30 μm to 40 μm. (b) The dependence of the focal width (i.e. FWHM) on the filling factor f. Note that the scale of y-axis (focal width) is from 0.74 μm to 0.88 μm.

Fig. 38 shows the dependence of two focus characteristics (the distance and the size of the focus) on the filling factor f. As each value of f corresponds to a specific temperature in the phase transition, the results of Fig. 37 directly reveal the temperature-based tuning of the  $VO_2$  metalens. It is clear that both the distance and the size of the focus change continuously with f. It means that they will also change continuously with temperature in the temperature window of the phase transition. The dependence of the focal distance on f is particularly interesting because it shows that the metalens could be used for continuous zooming. This continuous zooming could be achieved by temperature control and does not require any mechanical movement. In fact, I have used a similar approach in my exploration of VGM, which is to install an independent heating plate on the bottom of the device. This heating plate can increase or decrease the temperature of the device in step lengths of about 2.5 °C. For reflective metalenses, the heating plate will not have any effect on the optical path, so it is more conducive to temperature monitoring. For transmissive designs, more complex heating methods such as ring heating circuits are required.

I have provided an estimation of the focal length at each value of f and shown it in Fig. 38 as well. The estimation is based on a hybrid method that combines COMSOL numerical simulation and the analytical equation of Eq. (17). At each f, I first numerically simulate the phase profile of all the meta-atoms across the metalens. This phase profile is then analytically fitted using Eq. (17). This fitting produces an estimated focal length. The results are plotted to produce the green curve in Fig. 38, which is close to the pure numerical results. Although a generalised method for designing continuously tuneable  $VO_2$  metalens has not been achieved, I have made some attempts based on the existing simulation results. This part of the work is detailed in Appendix D.

#### 4.3. Fabrication work

### 4.3.1. Exploration on ICP etching rate of Si

To fabricate the metalens I designed and stated in section 4.2 and use it for further measurements, I have made a series of experimental preparations, including receiving training in E-beam lithography resist coating, inductively coupled plasma (ICP) etching, ALD and other correlative experimental procedures. Limited by the feasibility of the design and the supply of the VO<sub>2</sub> precursor (TEMAV), the experiment has not been completed. Since ICP etching is essential for all fabrication processes my work may involve to reshape the Si structure for further deposition of VO<sub>2</sub>, here I briefly discuss a series of tests that I have conducted in testing the ICP etching process.

There are three main etching methods that our cleanroom provides technical support to, including ion beam etching (IBE), reactive ion etching (RIE) and inductively coupled plasma RIE (ICP). I have been trained in all three etching methods. When it involves the etching process of Si, ICP is my first choice due to its high anisotropy (can achieve sidewalls nearly vertical) and high etch rate. Roughly speaking, ICP is based on RIE, with extra induced electric fields on the sides of the chamber to enhance the impact of plasma beams on the target materials. It thus can increase the intensity and the aspect ratio of etched patterns. Since the structures my work involves are basically on the nanometre scale, precise control of the etch rate control is essential. Here I will use Si as an example to introduce how I determine the etch rate of ICP.

Among all factors to affect the etch rate, ICP power and RF power play a decisive role [207]. During all recorded etching processes, the ICP power fluctuates from 799 W to 800 W, with a reflected rate from 1.25% to 7%. The RF power floats from 49 W to 51 W, with a reflected rate from 9.9% to 16%. It can be basically considered that these two power indicators are stable, and the errors caused are within the acceptable range. Other factors that may influence the etch

rate include (i) the size of the carrier wafer, which affects the reflection of plasma beams. (ii) The materials of the carrier wafer and chips (or wafer) to etch. (iii) The recipe of the etching process. In our cleanroom, vertical etching (VE) and shallow etching (SE) are two commonly used recipes to provide different etch rates.

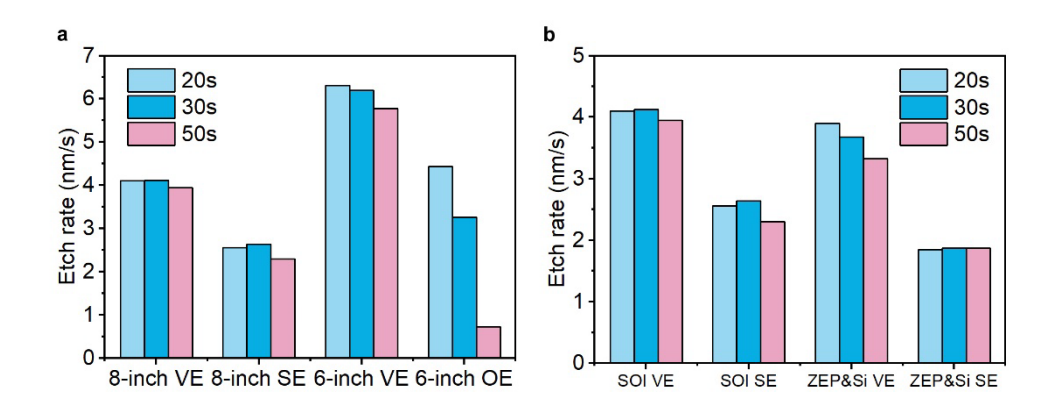


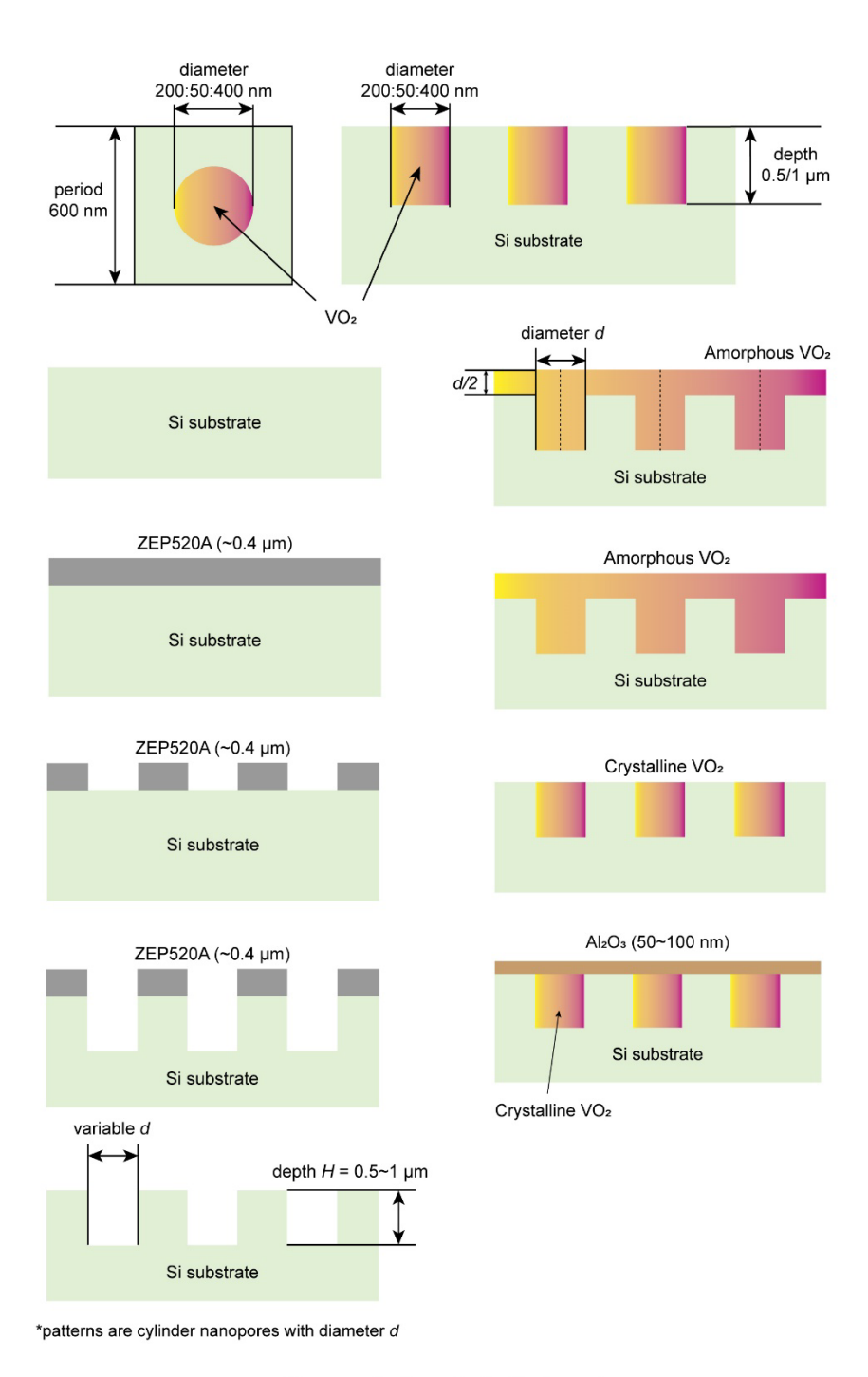
**Fig. 39 Etch rate measured from different SOI-based samples with different etching recipes.** There are two recipes commonly used in our cleanroom for a-Si etching: vertical etching (VE) and shallow etching (SE). For each sample, the etching is divided into 3 stages. (a) Comparison among SOI dummy chips using VE and SE recipes and placed on different carrier wafers respectively. (b) An 8-inch Si wafer is used as the carrier. The bare SOI chips are compared with the SOI chips coated with ZEP520A in terms of the etch rate.

The results are shown in Fig. 39. In Fig. 39(a), SOI dummy chips are used for etching tests. 3-stage etching is used to get feedback from experimental measurements and adjust the process time, which is designed to prevent the negative impact of systematic errors. Note that one group is set to be over-etched by using the thinner Si layer. In Fig. 39(b), another sample with the e-beam resist ZEP520A coated on the Si is also measured. Some simple conclusions can be made from Fig. 39(a): (i) the etch rate of the VE recipe is much faster than that of SE. (ii) By comparing the results of 8-inch carrier and 6-inch carrier groups, a smaller carrier wafer contributes to a higher etch rate. (iii) At the moment when the Si layer is completely etched (SiO<sub>2</sub> exposed), the etch rate exhibits a rapid decrease. For a mixture of two materials, the etch rate will not be equal to that of etching them separately. The etch rate measured from the ZEP-coated sample also supports it.

#### 4.3.2. Fabrication of embedded VO<sub>2</sub> fillings

In this section, I will introduce a design based on VO<sub>2</sub> filling embedded in the Si substrate. This design is carried out after I completed the initial proposal and exploration of VGM, aiming to

find a more accurate description of phase change behaviour and causes through more complex structures. Since this design has not been completed and used for characterisation, its functions and correlative theoretical background will not be described in detail. This section will focus on the completed experimental part and introduce the fabrication processes related to VO<sub>2</sub>. The schematic of the device and the entire fabrication process are shown in Fig. 40. As of the time of writing this thesis, all procedures before the coating of Al<sub>2</sub>O<sub>3</sub> and dry etching of VO<sub>2</sub> have been completed.



\*thickness ratio does not reflect the true scale

Fig. 40 Fabrication process of the embedded  $VO_2$  filling. The basic element of this device is the cylinder  $VO_2$  filling buried in the Si substrate. The depth of these fillings is 0.5  $\mu$ m. The diameters varies from 200 nm to 400 nm with a step of 50 nm. The main fabrication procedures are shown in the figure, which include: resist coating, E-beam lithography, etching, and ALD. The dimensions do not reflect the true scale of the structure.

The process starts with the E-beam lithography. The ZEP520A is coated at 4000 rpm for 60 seconds, which produces a resist film of  $\sim$ 400 nm. ICP etching is then executed to produce holes with a high aspect ratio for VO<sub>2</sub> to fill. Then as introduced in section 3.1, I choose ALD as the method to deposit VO<sub>2</sub> (to be more precise here it remains VO<sub>x</sub> as the ratio between vanadium and oxygen is not determined yet) into these holes. Then the top layer of VO<sub>2</sub> films is etched to reshape the surface, which aim to eliminate the interference with the VO<sub>2</sub> fillings. Annealing process is then done to precisely control the ratio between vanadium and oxygen, which means the VO<sub>2</sub> used for functional targets is as pure as possible. The final step is to deposit a thin Al<sub>2</sub>O<sub>3</sub> film onto the top by ALD. As described before, the phase transition of VO<sub>2</sub> causes a non-negligible density change, which is around 5% in volume. The Al<sub>2</sub>O<sub>3</sub> film is required to limit the volume change of the VO<sub>2</sub> films, thereby constraining its phase transition. The design was originally intended to explore the possibility of artificially interfering with the phase transition, but ultimately, I failed to characterise them experimentally.

Here I'll detail some of the procedures in Fig. 40. After developing the sample at room temperature for 90 seconds in ZED N50 and 30 seconds in IPA, ICP etching is completed to produce the grooves. The selectivity of ZEP520A: Si is 1:3 theoretically, but according to the tests shown in Appendix E, ZEP520A of 400 nm can support the etching of Si up to around 800 nm, which is sufficient for this design. The resist is then stripped by ultrasonic treatment in NMP solution at 60 °C for 4 hours. The ALD of VO<sub>2</sub> is detailed in Chapter 1. The main materials involved are TEMAV precursor, H<sub>2</sub>O (oxidant), N<sub>2</sub> or Ar (carrier). The TEMAV is heated to 85 °C, then the growth occurs at 150 °C. Before the annealing process, the chip is cleaved into small chips for different annealing conditions. The annealing (crystallization) is processed in an Agile Nanofab system. The initial condition is set according to VO<sub>2</sub> of 500 nm, which is 400 °C, 1 Torr, 4 hours. The mask design layout is shown in Fig. 41, and the photo and SEM images of these chips are shown in Fig. 42.

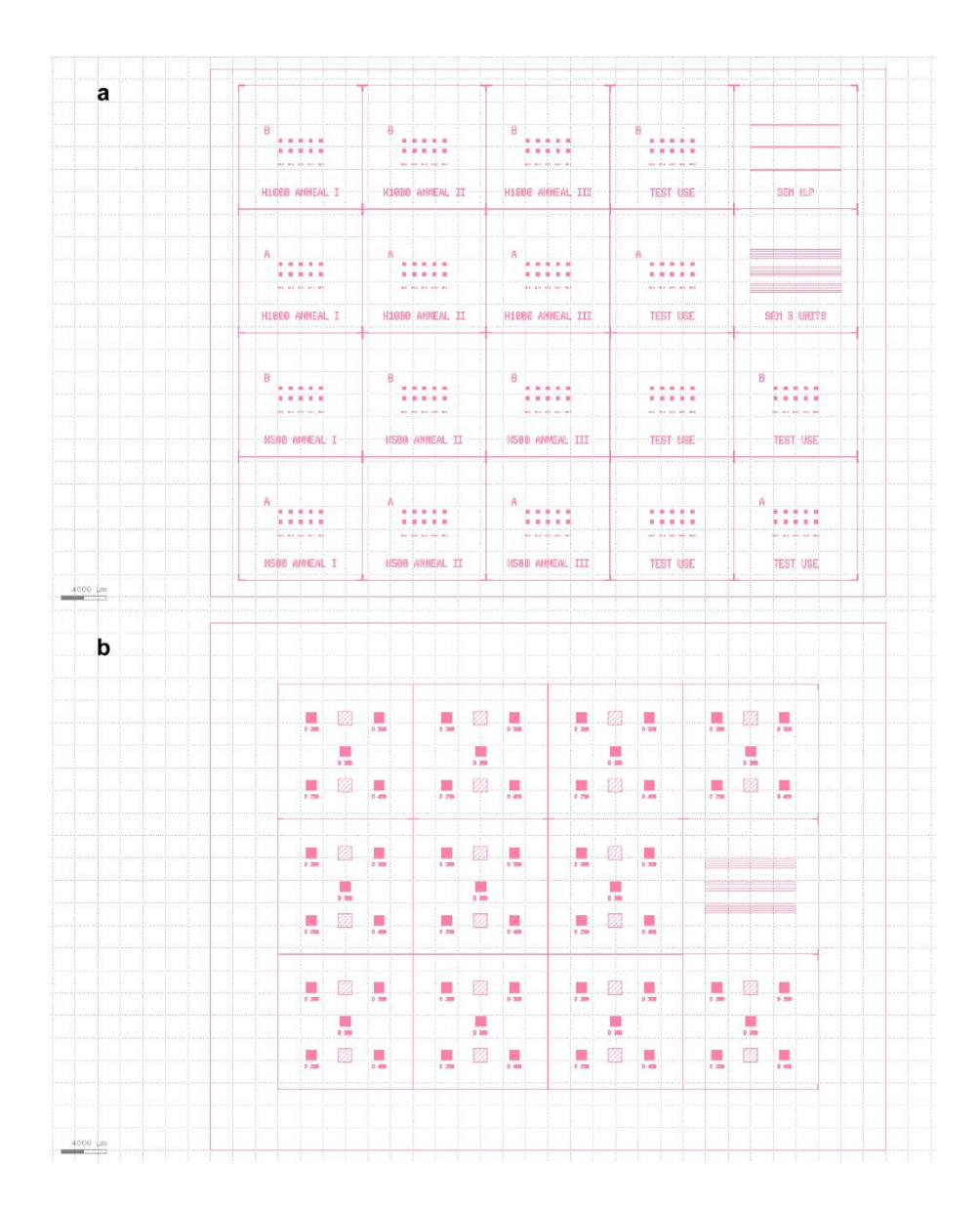


**Fig. 41 Layout of mask design for E-beam lithography.** (a) Original design used to fabricate the experimental sample. The 2-inch chip is divided into 15 small chips, each of which consists of 10 square arraies of VO<sub>2</sub> filling structures with different diameters. Bars are designed on two of them for cross-section view of SEM. (b) Optmized design that reduces the number of arraies. Dummy areas are set to test the etch rate during the patterning process. SET bars are remained.

In Fig. 42(b) and (c), the most obvious manufacturing defect and also a design discrepancy is the bulge near the corners of holes. The reason that may contribute to these high corners: (i) there is a difference between the pressure inside the chamber and that in the holes, which contribute to the formation of cavities during the growth process. (ii) The theoretical growth rate along different directions of ALD is same, so at the corners of these holes, the VO<sub>2</sub> deposition will be faster than average as horizontally grown and vertically grown VO<sub>2</sub> overlap

here. Then the corner will turn to be larger, which in turn affects the gas entering these holes. This may also result in uneven filling with in the holes.

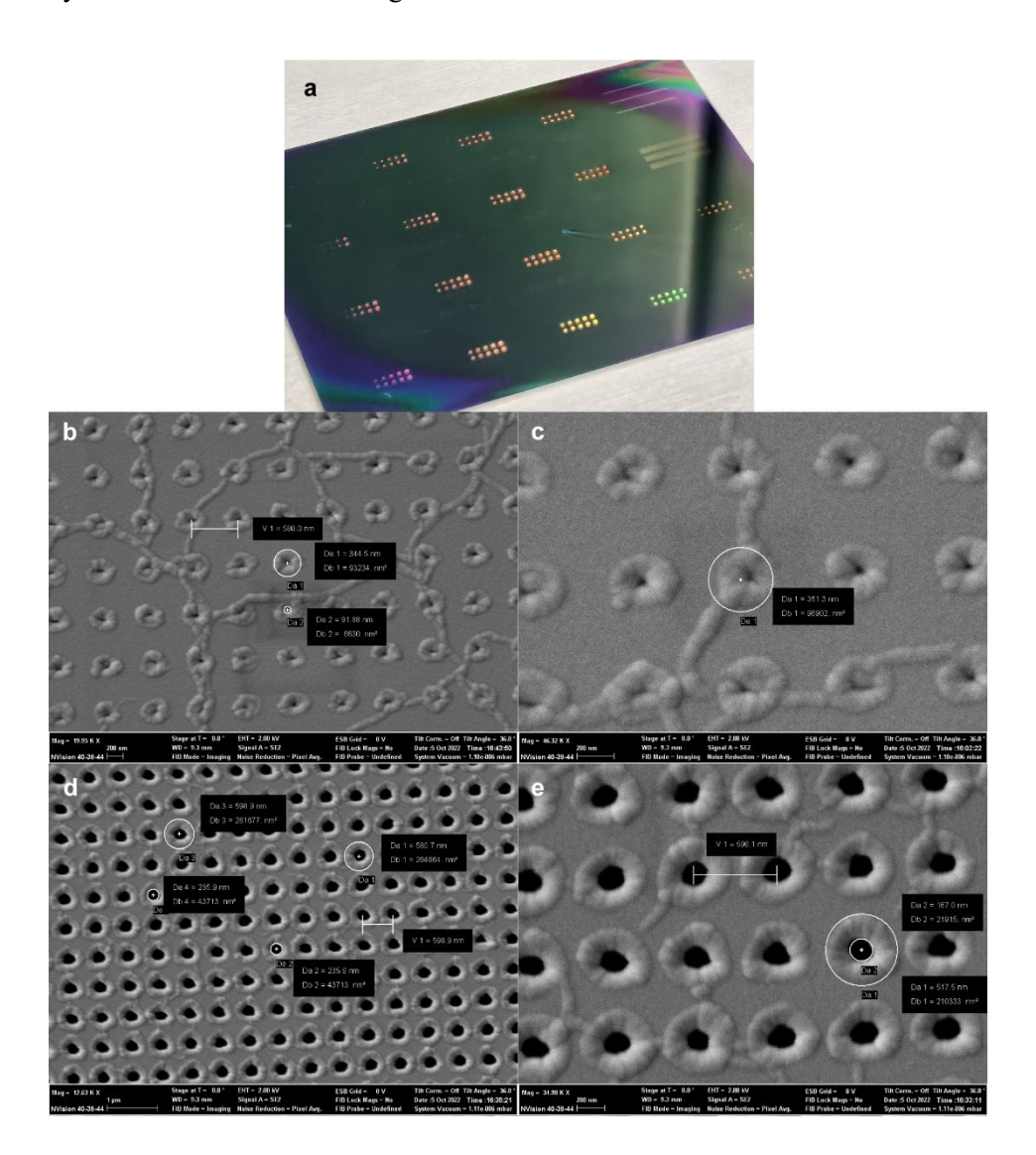


**Fig. 42 Photo and SEM images of the VO<sub>2</sub> filling structure buried in the Si substrate.** (a) The photo shows the overall view of the 2-inch chip. (b) and (c) are the SEM images of the array where the diameter of VO<sub>2</sub> filling is 200 nm at different zoom scales. (d) and (e) are the SEM images of the array where the diameter of VO<sub>2</sub> filling is 400 nm at different zoom scales. The rough measurement of the period, the width of the VO<sub>2</sub> filling (including the overflow area at the edge) and the inner diameter are marked.

It can be observed from Fig. 42 that, unlike the expected situation of using the isotropic growth characteristics of ALD to uniformly coat VO<sub>2</sub> on the sidewall to fill the holes on the Si substrate, the holes in the 200 nm group are basically filled, while those in the 400 nm group are far from being completely filled. To further study the growth of VO<sub>2</sub>, I measured the roughness of the

sample surface using atomic force microscopy (AFM) and plotted the estimated 3D graph of the 200 nm and 400 nm groups as shown in Fig. 43.

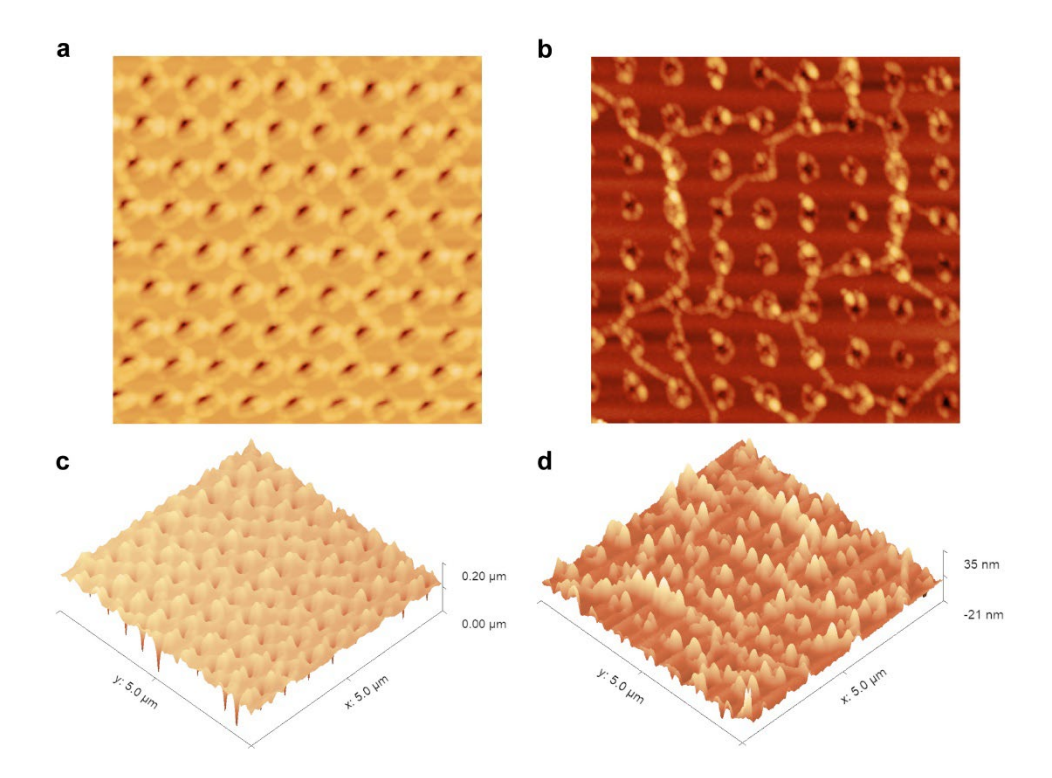


Fig. 43 AFM images of the VO<sub>2</sub> filling structure buried in the Si substrate. (a) The 2D top view of the array where the diameter of VO<sub>2</sub> filling is 200 nm. (b) The 2D top view of the array where the diameter of VO<sub>2</sub> filling is 400 nm. (c) and (d) are the corresponding 3D graphs plotted by measuring the thicknesses of sampling points on the surface. The roughness of the surface can be obtained by analysing the relative height difference between sampling points.

As can be seen from the 2D images, as an imaging tool, the quality of the 2D images generated by AFM is not as clear as that of SEM. However, AFM can be used to roughly estimate the roughness of a surface, benefiting from its working principle of measuring the relative displacement through a probe to calculate thickness. From Fig. 43(c) and Fig. 43(d), the surface roughness of the 400nm group is significantly higher than that of the 200nm group, especially in the raised parts around the holes. Although it is difficult for AFM to accurately measure the voids inside the holes due to the limitation of the probe size, it can still be inferred from the existing results that as the deposition thickness via ALD increases, these holes are not filled as uniformly as expected. Rather, a large error can be observed.

Due to the limited supply of VO<sub>2</sub> precursors and the training schedules for characterisation experiments, this work stopped here. Although no complete results were provided for

publication, this work still provided me with valuable experience in independently completing the fabrication of VO<sub>2</sub> films and can serve as a reference for proposing more promising VO<sub>2</sub>-enabled phase transition devices in the future.

#### 4.3.3. The phase transition of ultra-thin VO<sub>2</sub> films

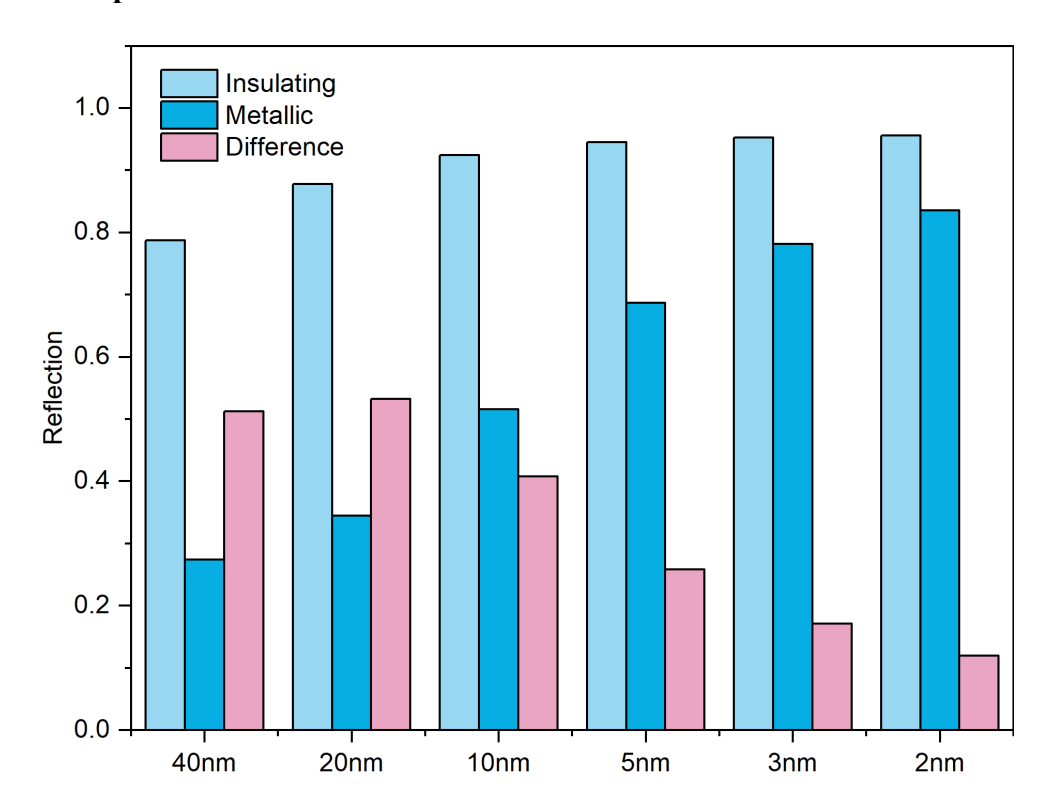


**Fig. 44 Reflection of VO<sub>2</sub> films of different thicknesses.** The VO<sub>2</sub> sample has the same structure as that used in Chapter 2 (VO<sub>2</sub> film grown on SiO<sub>2</sub> of 1225 nm, Al of 100 nm). VO<sub>2</sub> thickness varies from 2 nm to 40 nm. The reflection at the insulating phase and metallic phase are recored, then the difference is calculated to show the contrast (theoretical phase transition feature).

Another application form of VO<sub>2</sub> that has attracted research interest is the phase transition in the ultra-thin state. By molecular beam epitaxy, VO<sub>2</sub> films thinner than 2 nm can be grown, but there is a lack of evidence to support the films still maintaining the phase transition features [208, 209]. Some other literature that uses similar fabrication processes (e.g., use VTOP as precursors) found that 40~50 nm might be the optimal thickness for the trade-off between thickness and obvious IMT characteristics [210]. Besides, through magnetron sputtering, polycrystalline VO<sub>2</sub> films thinner than 10nm can be produced for high-transmittance devices. However, the contrast almost disappears at this thickness [211]. Since ultra-thin VO<sub>2</sub> films may become the key to switchable devices and be used in straight waveguides and ring waveguides, I conducted a series of explorations on the phase transition limit thickness. The main

contribution of this fabrication work is to explore the limitations of the currently used ALD process in growing ultrathin VO<sub>2</sub>, and the possible reasons are briefly discussed.

Fig. 44 shows the simulation results of VO<sub>2</sub> films via COMSOL Multiphysics (the basic settings are same as stated in appendix A), the thickness of which varies from 2 nm to 40 nm. From a theoretical perspective, when the film thickness drops to 20 nm or even 10 nm, there is still a significant contrast between the two pure phases. For 3 nm and 2 nm groups, this contrast is likely to be indistinguishable from experimental errors. For comparison, I fabricated several experimental samples. The ALD conditions are: TEMAV is pre-heated to 85°C, then the reaction is processed at 150 °C. H<sub>2</sub>O is used as the oxidant. The pressure is set to 1 Torr. Five samples of different thicknesses are fabricated, which takes 90 cycles, and 300 cycles. 750 cycles, 900 cycles and 1200 cycles of ALD respectively. The correlative parameters are listed in the table below and the reflection spectra measured by FTIR are shown in Fig. 45. The cycle number of each group and the corresponding thickness of grown VO2 films are listed in Table. 5 below.

**Table. 5 ALD parameters of several VO<sub>2</sub> film samples grown by different cycles.** Ideally, the thickness of the VO<sub>2</sub> film is directly proportional to the number of cycles. However, due to the inability to achieve strict self-limiting growth and the lack of precursors, the thickness may deviate from expectations.

Cycle number	Expected thickness/nm	Measured thickness/nm
90	3	6.23
300	10	13.5
750	20	27.26
900	30	32.99
1200	40	41.47

From Table. 5, the 90-cycle group exhibits a large error in the thickness. There are several possible reasons to result in the error: (i) The chamber used for the ALD process can be loaded with an 8-inch wafer. When smaller chips are placed, the uniformity may change. In general, the thickness of the deposition is larger in the area closer to the air inlet, while the thickness of the deposition at the far end is smaller. (ii) When the precursor supply is short, it will be difficult to accurately estimate the thickness deposited per cycle due to the drop in air pressure.

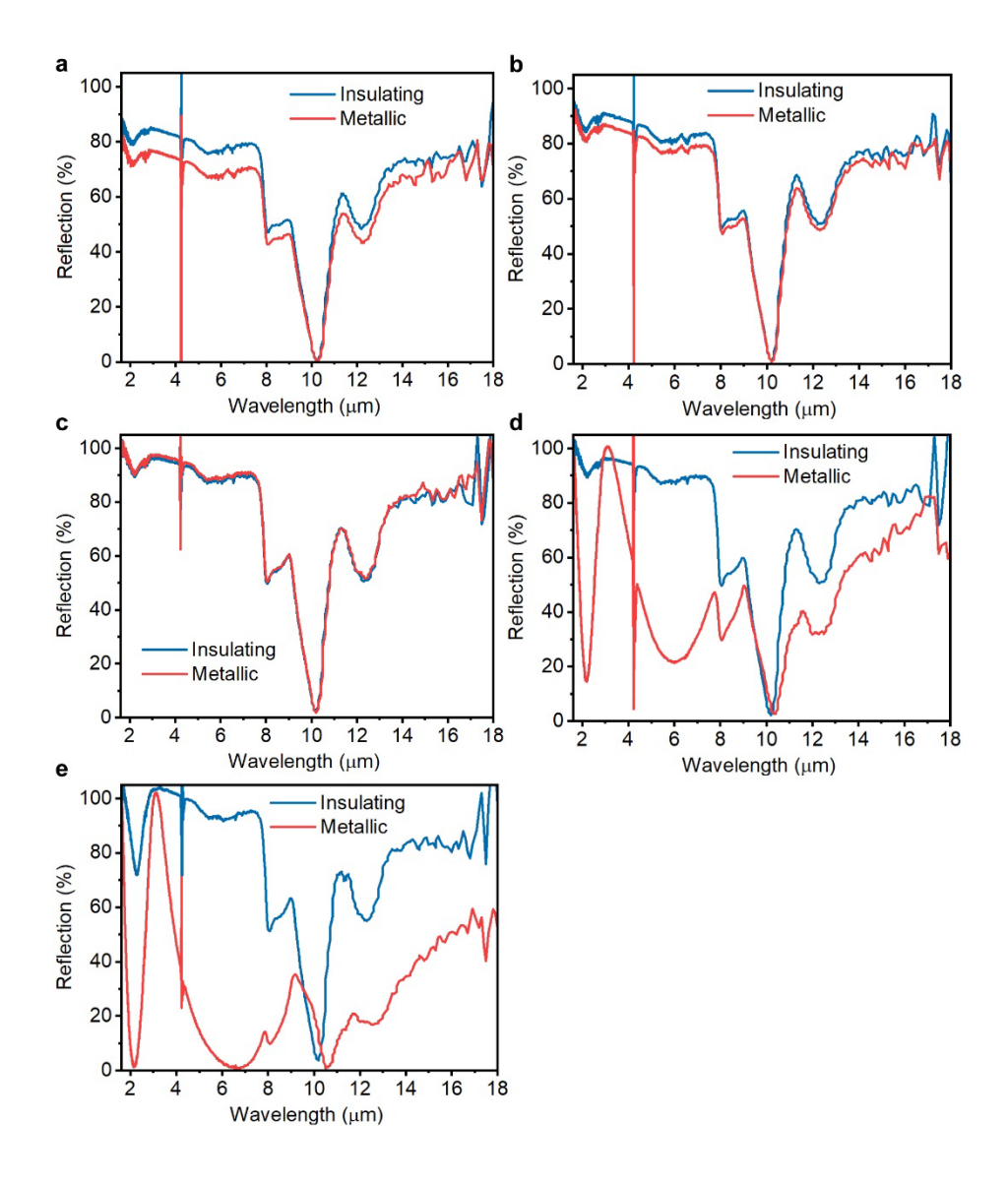


Fig. 45 Reflection spectra across broadband measured on  $VO_2$  samples of different thicknesses. (a) ~ (e) show the reflection spectra measured at the insulating and metallic phases from the  $VO_2$  samples grown by ALD process of 90 cycles, 300 cycles, 750 cycles, 900 cycles and 1200 cycles respectively. The contrast between low-temperature and high-temperature curves reflects the significance of phase transition characteristics.

Fig. 45 shows the reflection spectra across the broadband (1.25  $\mu m$  to 18  $\mu m$ ) measured from VO<sub>2</sub> samples of different thicknesses. The significance of phase transition characteristics can be directly observed through the contrast between the blue low-temperature spectrum and red high-temperature spectrum. For the 90-cycle, 300-cycle, and 750-cycle groups, it can be considered that the phase transition cannot be observed from the change in optical properties (the contrast in the 90-cycle group is uniform across all wavelengths so it can be regarded as the errors). For the 900-cycle and 1200-cycle groups, the contrast between the insulating phase

and metallic phase is obvious. From this measurement, with the same ALD and annealing process I use, in the design of intensity modulation devices (reflective or transmissive devices), the thickness of the functional layer of  $VO_2$  should be at least 30 nm.

# 5. Summary and future work

# 5.1. Summary of my PhD project

My PhD work mainly involves the two topics of vertical growth models (VGM) and the design of tunable metalens, as well as some extensions related to the phase transition of VO<sub>2</sub>. The results are output in forms of theoretical simulation, analytical calculation and experiment.

First, I have proposed a type of new theoretical model, the vertical growth model, and used it to analyse the optical properties of a VO<sub>2</sub> thin film during phase transition. The model views the VO<sub>2</sub> phase transition as a layer-by-layer conversion from one phase into the other, which can emerge from the top and/or the bottom surfaces of the thin film. This VGM has a theoretical assumption that is the opposite of the EMMs, which requires coexisting phases to mix in space to form an effective medium. The VGM is compared against the Bruggeman and the Looyenga models, two EMMS that are commonly used in VO<sub>2</sub> research, in reproducing reflection measured on two VO<sub>2</sub> thin films. Both the VGM and the EMMs well reproduce the reflection across a significant wavelength range in the near-infrared (from 1.4 to 2.0 μm) and a temperature range (from 25.0 to 100.0 °C) that fully covers the phase transition. Based on three different figures of merit that reveal different features of the optical modulation, I find that the VGM provides mostly equivalent, in certain cases slightly better, fitting to the experimental results.

For the EMMs, the results show that they remain useful analytical models. However, because the VGM provides very similar theoretical results, the fundamental theoretical assumption of the EMMs, which states that constituent phases mix in space, could be wrong for some thin film experiments. For the VGM, our results show that it is a new, straightforward analytical model for analysing VO<sub>2</sub> phase transition. It also indicates that the phase transition in ALD-fabricated VO<sub>2</sub> thin films is closer to a layered format. This insight, which needs to be checked against direct, microscopic experimental observations in the future, could benefit a broad range of phase transition-enabled nanophotonics research. In addition to VO<sub>2</sub> discussed here, the VGM could also be utilized for various non-volatile phase transition, volatile phase transition and composite materials, such as GeSbTe (GST) ternary alloys [212].

Throughout my PhD project, this work serves as the basis for exploring the phase transition of VO<sub>2</sub>. In addition to verifying the credibility of the VGM under specific conditions, it also better verifies that the traditional EMM has a relatively reliable prediction performance in the wavelength range I am concerned about (such as 1550 nm), so it can be used for simple

applications such as refractive index derivation. Since the vertical growth models have not been supported by sufficient experimental data in the application field, the widely accepted effective medium models will still be used for calculations involving the physical parameters of  $VO_2$  such as refractive index and complex permittivity in the design of metalens.

Next, I have designed a  $VO_2$ -based tunable metalens and stated the method to select elements and establish the metalens array for simulation. Based on the exploration of the phase transition of  $VO_2$  in my first work, a reflection-mode tunable metalens working at a single wavelength of 1550 nm was proposed. The parameters of the prototype are listed as follows: the diameter of the metalens array is 41  $\mu$ m, with 41 units arranged along a single diameter. The basic structure of the meta-atom is a double-layer pillar formed by a 180 nm  $VO_2$  layer (bottom) and a 280 nm Si layer (top), which is grown on a Si substrate. The side lengths of the nanopillar are variables that to contribute different reflection phase values, the sweeping range of which is 100 nm to 800 nm. As the target function of this metalens, the designed focal length to implement binary tuning is 40  $\mu$ m when  $VO_2$  works in the insulating phase, while it changes to 30  $\mu$ m when  $VO_2$  works in the metallic phase. I adopt the refractive indices of two pure phases extracted from the experimental sample. The phase transition is implemented by using Looyenga's model to fit the refractive indices of corresponding phases.

Through FDTD simulation on Lumerical, the binary focus tuning is achieved by outputting the electric field intensity distribution as shown in section 4.2.3. The focal length of simulated metalens at the insulating phase is 39.27 µm (designed value is 40 µm), and it decreases to 30 µm (designed value is 30 µm) at the metallic phase. After realizing binary focus tuning, I took 9 intermediate states (a total of 11 points) by changing the value of filling factor *f* and calculated the focal length of the metalens at the corresponding states. This metalens is found to be continuously tunable as the focal length exhibits a continuous change during the phase transition. Since the phase transition characteristics of the single units that make up the metalens do not show regularity, I have not been able to complete a theoretical explanation of the continuously tunable characteristics of the metalens. The main contribution of this work so far is to provide an efficient solution to the metalens design, including a complete process from determining the unit structure and screening component meta-atoms to assembling the metalens for simulation to predict its performance.

In addition to these two pieces of works that have been published in some conferences, I also make attempts to research on some topics that are highly related to the fabrication. My main contribution in these separate works is to broaden the understanding of VO<sub>2</sub> properties and phase transitions by fully operating the fabrication of VO<sub>2</sub> thin films (ultrathin films stated in

section 4.3.3) or devices (VO<sub>2</sub> fillings in section 4.3.2) starting from Si or SOI wafers in the following aspects: (i) by exploring the possibility of constrained phase transition of VO<sub>2</sub>, the limitations and structural optimisation of high-aspect-ratio VO<sub>2</sub> devices are discussed. (ii) By observing the phase transition of VO<sub>2</sub> at films thinner to 2 nm via both numerical simulation and experiments, I discover the difficulty of growing ultra-thin VO<sub>2</sub> films based on current ALD process, and the attenuation of phase transition (contrast) as the film thickness decrease, which may be a key factor in limiting VO<sub>2</sub> application in nanophotonics.

In summary, I have made certain progress in the topic of possible applications of VO<sub>2</sub> phase transition, both in the unpopular and challenging theoretical aspects (VGM used to describe and predict the phase transition behaviour) and in the design of devices (metalens) with higher application value.

#### 5.2. Future work

In addition to the the work that have been discussed in chapter 4 in detail, I have also tried several other directions, all within the scope of VO<sub>2</sub>-based nanophotonic devices. Some preliminary results have been obtained, and they are described in the appendix. In my view, the most promising direction is combining the VO<sub>2</sub> phase transition with the emerging concept of photonic bound states in the continuum (BIC) [213, 214]. The concept of BIC originates from quantum mechanics, and it has become a hot topic in photonics research recently. It describes a unique type of resonance that is protected from external excitation. It is a mathematical concept, and practically only the quasi-BIC (qBIC) mode can be observed in the experiment. Below I describe qBIC briefly and provide some preliminary analysis in the Appendix E.

Fig. 46 shows a typical qBIC dielectric metasurfaces [215]. Its meta-atoms are identical Si pillars with different orientation angles. A BIC resonance exhibits characteristics such as zero line width and infinite quality factor Q. Ideal BIC has never been observed in experiments due to the energy loss and manufacturing defects. Instead, the concept of qBIC is proposed and widely studied. It creates ultrahigh Q-factor resonances by breaking the symmetry of the periodic structure and converting the symmetry-protected BIC into Fano resonance modes [216, 217]. A method to implement qBIC is to create asymmetry in Mie resonance units, and Fig. 46 shows two different types of element design used in qBIC systems. By reconfiguring the metasurfaces with different tilt and source modes, red and blue shifts are observed, which exhibits the high flexibility of this qBIC system in the design of imaging and spectroscopy devices.

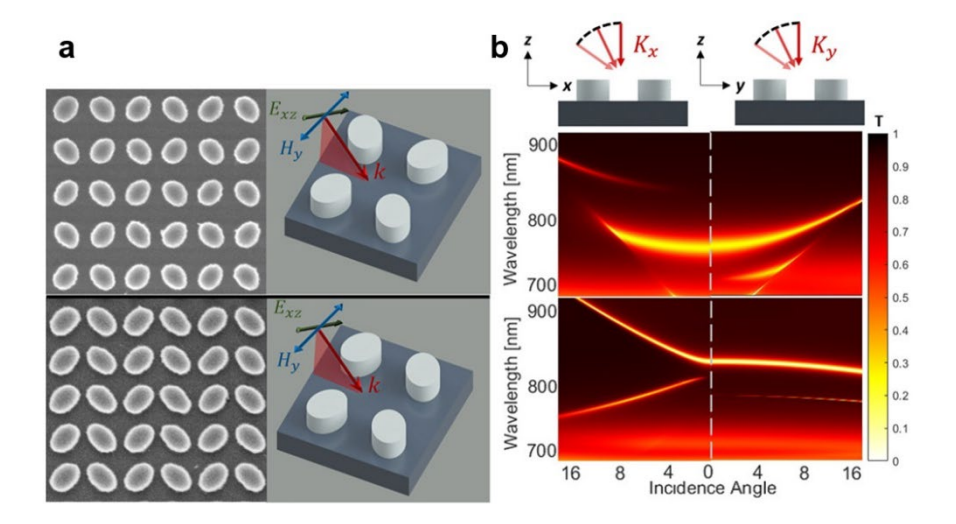


Fig. 46 High-index dielectric Quasi-BIC metasurfaces. (a) shows the schematics and the corresponding SEM images of two different basic unit designs, which have symmetry in both x and y directions and only in the y direction, respectively. (b) illustrates the cross-section view of them to clarify the polarization direction, and the corresponding transmission maps. The transmission is measured for different wavelengths and incident angles, which exhibits the absorption traces that result from resonance at the specific wavelength and incident angle. The figures (a) and (b) are copied from [215].

This category of metasurfaces introduces a new variable, which is symmetry-breaking achieved by different tilt angles of units. I have conducted some preliminary analysis on VO<sub>2</sub>-based qBIC metasurfaces and the results can be found in Appendix E. These limited results already indicate that VO<sub>2</sub>-based qBIC metasurfaces can become a promising new research direction.

# **Appendix**

### A. Simulation settings of COMSOL

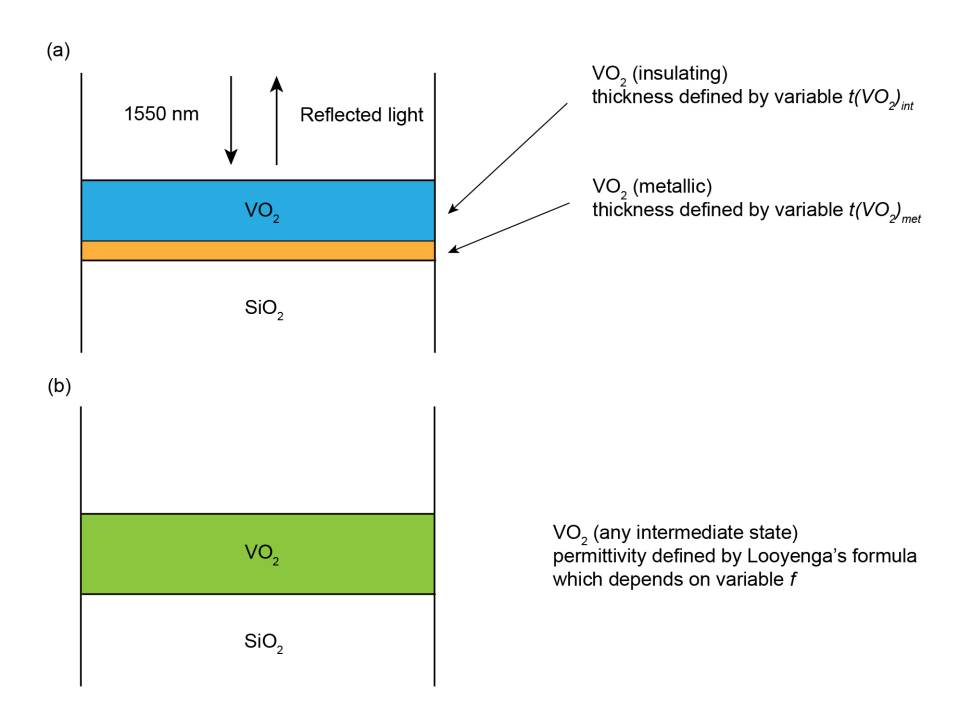


Fig. A1 Schematic of COMSOL modelling to implement VGM. (a) For vertical growth models, the variable swept is the thickness of metallic  $VO_2$  and insulating  $VO_2$ , which corresponds to a change in volume fraction. (b) For effective medium models, any intermediate state can be defined as a single material with tunable optical properties. The variable swept is the filling factor f that can determine the value of permittivity and refractive index.

As shown in Fig. A1, the simulation of EMM is implemented by continuously changing the variable of volume fraction factor f in the definition formula, while the case of VGM is much more complicated. Two uniform layers (three for type AS VGM) are set to represent insulating and metallic VO<sub>2</sub>. During the parametric sweep, the thickness of these layers varies to simulate the growth of metallic VO<sub>2</sub> in the mixture. The 2D structure is set to extend infinitely along the y-direction (perpendicular to the direction of the schematic diagram), while it repeats at a periodicity of 400 nm along the x-direction. The input light is a normal incident light from the top surface of the air, and the monitor to measure reflection is set on the same side. Perfectly matched layers are placed at both the upper boundary and bottom boundary. Only a single wavelength of 1550 nm is used for simulation.

As Fig. A1 shows, when defining the parameters, for any specific vertical growth models, the incident wavelength and the material properties corresponding to each wavelength (the dielectric constant that varies with the wavelength) are the only parameters that can be manually adjusted, and the thickness of metallic-state VO<sub>2</sub> occupied in the entire VO<sub>2</sub> layer is the only dynamically changing variable in the parametric sweep. Attention should be paid to the design of the simulation model. When the thickness of the VO<sub>2</sub> layer after phase transition is very small or very large (that is, the thickness of the insulating VO<sub>2</sub> layer is very small), the mesh density and accuracy of the 2D model will directly affect the accuracy of the simulation results, so compared with the EMT model, the simulation of the vertical growth model requires more resources. In this report, the minimum step of parametric sweep on thickness is 0.5 nm, which is equivalent to a change of 1.25% in volume fraction order, the two sets of models can still be placed in the same graphs for direct comparison.

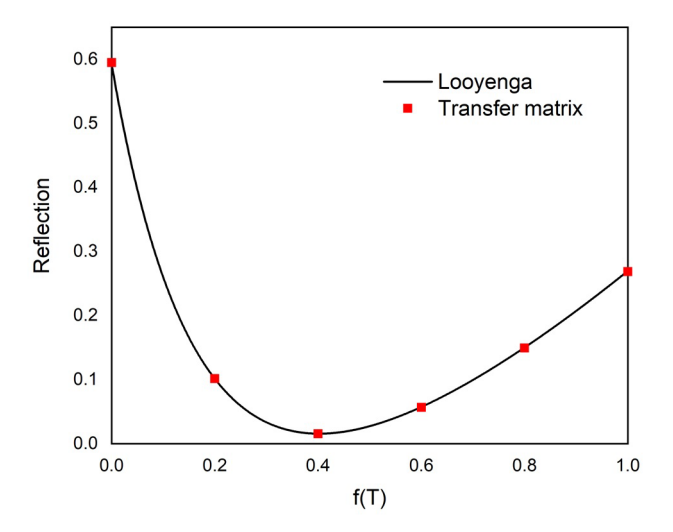
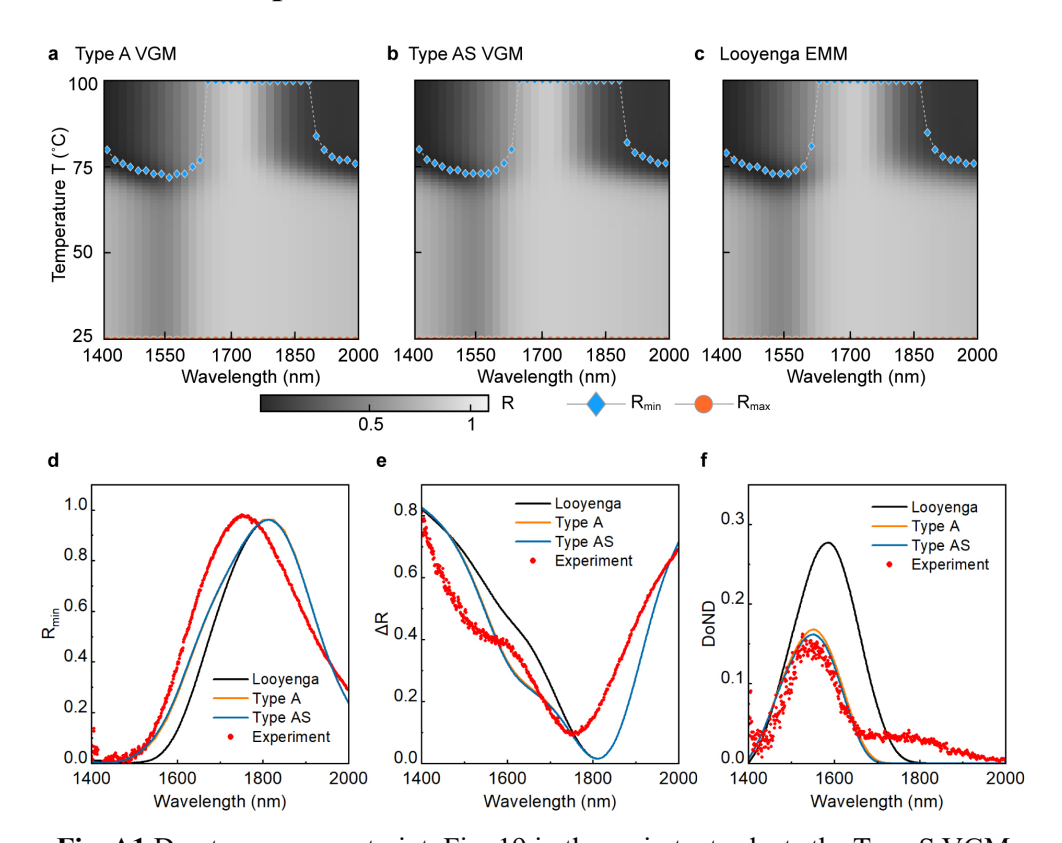


Fig. A2 Verification of simulation model by comparing reflection at six mixing states produced by Looyenga's model and transfer matrix method. The wavelength selected for calculation is 1550 nm.

Fig. A2 exhibits the verification results of Looyenga's model calculated by the transfer matrix method and COMSOL simulation. 6 points of reflection calculated by MATLAB are plotted to compare with the curve produced by COMSOL. It can be considered that results calculated by both the transfer matrix method and COMSOL simulation are reliable.

#### B. Quantified comparison between different models



**Fig. A1** Due to space constraint, Fig. 19 in the main text selects the Type S VGM and the Bruggeman EMM to compare with the experimental results. Here, the other two variants of the VGM (i.e., the Types A and AS) and the other EMM (i.e., the Looyenga model) are provided to complete the comparison. The maps of (a) Type A, (b) Type AS, and (c) Looyenga model are first produced, from which we extract the curves of (d)  $R_{\min}$ , (e)  $\Delta R$ , and (f) DoND. The results of Types A and AS are very close to Type S, and those of the Looyenga EMM are very close to the Bruggeman EMM. The conclusion that we draw in the main text is consequently further confirmed here, which states that the VGM and the EMMs provide a similar level of accuracy in the theoretical prediction, while the former slightly outperforms the latter in some cases [most visible in panel (f), the DoND]. the change in volume fraction. (b) For effective medium models, any intermediate state can be defined as a single material with tunable optical properties. The variable swept is the filling factor f that can determine the value of permittivity and refractive index.

Fig. 29 in section 4.1.6 illustrates the results of quantified comparison among experimental results, type S VGM and Bruggeman model. Colour maps to show the temperature-dependent change of reflection over different wavelengths from 1.4  $\mu$ m to 2.0  $\mu$ m are produced for direct

comparison. Then, three figures of merit (i.e.,  $R_{min}$ ,  $\Delta R$  and DoND) are introduced to compare VGM and EMM in their prediction of phase transition behaviour that happens in the practical VO<sub>2</sub> sample.

Besides the type S VGM and Bruggeman model that are detailed in the main text, there are some other theoretical models that I do simulation on. As the results show high similarity to other forms of these models, I list the results of these models here as shown in Fig. B1. For comparison, experimental results are plotted in Fig. B1 (d)  $\sim$  (f). As type A VGM and type AS VGM exhibit almost the same results as type S VGM, and the Looyenga model also shows high consistency with the Bruggeman model, there is no new conclusion to be drawn. I think the main reason that I didn't find enough distinction between three types of VGM is the model is too simple with less degrees of freedom. It's just a very primary attempt to introduce geometric parameters to phase transition analysis. For example, if I define a curved interface or roughness coefficient, it's likely to see larger difference, but it should be what further research focus on.

#### C. Parameters of representative elements in the metalens array

**Table. C1 Dimensions and output phase of elements along** x **direction.** 21 elements are arranged along the radius of metalens. As the metalens is symmetric along both x and y directions, here I list the parameters of elements located on the radius along the x direction, including the side lengths a and b, output phase at the insulating and metallic phases.

Side length a/nm	Side length b/nm	$\varphi_{ins}$	$arphi_{met}$
480	600	2.12	6.21
475	600	2.23	6.27
460	605	2.27	0.20
430	620	2.53	0.53
395	635	2.87	0.90
410	620	3.33	0.77
100	115	4.05	0.75
765	480	4.59	5.07
795	495	5.39	4.87
785	490	6.15	4.94
580	765	0.81	0.21
170	730	1.85	1.94
100	135	2.37	2.38
	480 475 460 430 395 410 100 765 795 785 580 170	480 600 475 600 460 605 430 620 395 635 410 620 100 115 765 480 795 495 785 490 580 765 170 730	480       600       2.12         475       600       2.23         460       605       2.27         430       620       2.53         395       635       2.87         410       620       3.33         100       115       4.05         765       480       4.59         795       495       5.39         785       490       6.15         580       765       0.81         170       730       1.85

13	755	495	4.19	4.99
14	735	220	5.47	6.25
15	395	305	0.57	1.49
16	635	570	1.55	3.64
17	610	515	3.58	5.56
18	395	625	5.26	0.92
19	760	555	1.33	3.40
20	530	575	2.37	5.59

**Table. C2 Dimensions and output phase of elements along the diagonal.** 21 elements are arranged along the radius of metalens. As the metalens is symmetric along both x and y directions, here I list the parameters of elements located on the diagonal that is 45 degrees to both x and y axes, including the side lengths a and b, output phase at the insulating and metallic phases.

Element number	Side length a/nm	Side length b/nm	$arphi_{ins}$	$arphi_{met}$
0 (centre)	480	600	2.12	6.21
1	470	600	2.31	0.05
2	440	610	2.56	0.45
3	390	640	3.04	0.95
4	405	625	3.71	0.81
5	770	490	4.76	4.98
6	795	485	5.74	4.95
7	625	735	0.72	0.09
8	100	550	2.20	2.21
9	735	500	3.82	5.01
10	685	220	5.68	0.20
11	540	600	1.36	2.79
12	630	510	3.55	5.46
13	390	605	5.91	0.99
14	540	580	2.03	5.21
15	395	630	4.80	0.89
16	505	605	1.50	5.64
17	415	610	4.05	0.75

18	600	780	0.75	0.11
19	750	495	3.96	5.00
20	755	580	0.86	1.48

Since the circular metalens has significant symmetry properties, and its array is axially symmetrical along the x and y axes, I established a matrix with a 1/4 circle to fill in the corresponding elements during unit screening to reduce the computational load. Here I list the dimensional parameters (side lengths a and b) and the output phase at the insulating phase and metallic phase of two groups of elements. Table. C1 shows the elements along the x direction and Table. C2 shows the elements placed on the diagonal. These representative elements occupy a large proportion of the units to form the entire metalens array.

#### D. Element optimisation by using different forms of VO<sub>2</sub> coating

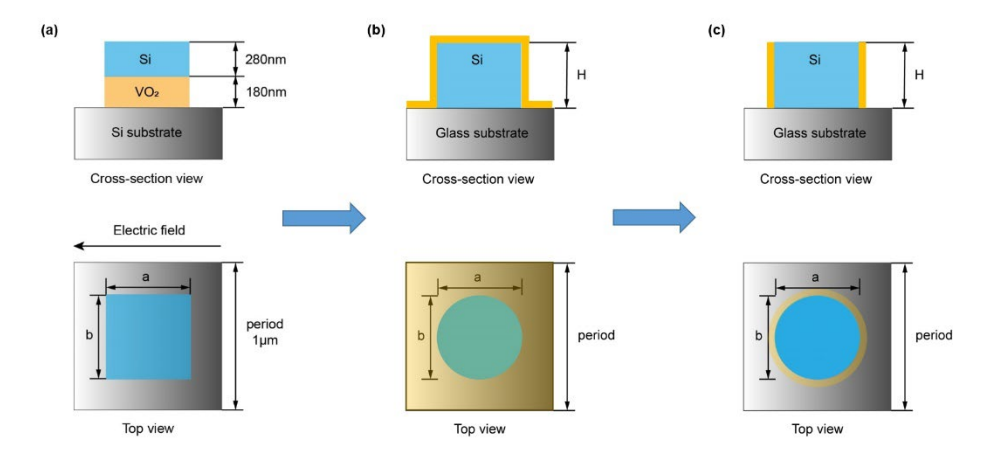


Fig. D1 Several meta-atom designs based on different types of VO<sub>2</sub> coating. (a)

The original design used in Chapter 3. The planar dimensions of the meta-atom is 1 μm by 1 μm. It contains a nanopillar that has a Si segment on top of a VO<sub>2</sub> segment. The thickness of the Si segment and the VO<sub>2</sub> segment is 280 nm and 180 nm, respectively. The planar dimensions *a* and *b* of the pillar serve as tunable parameters. (b) The first new design that deposits a VO<sub>2</sub> thin film on the Si pillar with a glass substrate. The Si pillar is an elliptical cylinder, the long axis and short axis of which are the variables for parametric sweep. (c) The second new design based on the structure shown in (b). By using precise etching technique, the top surface of VO<sub>2</sub> film can be removed, the rest part works as a ring-shape shell at the outer side of the Si pillar.

After binary focus tuning is implemented as stated in section 4.2.3, I attempted to optimise the metalens design from the perspective of the element library. There are three main factors for why I modified the design: (i) Compared with reflective metalenses, the transmissive type has broader application prospects. However, since the full  $2\pi$  phase coverage is more difficult to achieve on transmissive metalenses, it puts higher requirements on the element library. (ii) Though the metalens stated in the second work were designed based on Mie scattering, it is difficult to exclude the influence of the propagation phase due to the geometric dimensions of the unit elements. The use of  $VO_2$  thin films or shells can effectively reduce the overall width of the units and thus increase the aspect ratio, making the resonance characteristics easier to control. (iii) In this thesis, all designs involving  $VO_2$  growth are based on ALD, which is a slow and expensive deposition process. A  $VO_2$  layer of 180 nm is not cost-effective, while the design shown in Fig. D1 (b) and (c) can significantly reduce the cost.

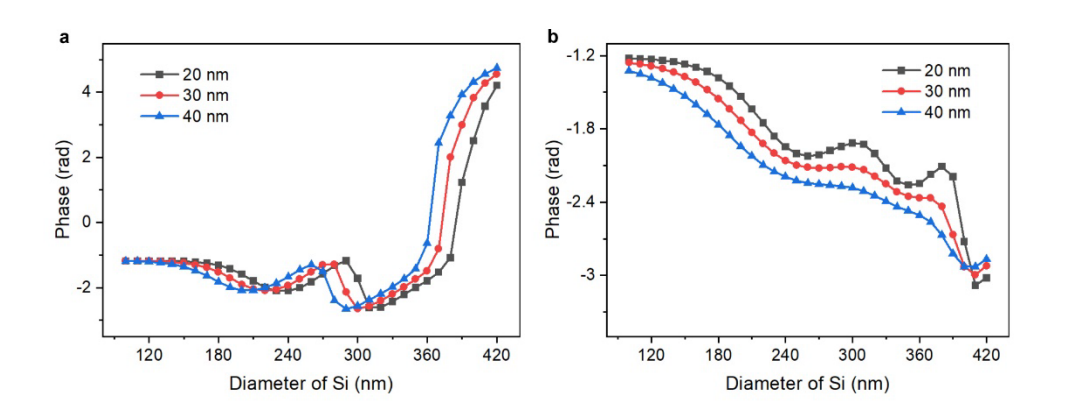
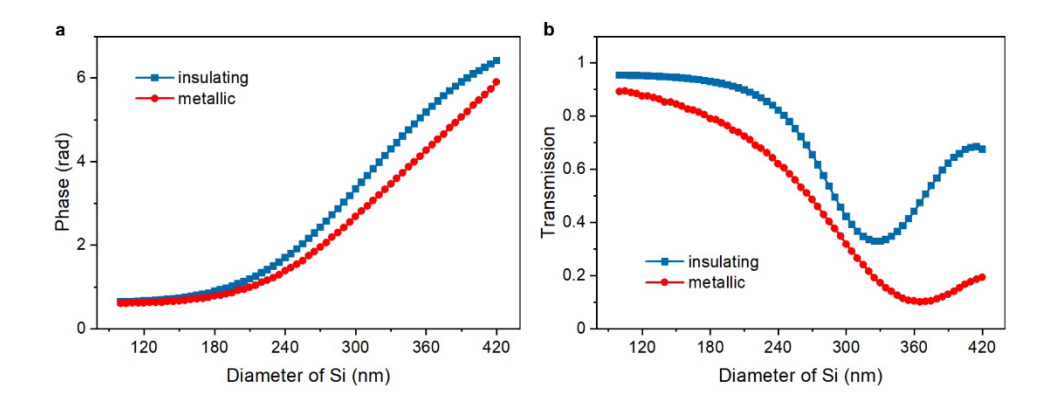


Fig. D2 Phase graphs of parametric sweep on diameter of VO<sub>2</sub>-coated Si pillars.

The structural design is shown in Fig. D1 (b). The diameter of Si pillar is set as the variable to sweep. (a) and (b) show the phase output at the insulating and metallic phases respectively. VO<sub>2</sub> films of three different thicknesses (20 nm, 30 nm, 40 nm) are used to explore the influence of VO<sub>2</sub> thickness on the phase coverage of this element design. The wavelength of incident light is 1550 nm.

The simulation of the new structure [Fig. D1(b)] starts with the simplest cylindrical structure, i.e., the case where the axis lengths a and b are equal. The height of the Si pillar is 800 nm, and the period of the unit element is set to 650 nm. The diameter of the Si cylinder varies from 100 nm to 420 nm by a step of 10 nm. To discuss the sensitivity of this structure to the thickness of VO<sub>2</sub>, three different thicknesses are simulated as shown in Fig. D2. From the graphs when the VO<sub>2</sub> coating works at the insulating phase, all three groups contribute to a  $2\pi$  phase coverage with slight difference between each other. However, the phase coverage exhibits a rapid decrease at the metallic phase. By comparing the new structure with the element that I used in

my second work, the phase coverage doesn't satisfy the requirements of the metalens design yet. From the perspective of resonance characteristics, it is speculated that the VO<sub>2</sub> coating affects the Mie scattering. This conjecture can be further supported by the fact that VO<sub>2</sub> with different thicknesses has little effect on the phase distribution results. With the support of precisely controlled etching technology, the VO<sub>2</sub> coating on the top surface and the substrate can be removed, then the rest part works like a ring-shaped shell coated on the sidewall of the Si pillar. Through several rounds of parametric sweep, the simulation results are shown in Fig. D3.



**Fig. D3** Phase and transmission graphs of parametric sweep on diameter of VO<sub>2</sub>-coated Si pillars. The structural design is shown in Fig. D1 (c). The diameter of Si pillar is set as the variable to sweep. (a) shows the phase output at both the insulating (blue dots and line) and metallic (red dots and line) phases. (b) shows the corresponding transmission intensity. The period of the element is 650 nm. The height of the Si pillar is 600 nm. The thickness of VO<sub>2</sub> shell is 20 nm, while the height is 550 nm (50 nm corner etching applied). An Al<sub>2</sub>O<sub>3</sub> isolation layer of 10 nm is deposited between VO<sub>2</sub> and Si. The wavelength of incident light is 1550 nm.

The structure used for simulation to produce Fig. D3 is significantly different from that of Fig. D2. (i) The dimensions are modified. The height of Si is reduced to 600 nm, and the thickness of VO<sub>2</sub> is set to 20 nm to reduce the cost. (ii) An Al<sub>2</sub>O<sub>3</sub> layer of 10 nm is deposited on the Si pillar before coating the VO<sub>2</sub> shell. The material of Al<sub>2</sub>O<sub>3</sub> has a refractive index similar to that of glass. By isolating the VO<sub>2</sub> and the Si pillar, the phase coverage of this element design might be effectively extended. (iii) The VO<sub>2</sub> shell is designed to be lower than the Si pillar, for the same reason as stated in the second point. The difference between VO<sub>2</sub> and Si can be implemented by an etching process with extremely high anisotropy (in our cleanroom, the angle of etched sidewalls to the horizontal plane can reach 80 degrees or more).

Fig. D3 shows a group of phase and transmission data simulated from a representative element model. Other models differ in the dimensional parameters and contribute to similar results, which are not detailed here. By using the new  $VO_2$  structure (thin shell), at both the insulating phase and metallic phase a  $2\pi$  phase coverage is achieved. However, the phase contrast is far from the standards for the design of tunable devices [Fig. D3(a)]. Different from the phase distribution, Fig. D3(b) exhibits the change in transmission intensity at two pure phases. The contrast in transmission is significant, the maximum difference of which reaches 50%. At the same time, the minimum transmittance approaches 10% when  $VO_2$  works at a high temperature. This provides great possibilities for designing switchable intensity modulation devices that work at specific wavelengths and demonstrates the potential of  $VO_2$  thin films or thin-film-like devices in manufacturing full absorbers and other tuneable devices.

#### E. Mie-resonance tunable metasurfaces based on VO<sub>2</sub>

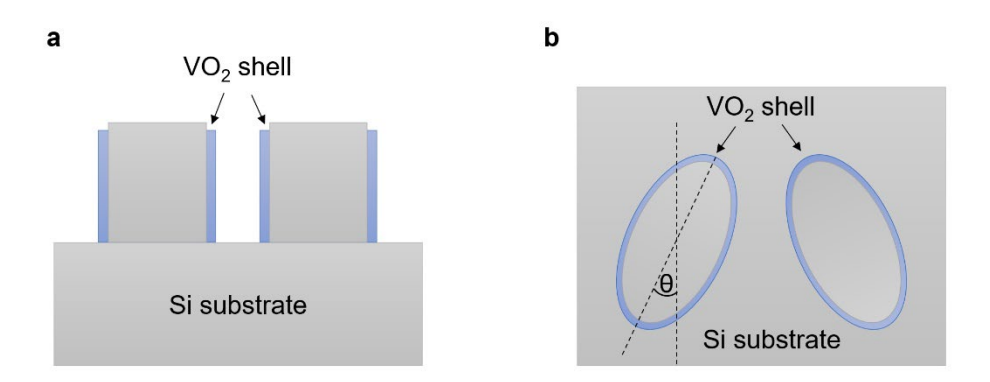
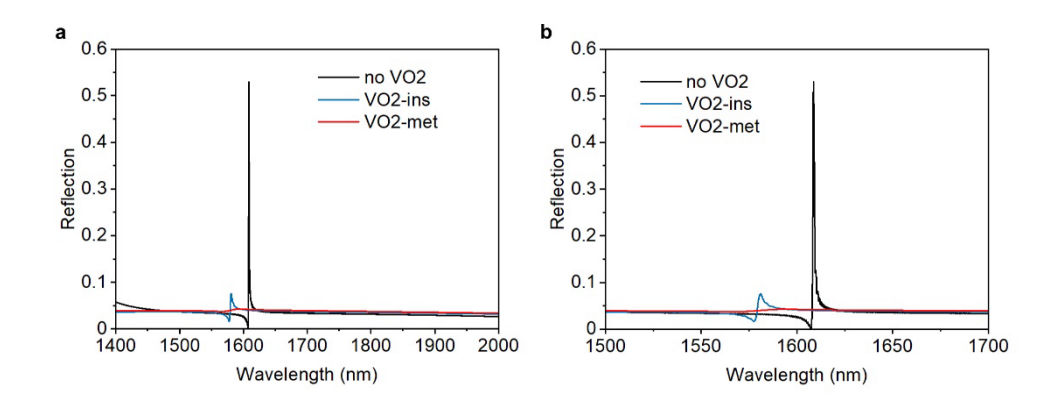


Fig. E1 Schematic of the meta-atom of the VO<sub>2</sub> shell-based tunable metasurface.

(a) The cross-section view. A thin VO<sub>2</sub> shell is coated on the outer side of the Si pillar. The height of VO<sub>2</sub> shell is slightly lower than that of the Si pillar by using precisely controlled etching process. (b) The top view. Two Si pillars are symmetric with the same rotation angle  $\theta$ . The period of the structure is 894 nm along x direction and 515 nm along y direction. The height of the Si pillar is 175 nm.

As stated in the future work section, I made a series of attempts at the design of q-BIC-like systems based on the phase transition of VO<sub>2</sub>. Different from common reconfigurable metasurfaces, the phase transition characteristics of VO<sub>2</sub> can be used to adjust the frequency response characteristics, such as the reflected and transmitted intensity, without changing the component structure. The basic design of the element is shown in Fig. E1. The fundamental structure is determined based on the design from [218].

The axis lengths of the elliptical cylinders are 445 nm and 216 nm, respectively. The height of the Si pillar and the period of repeated units are stated above. The original design works as a q-BIC nanoparticle trapping system. By setting the rotation angle  $\theta = 5^{\circ}$ , the metasurface produces a reflection spectrum with a peak at a certain wavelength domain. My design is to coat an ultra-thin VO<sub>2</sub> film (20 nm) on this Si-based structure and then process the VO<sub>2</sub> into a ring-shaped shell by an etching process that is detailed in section 4.3.1, which is shown in Fig. 39. Due to the intervention of VO<sub>2</sub>, the resonance characteristics of the structure are affected. The reflection spectrum under the same conditions is shown in Fig. E2 below.



**Fig. E2 Comparison of reflection spectra across 1.4 μm to 2.0 μm.** (a) The overall view of the spectra output by the Si-based element,  $VO_2$ -coated element at the insulating phase and the metallic phase. The peak reflection intensity of the Si-based group is around 55%. (b) The zoom view with a scale from 1.5 μm to 1.7 μm, which focuses on the peak.

When the rotation angle  $\theta$  is set to 5 degrees, the reflection peak of the original design (Sibased) reaches about 55%. The VO<sub>2</sub> group also produces a peak in the adjacent wavelength region (when it operates in the insulating phase), but its absolute value is much smaller than the result of the Si group, which is around 8%. Then I kept the basic structure unchanged and coated a 20 nm VO<sub>2</sub> ring-shaped shell on the outside of the Si pillar. Next, I did a series of parametric sweeps based on the rotation angle  $\theta$ , and obtained a group of data with ideal absolute reflection intensity and contrast between two pure phases, as shown in Fig. E3 below.

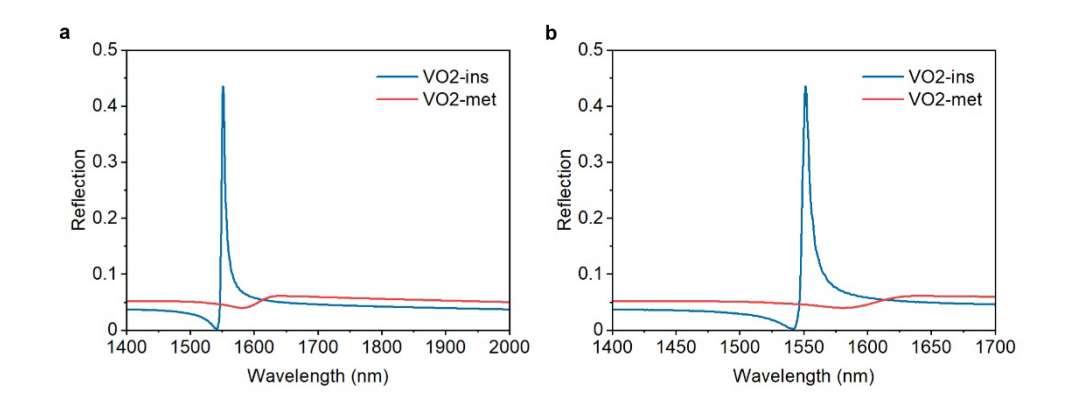


Fig. E3 Comparison of reflection spectra across 1.4  $\mu$ m to 2.0  $\mu$ m (VO2 groups only). (a) The overall view of the spectra output by the VO<sub>2</sub>-coated element at the insulating phase and the metallic phase respectively. The peak reflection intensity of the insulating phase simulation is around 44%. (b) The zoom view with a scale from 1.4  $\mu$ m to 1.7  $\mu$ m, which focuses on the peak.

## **List of References**

- 1. Liu, Y. and X. Zhang, *Metamaterials: a new frontier of science and technology*. Chemical Society Reviews, 2011. **40**(5): p. 2494-2507.
- 2. Belov, P.A., C.R. Simovski, and S.A. Tretyakov, *Two-dimensional electromagnetic crystals formed by reactively loaded wires*. Physical Review E, 2002. **66**(3): p. 036610.
- 3. Choy, T.C., *Effective Medium Theory: Principles and Applications*. 2016: Oxford Science Publications.
- 4. Markel, V.A., *Introduction to the Maxwell Garnett approximation: tutorial.* Journal of the Optical Society of America a-Optics Image Science and Vision, 2016. **33**(7): p. 1244-1256.
- 5. Liu, K., et al., *Recent progresses on physics and applications of vanadium dioxide*. Materials Today, 2018. **21**(8): p. 875-896.
- 6. Hu, P., et al., *Vanadium Oxide: Phase Diagrams, Structures, Synthesis, and Applications.* Chemical Reviews, 2023. **123**(8): p. 4353-4415.
- 7. Lee, S., et al., *Anomalously low electronic thermal conductivity in metallic vanadium dioxide.* Science, 2017. **355**(6323): p. 371-374.
- 8. Shao, Z.W., et al., Recent progress in the phase-transition mechanism and modulation of vanadium dioxide materials. NPG Asia Materials, 2018. **10**: p. 581-605.
- 9. Vu, T.D., et al., *Durable vanadium dioxide with 33-year service life for smart windows applications*. Materials Today Energy, 2022. **26**: p. 100978.
- 10. Takeya, H., et al., *Bolometric photodetection using plasmon-assisted resistivity change in vanadium dioxide*. Scientific Reports, 2018. **8**: p. 12764.
- 11. Wang, T., et al., Maximizing the performance of photothermal actuators by combining smart materials with supplementary advantages. Science Advances, 2017. **3**(4): p. e1602697.
- 12. Deng, S.B., et al., Selective area doping for Mott neuromorphic electronics. Science Advances, 2023. 9(11): p. eade4838.
- 13. Qazilbash, M.M., et al., *Mott transition in VO2 revealed by infrared spectroscopy and nano-imaging*. Science, 2007. **318**(5857): p. 1750-1753.
- 14. Xu, Z.Q., et al., Spatially Resolved Dynamically Reconfigurable Multilevel Control of Thermal Emission. Laser & Photonics Reviews, 2020. 14(1): p. 1900162.
- 15. Voshchinnikov, N.V., G. Videen, and T. Henning, *Effective medium theories for irregular fluffy structures: aggregation of small particles*. Applied Optics, 2007. **46**(19): p. 4065-4072.
- 16. Tuhkala, M., J. Juuti, and H. Jantunen, *Method to characterize dielectric properties of powdery substances*. Journal of Applied Physics, 2013. **114**(1): p. 014108.
- 17. Leahu, G., et al., Anomalous optical switching and thermal hysteresis during semiconductor-metal phase transition of VO2 films on Si substrate. Applied Physics Letters, 2013. **103**(23): p. 231114.
- 18. Currie, M., M.A. Mastro, and V.D. Wheeler, *Characterizing the tunable refractive index of vanadium dioxide*. Optical Materials Express, 2017. **7**(5): p. 1697-1707.
- 19. Frame, J.D., N.G. Green, and X. Fang, Modified Maxwell Garnett model for hysteresis

- in phase change materials. Optical Materials Express, 2018. 8(7): p. 1988-1996.
- 20. Choi, H.S., et al., *Mid-infrared properties of a VO2 film near the metal-insulator transition*. Physical Review B, 1996. **54**(7): p. 4621-4628.
- 21. Qazilbash, M.M., et al., *Infrared spectroscopy and nano-imaging of the insulator-to-metal transition in vanadium dioxide*. Physical Review B, 2009. **79**(7): p. 075107.
- 22. Rensberg, J., et al., *Active Optical Metasurfaces Based on Defect-Engineered Phase-Transition Materials*. Nano Letters, 2016. **16**(2): p. 1050-1055.
- 23. Kim, Y., et al., *Phase Modulation with Electrically Tunable Vanadium Dioxide Phase-Change Metasurfaces.* Nano Letters, 2019. **19**(6): p. 3961-3968.
- 24. Hernandez-Cardoso, G.G., A.K. Singh, and E. Castro-Camus, *Empirical comparison between effective medium theory models for the dielectric response of biological tissue at terahertz frequencies*. Applied Optics, 2020. **59**(13): p. D6-D11.
- Wan, C.H., et al., On the Optical Properties of Thin-Film Vanadium Dioxide from the Visible to the Far Infrared. Annalen Der Physik, 2019. **531**(10): p. 1900188.
- 26. Lee, D., et al., Sharpened VO2 Phase Transition via Controlled Release of Epitaxial Strain. Nano Letters, 2017. 17(9): p. 5614-5619.
- 27. Yang, Z., C. Ko, and S. Ramanathan, *Oxide Electronics Utilizing Ultrafast Metal-Insulator Transitions*. Annual Review of Materials Research, 2011. **41**(1): p. 337-367.
- 28. Wegkamp, D. and J. Stähler, *Ultrafast dynamics during the photoinduced phase transition in VO2*. Progress in Surface Science, 2015. **90**(4): p. 464-502.
- 29. Ko, B., T. Badloe, and J. Rho, *Vanadium dioxide for dynamically tunable photonics*. ChemNanoMat, 2021. **7**(7): p. 713-727.
- 30. Wilson, K., C. Marocico, and A. Bradley, *Dynamic structural colour using vanadium dioxide thin films.* Journal of Physics D: Applied Physics, 2018. **51**(25): p. 255101.
- 31. Chang, T.-C., et al., *Review on thermochromic vanadium dioxide based smart coatings:* from lab to commercial application. Advances in Manufacturing, 2018. **6**: p. 1-19.
- 32. Son, T.V., et al., *Polarization modulation by vanadium dioxide on metallic substrates*. Optics Communications, 2018. **427**: p. 511-516.
- 33. In, S., et al., Self-Organized Gold Network-Vanadium Dioxide Hybrid Film for Dynamic Modulation of Visible-to-Near-Infrared Light. Advanced Photonics Research, 2020. **1**(1): p. 2000050.
- 34. Song, Z., et al., Broadband tunable terahertz absorber based on vanadium dioxide metamaterials. Optics express, 2018. **26**(6): p. 7148-7154.
- 35. Liu, H., et al., *Vanadium dioxide-assisted broadband tunable terahertz metamaterial absorber.* Scientific reports, 2019. **9**(1): p. 5751.
- 36. Chen, S., et al., *Optical switch based on vanadium dioxide thin films*. Infrared physics & technology, 2004. **45**(4): p. 239-242.
- Wu, G., et al., *Ultra-wideband tunable metamaterial perfect absorber based on vanadium dioxide*. Optics Express, 2021. **29**(2): p. 2703-2711.
- 38. Cao, B., et al., Switchable broadband metamaterial absorber/reflector based on vanadium dioxide rings. Applied Optics, 2020. **59**(27): p. 8111-8117.
- 39. Liu, W., et al., Diffractive metalens: from fundamentals, practical applications to current trends. Advances in Physics: X, 2020. 5(1): p. 1742584.
- 40. Chen, K., et al., A reconfigurable active Huygens' metalens. Advanced materials, 2017.

- **29**(17): p. 1606422.
- 41. Luo, X., Subwavelength optical engineering with metasurface waves. Advanced Optical Materials, 2018. **6**(7): p. 1701201.
- 42. Cheben, P., et al., *Subwavelength integrated photonics*. Nature, 2018. **560**(7720): p. 565-572.
- 43. Shen, Z., et al., *Liquid crystal integrated metalens with tunable chromatic aberration*. Advanced Photonics, 2020. **2**(3): p. 036002-036002.
- 44. Badloe, T., et al., *Electrically tunable bifocal metalens with diffraction-limited focusing and imaging at visible wavelengths.* Advanced Science, 2021. **8**(21): p. 2102646.
- 45. Iyer, P.P., et al., *Uniform thermo-optic tunability of dielectric metalenses*. Physical Review Applied, 2018. **10**(4): p. 044029.
- 46. Paniagua-Dominguez, R., et al., *A metalens with a near-unity numerical aperture*. Nano letters, 2018. **18**(3): p. 2124-2132.
- 47. Meng, C., et al., *Dynamic piezoelectric MEMS-based optical metasurfaces*. Science Advances, 2021. 7(26): p. eabg5639.
- 48. Zhang, C., et al., *A reconfigurable active acoustic metalens*. Applied Physics Letters, 2021. **118**(13).
- 49. Cheng, Y., et al., *Acoustic subwavelength imaging of subsurface objects with acoustic resonant metalens*. Applied Physics Letters, 2013. **103**(22).
- 50. Barceloux, D.G. and D. Barceloux, *Vanadium*. Journal of Toxicology: Clinical Toxicology, 1999. **37**(2): p. 265-278.
- 51. Surney, S., M.G. Ramsey, and F.P. Netzer, *Vanadium oxide surface studies*. Progress in Surface Science, 2003. **73**(4): p. 117-165.
- 52. Pergament, A., G. Stefanovich, and A. Velichko, *Oxide electronics and vanadium dioxide perspective: A review.* Journal on Selected Topics in Nano Electronics and Computing, 2013. **1**(1): p. 24-43.
- Wang, H., X. Yi, and Y. Li, Fabrication of VO2 films with low transition temperature for optical switching applications. Optics communications, 2005. **256**(4-6): p. 305-309.
- 54. Hong-Chen, W., et al., Fabrication and characterization of nanocrystalline VO2 thin films. Chinese Physics Letters, 2005. **22**(7): p. 1746.
- 55. Fujiwara, H., Spectroscopic ellipsometry: principles and applications. 2007: John Wiley & Sons.
- 56. Levi, A., *The Lorentz oscillator model*. Essential classical mechanics for device physics, 2016: p. 5-1.
- 57. Li, H., et al., *Analysis of the Drude model in metallic films*. Applied optics, 2001. **40**(34): p. 6307-6311.
- 58. Oka, Y., et al., *Crystal structures and transition mechanism of VO2 (A)*. Journal of Solid State Chemistry, 1998. **141**(2): p. 594-598.
- 59. Popuri, S.R., et al., VO2 (A): Reinvestigation of crystal structure, phase transition and crystal growth mechanisms. Journal of Solid State Chemistry, 2014. 213: p. 79-86.
- 60. Gavriliuk, A.G., et al., *Another mechanism for the insulator-metal transition observed in Mott insulators.* Physical Review B, 2008. 77(15): p. 155112.
- 61. Ballif, C., et al., *Status and perspectives of crystalline silicon photovoltaics in research and industry.* Nature Reviews Materials, 2022. 7(8): p. 597-616.

- 62. Hull, R., *Properties of crystalline silicon*. 1999: IET.
- 63. Cai, H., et al., *Multifunctional Hybrid Metasurfaces for Dynamic Tuning of Terahertz Waves*. Advanced Optical Materials, 2018. **6**(14).
- 64. Zhang, Z., et al., Thermochromic VO2 thin films: solution-based processing, improved optical properties, and lowered phase transformation temperature. Langmuir, 2010. **26**(13): p. 10738-10744.
- 65. Yoon, J., et al., Controlling the temperature and speed of the phase transition of VO2 microcrystals. ACS applied materials & interfaces, 2016. **8**(3): p. 2280-2286.
- 66. Sun, J. and G.K. Pribil, *Analyzing optical properties of thin vanadium oxide films through semiconductor-to-metal phase transition using spectroscopic ellipsometry*. Applied Surface Science, 2017. **421**: p. 819-823.
- 67. Prasad, P.N., *Nanophotonics*. 2004: John Wiley & Sons.
- 68. Altug, H., et al., *Advances and applications of nanophotonic biosensors*. Nature nanotechnology, 2022. **17**(1): p. 5-16.
- 69. Gaponenko, S.V., *Introduction to nanophotonics*. 2010: Cambridge University Press.
- 70. Liu, H., J. Lu, and X.R. Wang, *Metamaterials based on the phase transition of VO2*. Nanotechnology, 2017. **29**(2): p. 024002.
- 71. Peterseim, T., et al., Optical properties of VO2 films at the phase transition: Influence of substrate and electronic correlations. Journal of Applied Physics, 2016. **120**(7).
- 72. Tompkins, H. and E.A. Irene, *Handbook of ellipsometry*. 2005: William Andrew.
- 73. Jellison Jr, G.E., *Data analysis for spectroscopic ellipsometry*. Thin Solid Films, 1993. **234**(1-2): p. 416-422.
- 74. Huang, Z., et al., *Infrared characteristics of VO2 thin films for smart window and laser protection applications*. Applied Physics Letters, 2012. **101**(19).
- 75. Kocer, H., et al., *Thermal tuning of infrared resonant absorbers based on hybrid gold-VO2 nanostructures.* Applied Physics Letters, 2015. **106**(16).
- 76. Zhang, K., et al., Synthesis of VO2 thin films by atomic layer deposition with TEMAV as precursor. ECS Transactions, 2013. **50**(13): p. 175.
- 77. Jostmeier, T., et al., *Optically imprinted reconfigurable photonic elements in a VO2 nanocomposite*. Applied Physics Letters, 2014. **105**(7).
- 78. Gomez-Heredia, C., et al., *Thermal hysteresis measurement of the VO2 emissivity and its application in thermal rectification*. Scientific Reports, 2018. **8**(1): p. 8479.
- 79. Ramirez-Rincon, J., et al., *Thermal hysteresis measurement of the VO2 dielectric function for its metal-insulator transition by visible-IR ellipsometry.* Journal of Applied Physics, 2018. **124**(19).
- 80. Kats, M.A., et al., *Ultra-thin perfect absorber employing a tunable phase change material*. Applied Physics Letters, 2012. **101**(22): p. 221101.
- 81. Taylor, S., Y. Yang, and L. Wang, *Vanadium dioxide based Fabry-Perot emitter for dynamic radiative cooling applications*. Journal of Quantitative Spectroscopy and Radiative Transfer, 2017. **197**: p. 76-83.
- 82. Berthomieu, C. and R. Hienerwadel, *Fourier transform infrared (FTIR) spectroscopy*. Photosynthesis research, 2009. **101**: p. 157-170.
- 83. Choy, T.C., *Effective medium theory: principles and applications*. Vol. 165. 2015: Oxford University Press.

- 84. Lalanne, P. and D. Lemercier-Lalanne, *On the effective medium theory of subwavelength periodic structures*. Journal of Modern Optics, 1996. **43**(10): p. 2063-2085.
- 85. Choy, T.C. *Effective medium theory : principles and applications.* 1999.
- 86. Norris, A.N., P. Sheng, and A.J. Callegari, *Effective-medium theories for two-phase dielectric media*. Journal of Applied Physics, 1985. **57**(6): p. 1990-1996.
- 87. Zhang, X. and Y. Wu, *Effective medium theory for anisotropic metamaterials*. Scientific Reports, 2015. **5**(1): p. 7892.
- 88. Koschny, T., et al., *Effective medium theory of left-handed materials*. Physical review letters, 2004. **93**(10): p. 107402.
- 89. David, C., Y. Gueguen, and G. Pampoukis, *Effective medium theory and network theory applied to the transport properties of rock*. Journal of Geophysical Research: Solid Earth, 1990. **95**(B5): p. 6993-7005.
- 90. Markel, V.A., *Introduction to the Maxwell Garnett approximation: tutorial.* JOSA A, 2016. **33**(7): p. 1244-1256.
- 91. Stroud, D., *The effective medium approximations: Some recent developments.* Superlattices and microstructures, 1998. **23**(3-4): p. 567-573.
- 92. Looyenga, H., *Dielectric constants of heterogeneous mixtures*. Physica, 1965. **31**(3): p. 401-406.
- 93. Ahmet, I.Y., et al., *Polymorph-Selective Deposition of High Purity SnS Thin Films from a Single Source Precursor.* Chemistry of Materials, 2015. **27**(22): p. 7680-7688.
- 94. Niklasson, G.A., C.G. Granqvist, and O. Hunderi, *Effective medium models for the optical properties of inhomogeneous materials*. Applied Optics, 1981. **20**(1): p. 26-30.
- 95. Brosseau, C., Generalized effective medium theory and dielectric relaxation in particle-filled polymeric resins. Journal of applied physics, 2002. **91**(5): p. 3197-3204.
- 96. Wan, C., et al., On the Optical Properties of Thin-Film Vanadium Dioxide from the Visible to the Far Infrared. Annalen der Physik, 2019. **531**(10): p. 1900188.
- 97. McLachlan, D.S., et al., *Modeling the Permittivity of Composite Materials with a General Effective Medium Equation*. Journal of Electromagnetic Waves and Applications, 1992. **6**(9): p. 1099-1131.
- 98. Frey, K., M. Modell, and J. Tester, *Density-and-temperature-dependent volume translation for the SRK EOS: 1. Pure fluids.* Fluid Phase Equilibria, 2009. **279**(1): p. 56-63.
- 99. Gurvitch, M., et al., *Nonhysteretic behavior inside the hysteresis loop of VO2 and its possible application in infrared imaging.* Journal of Applied Physics, 2009. **106**(10).
- 100. Kelly, P.J. and R.D. Arnell, *Magnetron sputtering: a review of recent developments and applications*. Vacuum, 2000. **56**(3): p. 159-172.
- 101. Swann, S., Magnetron sputtering. Physics in technology, 1988. 19(2): p. 67.
- 102. Kim, Y.-W., Temperature dependent vibration analysis of functionally graded rectangular plates. Journal of Sound and Vibration, 2005. **284**(3): p. 531-549.
- 103. Kumar, S., et al., *The phase transition in VO2 probed using x-ray, visible and infrared radiations.* Applied Physics Letters, 2016. **108**(7).
- 104. Katz, M., Introduction to geometrical optics. 2002: World scientific.
- 105. Romano, A. and R. Cavaliere, Geometric optics. 2010: Springer.

- 106. Jamieson, T.H., *Thin-lens theory of zoom systems*. Optica Acta: International Journal of Optics, 1970. **17**(8): p. 565-584.
- 107. Firester, A., *The thin lens equation for optical parametric image conversion*. Optoelectronics, 1969. 1: p. 138-142.
- 108. Park, S.C. and R.R. Shannon, *Zoom lens design using lens modules*. Optical Engineering, 1996. **35**(6): p. 1668-1676.
- 109. Mikš, A., J. Novák, and P. Novák, *Method of zoom lens design*. Applied optics, 2008. **47**(32): p. 6088-6098.
- 110. Mertz, J., *Introduction to optical microscopy*. 2019: Cambridge University Press.
- 111. Davidson, M.W. and M. Abramowitz, *Optical microscopy*. Encyclopedia of imaging science and technology, 2002. **2**(1106-1141): p. 120.
- 112. Hecht, E., Optics. 2012: Pearson Education India.
- 113. Greivenkamp, J.E., *Field guide to geometrical optics*. Vol. 1. 2004: SPIE press Bellingham, Washington.
- 114. Cao, D.-Z., J. Xiong, and K. Wang, *Geometrical optics in correlated imaging systems*. Physical Review A, 2005. **71**(1): p. 013801.
- 115. Charman, W., *Wavefront technology: past, present and future.* Contact Lens and Anterior Eye, 2005. **28**(2): p. 75-92.
- 116. Parazzoli, C., et al., Experimental verification and simulation of negative index of refraction using Snell's law. Physical Review Letters, 2003. **90**(10): p. 107401.
- 117. Kweon, G.-I. and C.-H. Kim, *Aspherical lens design by using a numerical analysis*. Journal of the Korean Physical Society, 2007. **51**(1): p. 93-103.
- 118. Gutiérrez, C.E., Aspherical lens design. JOSA A, 2013. **30**(9): p. 1719-1726.
- 119. Meinhart, C.D. and S.T. Wereley, *The theory of diffraction-limited resolution in microparticle image velocimetry*. Measurement science and technology, 2003. **14**(7): p. 1047.
- 120. Hell, S.W., R. Schmidt, and A. Egner, *Diffraction-unlimited three-dimensional optical nanoscopy with opposing lenses*. Nature Photonics, 2009. **3**(7): p. 381-387.
- 121. Wang, K., et al., Design of compact freeform lens for application specific light-emitting diode packaging. Optics Express, 2010. **18**(2): p. 413-425.
- 122. Kim, S.-H., et al. Integrated micro optical flying head with lens positioning actuator for small form factor data storage. in TRANSDUCERS'03. 12th International Conference on Solid-State Sensors, Actuators and Microsystems. Digest of Technical Papers (Cat. No. 03TH8664). 2003. IEEE.
- 123. Miyamoto, K., *The phase Fresnel lens.* JOSA, 1961. **51**(1): p. 17-20.
- 124. Davis, A. and F. Kühnlenz, *Optical design using Fresnel lenses: Basic principles and some practical examples.* Optik & Photonik, 2007. **2**(4): p. 52-55.
- 125. Minin, I. and O. Minin, *Diffractive optics and nanophotonics*. Resolution below the diffraction limit. Cham: Springer, 2016.
- 126. Turunen, J. and F. Wyrowski, *Diffractive optics for industrial and commercial applications*. 1998.
- 127. O'Shea, D.C., Diffractive optics: design, fabrication, and test. Vol. 62. 2004: SPIE press.
- 128. Zhang, Q., et al., Diffractive optical elements 75 years on: from micro-optics to metasurfaces. Photonics Insights, 2023. **2**(4): p. R09-R09.

- 129. Meem, M., A. Majumder, and R. Menon, *Full-color video and still imaging using two flat lenses*. Optics express, 2018. **26**(21): p. 26866-26871.
- 130. Biswas, A., et al., Advances in top-down and bottom-up surface nanofabrication: Techniques, applications & future prospects. Advances in colloid and interface science, 2012. **170**(1-2): p. 2-27.
- 131. Zhang, S., Building from the bottom up. Materials Today, 2003. 6(5): p. 20-27.
- 132. Cai, J., et al., *Atomically precise bottom-up fabrication of graphene nanoribbons*. Nature, 2010. **466**(7305): p. 470-473.
- 133. Gupta, A., T. Sakthivel, and S. Seal, *Recent development in 2D materials beyond graphene*. Progress in Materials Science, 2015. **73**: p. 44-126.
- 134. Hu, J., et al., *A review on metasurface: from principle to smart metadevices.* Frontiers in Physics, 2021. **8**: p. 586087.
- 135. Huang, L., S. Zhang, and T. Zentgraf, *Metasurface holography: from fundamentals to applications*. Nanophotonics, 2018. 7(6): p. 1169-1190.
- 136. Jung, C., et al., *Metasurface-driven optically variable devices*. Chemical Reviews, 2021. **121**(21): p. 13013-13050.
- 137. Lin, D., et al., Dielectric gradient metasurface optical elements. science, 2014. 345(6194): p. 298-302.
- 138. Tripathi, A., et al., *Tunable Mie-resonant dielectric metasurfaces based on VO2 phase-transition materials.* ACS photonics, 2021. **8**(4): p. 1206-1213.
- 139. Li, J., et al., Frequency-switchable VO2-based coding metasurfaces at the terahertz band. Optics Communications, 2020. **458**: p. 124744.
- 140. Lysenko, S., et al., *Light-induced ultrafast phase transitions in VO2 thin film*. Applied Surface Science, 2006. **252**(15): p. 5512-5515.
- 141. Liang, H., et al., *Ultrahigh numerical aperture metalens at visible wavelengths*. Nano letters, 2018. **18**(7): p. 4460-4466.
- 142. Zuo, H., et al., *High-efficiency all-dielectric metalenses for mid-infrared imaging*. Advanced Optical Materials, 2017. **5**(23): p. 1700585.
- 143. Yoon, G., et al., *Printable nanocomposite metalens for high-contrast near-infrared imaging*. ACS nano, 2021. **15**(1): p. 698-706.
- 144. Chen, B.H., et al., *GaN metalens for pixel-level full-color routing at visible light*. Nano letters, 2017. **17**(10): p. 6345-6352.
- 145. Bai, W., et al., Near-infrared tunable metalens based on phase change material Ge2Sb2Te5. Scientific reports, 2019. 9(1): p. 5368.
- 146. Shalaginov, M.Y., et al., *Reconfigurable all-dielectric metalens with diffraction-limited performance*. Nature communications, 2021. **12**(1): p. 1225.
- 147. Li, X., et al., *Graphene metalens for particle nanotracking*. Photonics Research, 2020. **8**(8): p. 1316-1322.
- 148. Zhou, H., et al., *Broadband achromatic metalens in the midinfrared range*. Physical Review Applied, 2019. **11**(2): p. 024066.
- 149. Yang, Q., et al., *Mie-resonant membrane huygens' metasurfaces*. Advanced Functional Materials, 2020. **30**(4): p. 1906851.
- 150. Liu, W., et al., Dielectric resonance-based optical metasurfaces: from fundamentals to applications. Iscience, 2020. **23**(12).

- 151. Nieto-Vesperinas, M., *Fundamentals of Mie scattering*, in *Dielectric Metamaterials*. 2020, Elsevier. p. 39-72.
- 152. Babicheva, V.E. and A.B. Evlyukhin, *Mie-resonant metaphotonics*. Advances in Optics and Photonics, 2024. **16**(3): p. 539-658.
- 153. Liu, T., et al., Multipole and multimode engineering in Mie resonance-based metastructures. Nanophotonics, 2020. 9(5): p. 1115-1137.
- 154. Li, C. and Z. Song, *Tailoring terahertz wavefront with state switching in VO2 Pancharatnam–Berry metasurfaces.* Optics & Laser Technology, 2023. **157**: p. 108764.
- 155. He, F., K.F. MacDonald, and X. Fang, *Continuous beam steering by coherent light-by-light control of dielectric metasurface phase gradient.* Optics Express, 2020. **28**(20): p. 30107-30116.
- 156. He, F., et al., Coherently switching the focusing characteristics of all-dielectric metalenses. Optics Express, 2022. **30**(15): p. 27683-27693.
- 157. Yi, X., et al., A new fabrication method for vanadium dioxide thin films deposited by ion beam sputtering. Infrared Physics & Technology, 2003. 44(2): p. 137-141.
- 158. Fu, G., et al., *Annealing effects on VO2 thin films deposited by reactive sputtering*. Thin Solid Films, 2006. **515**(4): p. 2519-2522.
- 159. Shigesato, Y., M. Enomoto, and H. Odaka, *Thermochromic VO2 films deposited by RF magnetron sputtering using V2O3 or V2O5 targets*. Japanese Journal of Applied Physics, 2000. **39**(10R): p. 6016.
- 160. Luo, Y., et al., Optimization of microstructure and optical properties of VO2 thin film prepared by reactive sputtering. Journal of Applied Physics, 2013. 113(18).
- 161. Shibuya, K. and A. Sawa, *Optimization of conditions for growth of vanadium dioxide thin films on silicon by pulsed-laser deposition*. AIP Advances, 2015. **5**(10).
- 162. Keller, J., et al., Direct comparison of atomic layer deposition and sputtering of In2O3:H used as transparent conductive oxide layer in CuIn1-xGaxSe2 thin film solar cells. Solar Energy Materials and Solar Cells, 2016. 157: p. 757-764.
- 163. Bahlawane, N. and D. Lenoble, *Vanadium Oxide Compounds: Structure, Properties, and Growth from the Gas Phase*. Chemical Vapor Deposition, 2014. **20**(7-8-9): p. 299-311.
- 164. Berezina, O., et al., *Vanadium oxide thin films and fibers obtained by acetylacetonate sol—gel method.* Thin Solid Films, 2015. **574**: p. 15-19.
- 165. Dobbelaere, T., et al., *Plasma-Enhanced Atomic Layer Deposition of Iron Phosphate* as a Positive Electrode for 3D Lithium-Ion Microbatteries. Chemistry of Materials, 2016. **28**(10): p. 3435-3445.
- 166. Prasadam, V.P., et al., *Atomic layer deposition of vanadium oxides: process and application review.* Materials Today Chemistry, 2019. **12**: p. 396-423.
- 167. Leskelä, M. and M. Ritala, *Atomic layer deposition (ALD): from precursors to thin film structures*. Thin solid films, 2002. **409**(1): p. 138-146.
- 168. Granneman, E., et al., *Batch ALD: Characteristics, comparison with single wafer ALD, and examples.* Surface and coatings technology, 2007. **201**(22-23): p. 8899-8907.
- 169. George, S.M., A.W. Ott, and J.W. Klaus, *Surface Chemistry for Atomic Layer Growth*. The Journal of Physical Chemistry, 1996. **100**(31): p. 13121-13131.
- 170. Marrian, C.R.K. and D.M. Tennant, Nanofabrication. Journal of Vacuum Science &

- Technology A, 2003. 21(5): p. S207-S215.
- 171. George, S.M., *Atomic Layer Deposition: An Overview.* Chemical Reviews, 2010. **110**(1): p. 111-131.
- 172. Premkumar, P.A., et al., *Process study and characterization of VO2 thin films synthesized by ALD using TEMAV and O3 precursors.* ECS Journal of Solid State Science and Technology, 2012. **1**(4): p. P169.
- 173. Prasadam, V., et al., *Study of VO2 thin film synthesis by atomic layer deposition*. Materials Today Chemistry, 2019. **12**: p. 332-342.
- 174. Johnson, R.W., A. Hultqvist, and S.F. Bent, *A brief review of atomic layer deposition:* from fundamentals to applications. Materials Today, 2014. **17**(5): p. 236-246.
- 175. Lyu, W., et al., Deep-subwavelength gap modes in all-dielectric metasurfaces for highefficiency and large-angle wavefront bending. Optics Express, 2022. **30**(7): p. 12080-12091.
- 176. Zhan, T., et al., *Transfer matrix method for optics in graphene layers*. Journal of Physics: Condensed Matter, 2013. **25**(21): p. 215301.
- 177. Katsidis, C.C. and D.I. Siapkas, General transfer-matrix method for optical multilayer systems with coherent, partially coherent, and incoherent interference. Applied Optics, 2002. **41**(19): p. 3978-3987.
- 178. Leckie, F. and E. Pestel, *Transfer-matrix fundamentals*. International Journal of Mechanical Sciences, 1960. **2**(3): p. 137-167.
- 179. Huray, P.G., Maxwell's equations. 2009: John Wiley & Sons.
- 180. Sun, K., et al., *VO2 thermochromic metamaterial-based smart optical solar reflector.* Acs Photonics, 2018. **5**(6): p. 2280-2286.
- 181. Sun, K., et al., Room temperature phase transition of W-doped VO2 by atomic layer deposition on 200 mm Si wafers and flexible substrates. Advanced Optical Materials, 2022. 10(23): p. 2201326.
- 182. Chen, H. and W. Shen, *Perspectives in the characteristics and applications of Tauc-Lorentz dielectric function model*. The European Physical Journal B-Condensed Matter and Complex Systems, 2005. **43**: p. 503-507.
- 183. Reynolds, D.A., *Gaussian mixture models*. Encyclopedia of biometrics, 2009. **741**(659-663).
- 184. Sehmi, H.S., W. Langbein, and E.A. Muljarov, *Optimizing the Drude-Lorentz model for material permittivity: Method, program, and examples for gold, silver, and copper.* Physical Review B, 2017. **95**(11): p. 115444.
- 185. Lee, D., et al., *Sharpened VO2 phase transition via controlled release of epitaxial strain.*Nano letters, 2017. **17**(9): p. 5614-5619.
- 186. Sun, K., et al., VO2 Thermochromic Metamaterial-Based Smart Optical Solar Reflector. Acs Photonics, 2018. **5**(6): p. 2280-2286.
- 187. Sun, K., et al., VO2 metasurface smart thermal emitter with high visual transparency for passive radiative cooling regulation in space and terrestrial applications. Nanophotonics, 2022. 11(17): p. 4101-4114.
- 188. Berezina, O., et al., *Vanadium oxide thin films and fibers obtained by acetylacetonate sol-gel method.* Thin Solid Films, 2015. **574**: p. 15-19.
- 189. Dou, S.L., et al., The influence of temperature on preparing tungsten doped vanadium

- dioxide films by sol-gel method. Materials Research Express, 2019. 6(1): p. 016408.
- 190. Aijaz, A., et al., Low-temperature synthesis of thermochromic vanadium dioxide thin films by reactive high power impulse magnetron sputtering. Solar Energy Materials and Solar Cells, 2016. **149**: p. 137-144.
- 191. Kubo, W., et al., *Polarization-dependent phase transition temperature in plasmonic thin films*. Japanese Journal of Applied Physics, 2020. **59**(5): p. 052001.
- 192. Khairy, K.T., et al., Thermochromic properties of vanadium oxide thin films prepared by reactive magnetron sputtering at different oxygen concentrations. Vacuum, 2023. **210**: p. 111887.
- 193. Bukhari, S.A., et al., The effect of oxygen flow rate on metal-insulator transition (MIT) characteristics of vanadium dioxide (VO2) thin films by pulsed laser deposition (PLD). Applied Surface Science, 2020. **529**: p. 146995.
- 194. Kumi-Barimah, E., D.E. Anagnostou, and G. Jose, *Phase changeable vanadium dioxide (VO2) thin films grown from vanadium pentoxide (V2O5) using femtosecond pulsed laser deposition*. Aip Advances, 2020. **10**(6): p. 065225.
- 195. Graf, D., et al., *Interdependence of Structure, Morphology, and Phase Transitions in CVD Grown VO2 and V2O3 Nanostructures.* Chemistry of Materials, 2017. **29**(14): p. 5877-5885.
- 196. Makarevich, A., et al., Hydrothermal epitaxy growth of self-organized vanadium dioxide 3D structures with metal-insulator transition and THz transmission switch properties. Crystengcomm, 2020. 22(15): p. 2612-2620.
- 197. Geng, X., et al., *Tuning Phase Transition and Thermochromic Properties of Vanadium Dioxide Thin Films via Cobalt Doping*. ACS Applied Materials & Interfaces, 2022. **14**(17): p. 19736-19746.
- 198. Peter, A.P., et al., *Metal-Insulator Transition in ALD VO2 Ultrathin Films and Nanoparticles: Morphological Control.* Advanced Functional Materials, 2015. **25**(5): p. 679-686.
- 199. Mattelaer, F., et al., *Atomic layer deposition of vanadium oxides for thin-film lithium-ion battery applications*. Rsc Advances, 2016. **6**(115): p. 114658-114665.
- 200. Sun, K., et al., Room Temperature Phase Transition of W-Doped VO2 by Atomic Layer Deposition on 200 mm Si Wafers and Flexible Substrates. Advanced Optical Materials, 2022. **10**(23): p. 2201326.
- 201. Khardani, M., M. Bouaïcha, and B. Bessaïs, *Bruggeman effective medium approach* for modelling optical properties of porous silicon: comparison with experiment. physica status solidi c, 2007. **4**(6): p. 1986-1990.
- 202. Rakic, A.D., Algorithm for the Determination of Intrinsic Optical-Constants of Metal-Films Application to Aluminum. Applied Optics, 1995. **34**(22): p. 4755-4767.
- 203. Kischkat, J., et al., Mid-infrared optical properties of thin films of aluminum oxide, titanium dioxide, silicon dioxide, aluminum nitride, and silicon nitride. Applied Optics, 2012. **51**(28): p. 6789-6798.
- 204. Zhong, X., et al., *Avalanche breakdown in microscale VO2 structures*. Journal of Applied Physics, 2011. **110**(8): p. 084516.
- 205. Zhao, Y., et al., *A broadband and switchable VO2-based perfect absorber at the THz frequency.* Optics Communications, 2018. **426**: p. 443-449.

- 206. Seo, M.A., et al., *Terahertz field enhancement by a metallic nano slit operating beyond the skin-depth limit.* Nature Photonics, 2009. **3**(3): p. 152-156.
- 207. Shul, R., et al., *Inductively coupled plasma etching of GaN*. Applied physics letters, 1996. **69**(8): p. 1119-1121.
- 208. Paik, H., et al., Transport properties of ultra-thin VO2 films on (001) TiO2 grown by reactive molecular-beam epitaxy. Applied physics letters, 2015. 107(16).
- 209. Fan, L., et al., Infrared response and optoelectronic memory device fabrication based on epitaxial VO2 film. ACS applied materials & interfaces, 2016. **8**(48): p. 32971-32977.
- 210. Peter, A.P., et al., *Metal-insulator transition in ALD VO2 ultrathin films and nanoparticles: morphological control.* Advanced Functional Materials, 2015. **25**(5): p. 679-686.
- 211. Lin, T., Y. Zhang, and D. Zheng, *The ultrathin VO2 (M) film with ultrahigh visible transmittance synthesized on the quartz glass substrate by HiPIMS.* Vacuum, 2018. **156**: p. 449-455.
- 212. Chen, Y.G., et al., Engineering the Phase Front of Light with Phase-Change Material Based Planar lenses. Scientific Reports, 2015. 5: p. 8660.
- 213. Marinica, D., A. Borisov, and S. Shabanov, *Bound states in the continuum in photonics*. Physical review letters, 2008. **100**(18): p. 183902.
- 214. Hsu, C.W., et al., *Bound states in the continuum*. Nature Reviews Materials, 2016. **1**(9): p. 1-13.
- 215. Levanon, N., et al., Angular transmission response of in-plane symmetry-breaking quasi-bic all-dielectric metasurfaces. ACS Photonics, 2022. 9(11): p. 3642-3648.
- 216. Miroshnichenko, A.E., S. Flach, and Y.S. Kivshar, *Fano resonances in nanoscale structures*. Reviews of Modern Physics, 2010. **82**(3): p. 2257.
- 217. Limonov, M.F., et al., *Fano resonances in photonics*. Nature photonics, 2017. **11**(9): p. 543-554.
- 218. Yang, S., et al., *Nanoparticle trapping in a quasi-BIC system*. ACS Photonics, 2021. **8**(7): p. 1961-1971.